First-Principles Molecular Modeling of Structure-Property Relationships and Reactivity in the Zeolite Chabazite

by

Cynthia S. Lo

Submitted to the Department of Chemical Engineering
in partial fulfillment of the requirements for the degree of

Doctor of Philosophy

at the

MASSACHUSETTS INSTITUTE OF TECHNOLOGY

February 2005

Author .....
Department of Chemical Engineering
November 3, 2004

Certified by .....
Bernhardt L. Trout
Associate Professor of Chemical Engineering
Thesis Supervisor

Accepted by .....
Daniel Blankschtein
Professor of Chemical Engineering
Chairman, Committee for Graduate Students

First-Principles Molecular Modeling of Structure-Property Relationships and Reactivity in the Zeolite Chabazite

by

Cynthia S. Lo

Submitted to the Department of Chemical Engineering
on November 3, 2004, in partial fulfillment of the
requirements for the degree of
Doctor of Philosophy

Abstract

Zeolites are crystalline, porous aluminosilicates; while a pure silicate structure is charge-neutral, the substitution of Al^{3+} for Si^{4+} creates in the framework a negative charge, which can be compensated by a proton that acts as a strong, acid-donating Brønsted site. Zeolites are widely used in industry, most commonly for catalysis and separations. Unfortunately, they have not yet been able to replace all homogeneous catalysts in industrial processes due to the difficulties in reactant and product diffusion to and from the zeolite surface in the absence of a solvent. However, it is believed that if we had a thorough understanding of how solid acids, especially zeolites, catalyze reactions, then we would be able to design heterogeneous catalysts to overcome these difficulties.

The nature of the acid sites in zeolites and the factors contributing to enhanced catalytic activity have been the subject of much study in the literature. In particular, the issue of whether all of the acid sites in a particular zeolite are homogeneous or heterogeneous in acid strength requires the development of a systematic way to quantify acidity. To address this, a detailed density functional theory (DFT) investigation of the reactivity of the acid sites in the zeolite chabazite was performed. Energies of adsorption of bases, deprotonation energies, and vibrational frequencies were calculated on a periodic chabazite (SSZ-13) model with various loadings of acid sites per unit cell, and with various structural framework defects. The four acidic oxygens at the aluminum T-site were found to all have roughly the same proton affinity, and the deprotonation energy is not correlated to the O-H bond length or vibrational stretch frequency. Furthermore, the adsorption energy of various bases at each acid site oxygen was found to be roughly the same and correlated only to the gas-phase proton affinity of the base; it does not vary significantly with acid site concentration or framework defects near the acid site. Given the range of local chemical structure that we investigated, these results suggest that the strength of the acid sites in chabazite is not influenced significantly by chemical or structural variations in the framework near the acid site.

A comprehensive methodology was also developed and implemented for studying

the mechanism for the coupling reaction of two methanol molecules to form ethanol and water in the zeolite chabazite. This test reaction models an initial carbon-carbon bond formation, which is thought to be the rate limiting step in the industrial methanol-to-gasoline and methanol-to-olefins processes. Transition path sampling and constrained molecular dynamics, within the Car-Parrinello approach, were used to study this reaction. A new mechanism was found for the carbon-carbon bond formation, which proceeds at 400 °C via stable intermediates of water, methane, and protonated formaldehyde. The carbon-carbon bond forms directly and concurrently with a proton transfer from methane to water. This mechanism does not involve the formation of dimethyl ether or surface methoxy groups at the acid site, as previously postulated. Also, the free energy barriers for the reaction in chabazite were compared to the free energy barriers for the analogous reaction in the gas phase, and the results suggest that the most likely role of the zeolite framework is molecular shape selectivity – constraining the gas phase reactants so that they are in close enough proximity to react.

Thesis Supervisor: Bernhardt L. Trout
Title: Associate Professor

Acknowledgments

- To God, the Father Almighty, the Creator of heaven and earth, for showing His love, joy, peace, patience, kindness, goodness, faithfulness, gentleness, and self-control to me, without whose justification and righteousness I would not be writing this today.

- To my thesis advisor, Bernhardt Trout, for sparking my interest in both quantum mechanical calculations and molecular dynamics simulations, encouraging me to study condensed matter systems, developing my skills in and love for research by offering valuable insights and direction, generously giving his time to help me with everything, and being a wonderful and supportive PhD advisor and a real joy to work for.

- To my thesis committee members Gerbrand Ceder, Karen Gleason, and William Green, for contributing their unique perspective, both computational and experimental, on my research, encouraging me to think about the big picture in terms of the industrial impact of my research, and being wonderful and supportive throughout my time at MIT.

- To Ravi Radhakrishnan, for helping me with the coding of the transition path sampling algorithm, teaching me so much about simulation methods, and encouraging me in my academic career.

- To Claudiu Giurumescu, for helping me with the initial constrained MD calculations and setting up the chabazite models, and teaching me all I know about UNIX and tape backups.

- To my other Trout Group labmates Brian Anderson, Brian Baynes, Gregg Beckham, Zhitao Cao, Nai-Yuan Chang, Jhih-Wei Chu, Alec Demurov, Chong Gu, Xi Lin, Yves Mantz, Oleg Mazyar, Faye McNeill, Philip Osafo-Kwaako, Bin Pan, Jane Rempel, Ning Shan, Hairong Tang, and Gwen Wilcox, for providing a supportive and fun work environment, full of intellectual stimulation and welcome

distractions after a long day of work, and laboring with me in our never-ending adventures in building computers, moving them from room to room, and calling PCs for Everyone.

- To my parents, Yi-Kang and Serene Lo, for raising me in a loving and supportive home, encouraging me to pursue my love of science and engineering by helping out with school projects and field trips, sacrificing so much to give Caleb and me the opportunities they didn't have, giving me discipline and love when I needed it, and bringing me up in the training and instruction of the Lord.

- To my little brother, Caleb Lo, for encouraging me professionally and personally during late night phone calls and IM chats, looking up to me even when I don't feel that I've accomplished all that much, and painstakingly proofreading each of my journal articles.

- To Kevin Ford and Mary Thompson, for helping me grow so much in my faith and servant leadership skills, and being the best InterVarsity staffworkers I could have ever asked for.

- To Jeffrey Blackburne, Clayton Featherstone, Ali Hadiashar, and Stephen Thrasher, for instilling their laid-back attitude in me, introducing me to the wonders of Futurama, Space Ghost, and Homestar Runner, and telling me constantly that "Dudes are number 1" (and props to Stephen for pointing out that Jeff calls me "Dude").

- To Jonathan Bratt, Daniel Nagaj, and Eric Orozco, for eating all of my cooking creations without complaint, playing Settlers of Catan with me into the wee hours of the night, and making Ashdown House a wonderful place to live.

- To Donald Crankshaw, David Chan, and John Lee, for serving joyfully with me as co-leaders for the Hardcore Bible Study, and encouraging me in the integration of my academics and my faith. And to those who have at any point attended the Hardcore Bible Study, for being the best and most supportive community of fellow Christians that I have ever been a part of.

- To Stephen Geiger, for introducing me to Christian music, working with me tirelessly and painstakingly on the website for the Salvation Army project, and accompanying me on countless late-night driving expeditions in search of open restaurants and diners.

- To Johanna Goth, Zianette Viera and Yiwen Zhang, for reminding me that it's cool to be female at MIT, being kind and trustworthy at all times, and encouraging me to develop my non-academic interests in origami, cooking, and swimming.

- To Ahmed Ismail, for visiting the Trout Group in the basement during his regular trips to the snail mail room, engaging me in thought-provoking discussions about simulations and real life, and personifying the word "snarky".

- To Susan Kern, for praying for and suppporting me during our weekly lunchtime meetings, and selflessly driving me to Target, Trader Joe's, and Guitar Center for my mega-shopping expeditions.

- To Edward Kopesky and Kenneth Lau, for watching sporting events and laughing at slapstick comedies on TV with me whenever I needed a break from work.

- To Muyiwa Ogunnika, for allowing me to ridicule his failed electronics purchases, and being a kind and supportive fellow TA for 10.34.

- To Gregory Pollock, Ji-Jon Sit, and Joseph Tracy for faithfully serving on the GCF leadership team with me for multiple years, and being wonderfully trustworthy, selfless, and loyal as friends.

- To all of my other friends that I did not properly acknowledge here, for unselfishly giving their quality time and offering prayers of support for me throughout my time at MIT.

- To Jesus Christ, His only Son, my Lord, for bearing my cross and my shame, without whose sacrifice I would not be writing this today. Amen.

Contents

List of Figures

List of Tables

Chapter 1

Introduction

Zeolites are crystalline, porous aluminosilicates made up of edge-sharing SiO_4 and AlO_4 tetrahedra in a framework structure; for that reason, the non-oxygen lattice atoms are called T-sites. A pure silicate structure is charge-neutral; however, the substitution of Al^{3+} for Si^{4+} creates in the framework a negative charge, which can be compensated by a proton that acts as a strong, acid-donating Brønsted site.

Zeolites are widely used in industry, most commonly for catalysis and separations. In the 1970's their use in the petrochemical industry was spurred by the development of the methanol to gasoline (MTG) process by Mobil, and in 1996, the development of the methanol-to-olefins (MTO) process by UOP/Hydro [138]. There are many benefits to using heterogeneous catalysts instead of liquid-phase processes, including waste minimization, options of a wide range of possible process operating conditions, and ease of product separation [38].

Unfortunately, solid-acid catalysts have not been able to replace all homogeneous catalysts in industrial processes. There are various reasons for this, including the difficulties in reactant and product diffusion to and from the zeolite surface in the absence of a solvent. However, it is believed that if we had a thorough understanding of how solid acids, especially zeolites, catalyze reactions, then we would be able to design heterogeneous catalysts to overcome these difficulties [61].

There does not yet exist even a simple measure for quantifying the acidity of the Brønsted sites in zeolites. Various measures have been proposed, including the O-H

bond length and infrared (IR) frequency [43], intensities of the IR O-H stretching bands [79], deprotonation energy (proton affinity), heats of adsorption of ammonia, pyridine, and other small base probe molecules measured by microcalorimetry and thermal programmed desorption [12], energy barriers for proton jump between neighboring oxygen atoms measured by variable temperature ^{1}H NMR [125], and even a lumped intrinsic acidity that is defined as the quotient of the O-H bond length and the O-H vibrational frequency [135].

Furthermore, there is no adequate scale for solid acidity that is analogous to the pK_a and Hammett acidity function [68] for aqueous acidity. Haw et al. [101, 69] found that ^{19}F and ^{15}N NMR could be used to measure the spectroscopic changes of Hammett bases adsorbed onto zeolites. However, it was pointed out by Fărcaşiu et al. [56] that the Hammett acidity values of solid acids are not useful measures of acidity and not correlated with the catalytic activity, since the protonation of a base by a solid acid site leads to the formation of a localized tight ion pair, for which the requirement of the neutral and protonated base having identical activity coefficients is not satisfied.

In particular, the issue of whether all of the acid sites in a particular zeolite are homogeneous or heterogeneous in acid strength requires the development of a systematic way to quantify acidity. It has been hypothesized by several researchers that the acid strength is affected by physical properties of the local framework structure and constituent atoms, and the Brønsted sites are heterogeneous in acid strength. The goal is a quantitative understanding of the factors that are responsible for differences in catalytic activity and how zeolites catalyze reactions, with the objective of using this information to design catalysts more effectively. It is hoped that by studying structure-property relationships in zeolites, insight will be provided into whether the strength of a zeolite's catalytic activity is determined primarily by differences in acid site strengths and geometric properties, or whether the influences are external and unrelated to the acid site.

A second, but perhaps even more important goal is to gain some understanding as to how zeolites catalyze solid state reactions. In general, reaction networks

for chemical processes occurring on solid surfaces are complex, involving dissociative adsorption, surface reactions, desorption, and other gas phase reactions. It is also difficult to study the mechanisms of the individual elementary reactions comprising these reaction networks, since most experimental methods determine composite properties that consist of many elementary steps lumped together, such as conversion rates and product selectivities. Therefore, computational methods that could be used to isolate and quantify elementary steps would be quite useful.

The exact role of zeolites in catalysis is also not known. Zeolites are Brønsted acids, so perhaps they may simply serve as a convenient proton source, which would otherwise be unattainable in the gas phase, for acid-catalyzed reactions. Another possibility is that zeolites work by molecular shape selectivity, where the gas phase reactants are constrained within the zeolite cages and channels so that they are in close enough proximity to react. These are short-range repulsions. Recently, it has been thought that the primary role of zeolites is for confinement, which consists of long-range and attractive interactions. These interactions increase the physisorption energies of the adsorbates up to values which are comparable to the activation energies for reactions. The zeolite framework may also act as a "solid solvent" in the case where the reactants and products are of comparable size to the diameter of the zeolite cages and channels, and work to stabilize the reactive transition state [51]. Most likely, zeolites work by a combination of these factors.

The model zeolite studied in this thesis is chabazite (SSZ-13) (Figure 1-1), which has 36 atoms in its unit cell. Chabazite has a trigonal unit cell ($a = b = c = 9.281$ Å, $\alpha = \beta = \gamma = 94.275°$), and we used the structural parameters determined by Smith et al. [128] using neutron diffraction. It contains two 8T, three 4T, and one 6T ring, where an 8T ring, for example, contains eight Si or Al atoms, and eight O atoms.

Chabazite was chosen mainly because of the small size of its unit cell, which means that the zeolite structure can be modeled as a periodic system, as opposed to using the cluster approximation, which treats just the atoms near the acid site and saturates the dangling bonds of the cluster with hydrogen atoms. The periodic approach is believed to be more representative of the physical system because the interactions of

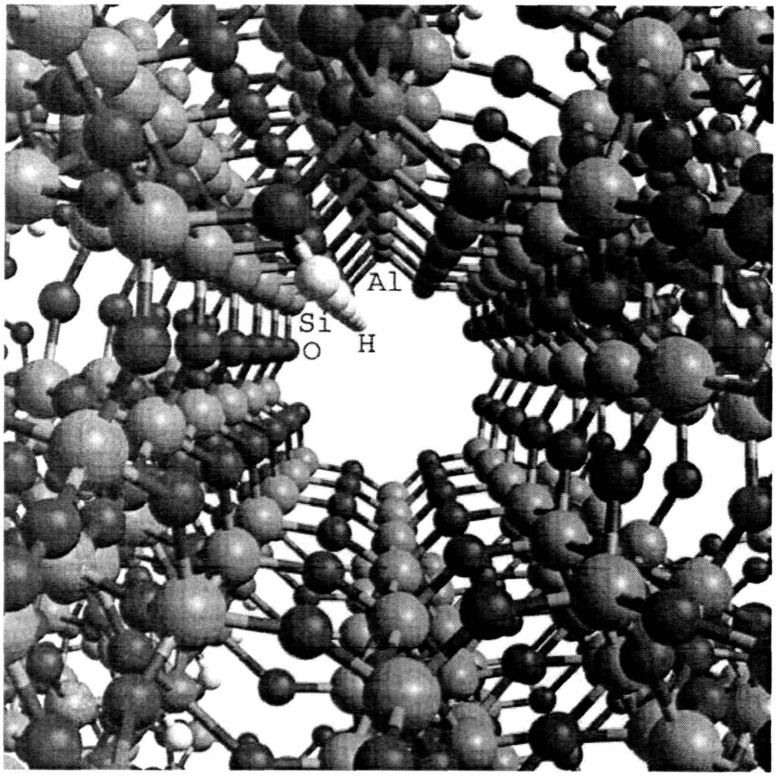

Figure 1-1: Perspective view down a channel of 8T rings in protonated chabazite with 1 Al/unit cell

adsorbed molecules with the zeolite framework, not just at the acid site, are explicitly included. Also, the use of periodic models means that the long-range electrostatic potential of the zeolite can be included without using linking methods.

Chapter 2 focuses on a derivation of the methods used in this thesis, including Density Functional Theory for calculating energetic and spectroscopic properties, Car-Parrinello molecular dynamics for simulating condensed matter processes including bond breakage and bond formation, constrained molecular dynamics for computing initial reaction paths that, while unphysical, help suggest reaction products and pathways that cross the transition state region, and transition path sampling for computing dynamic reaction paths that converge toward the true reaction mechanism.

Chapter 3 focuses on an understanding the effects of local structural defects on energetic properties at the acid site of a given zeolite, and evaluating several measures to probe the acid strength of the Brønsted sites.

Chapter 4 focuses on the methanol coupling reaction as a model for C-C bond formation, which is thought to be the rate-limiting step for the industrial methanol to gasoline (MTG) and methanol to olefins (MTO) processes. Specifically, the focus is on computing the dynamic reaction mechanism for this multi-step reaction, and on identifying the intermediates and products of the reaction.

Chapter 5 focuses on the methanol coupling reaction, specifically on identifying the correct reaction coordinates, and computing the free energy barriers for the individual reaction steps.

Finally, overall conclusions from this thesis, as well as suggestions for future work, are presented in Chapter 6.

Chapter 2

Methodology and Approach

2.1 Computational Tools

Molecular dynamics is the numerical integration of Newton's equation of motion to generate realistic physical trajectories, which are chronological sequences of points in phase space – configuration space and momentum space combined. Classical molecular dynamics using "predefined potentials", either based on empirical data or on independent electronic structure calculations, is commonly used to investigate many-body condensed matter systems; there are also many MD packages available, including CHARMM [23], AMBER [109], and NAMD [99]. The key is how to describe the interatomic interactions. In classical MD, the potentials are determined in advance, by considering two-body, three-body, and many-body contributions, both long-range and short range.

However, the need to fix the potentials beforehand poses serious limitations, especially for chemically complex systems where either: 1. There are many different atoms and molecules, and consequently many different interatomic interactions that must be parameterized, or 2. The electronic structure and bonding patterns change over the course of the MD simulations. Zeolite-catalyzed reactions fall into the second category, since they depend on the energetics of bond breakage and bond formation.

Instead, *ab initio* MD simulations will be performed on the chabazite system. The basic idea underlying *ab initio* MD is to compute the interatomic forces from electronic

structure calculations "on the fly" as the MD trajectory is generated. A brief overview of these methods, particularly in reference to Density Functional Theory (DFT) and the Car-Parrinello method (CPMD), is given in this section.

2.1.1 Density Functional Theory

Kohn and Sham expressed the total ground-state energy of an interacting system of electrons, with the classical nuclei fixed at positions $\{\mathbf{R}_I\}$, as a sum of several components:

$$E^{KS}[\{\phi_i\}] = T_s[\{\phi_i\}] + \int d\mathbf{r}\, V_{ext}(\mathbf{r})\, n(\mathbf{r}) + \frac{1}{2}\int d\mathbf{r}\, V_H(\mathbf{r})\, n(\mathbf{r}) + E_{xc}[n] \quad (2.1)$$

$$n(\mathbf{r}) = \sum_i |\phi_i(\mathbf{r})|^2$$

$$T_s[\{\phi_i\}] = \sum_i \frac{\hbar^2}{2m}\int d\mathbf{r}\, \phi_i^*(\mathbf{r})\left(-\nabla^2\right)\phi_i(\mathbf{r})$$

$$V_{ext}(\mathbf{r}) = -\sum_I \frac{Z_I}{|\mathbf{R}_I - \mathbf{r}|} + \sum_{I<J}\frac{Z_I Z_J}{|\mathbf{R}_I - \mathbf{R}_J|}$$

$$V_H(\mathbf{r}) = \int d\mathbf{r}\, \frac{n(\mathbf{r}')}{|\mathbf{r} - \mathbf{r}'|}$$

$n(\mathbf{r})$ is the electronic charge density; it is expressed in terms of the Kohn-Sham orbitals $\{\phi_i\}$, which are a set of orthonormal one-particle functions. $T_s[\{\phi_i\}]$ is the kinetic energy of a non-interacting reference system with the same number of electrons exposed to the same external potential as the fully interacting system [83], $V_{ext}(\mathbf{r})$ is the fixed external potential in which the electrons move, which comprises Coulombic interactions between the electrons and nuclei, and $V_H(\mathbf{r})$ is the Hartree potential, or classical electrostatic energy of two charge clouds stemming from the charge density. $E_{xc}[n]$ is the exchange-correlation functional, which is very difficult to calculate.

If the Kohn-Sham energy functional is minimized with respect to the orbitals $\{\phi_i\}$, the resulting equation is:

$$\left\{-\frac{\hbar^2}{2m}\nabla^2 + V_{ext}(\mathbf{r}) + V_H(\mathbf{r}) + \frac{\partial E_{xc}[n]}{\partial n(\mathbf{r})}\right\}\phi_i(\mathbf{r}) = \epsilon_i\phi_i(\mathbf{r}) \tag{2.2}$$

Hohenberg and Kohn proved [72] that if the exact forms of $T_s[\{\phi_i\}]$ and $E_{xc}[n]$ functionals were known, then the exact energy could be obtained from just the density $n(\mathbf{r})$.

The challenge has been to postulate an accurate expression for the exchange-correlation functional.

$$E_{xc}[n] = \int d\mathbf{r}\, n(\mathbf{r})\, \epsilon_{xc}[n(\mathbf{r})] \tag{2.3}$$

where $\epsilon_{xc}[n(\mathbf{r})]$ is the exchange-correlation energy per particle. In the local density approximation (LDA), $\epsilon_{xc}[n(\mathbf{r})]$ is simply approximated by the exchange-correlation energy associated with a homogeneous electron gas of the same density. Fortunately, this is known precisely, because if $\epsilon_{xc}[n(\mathbf{r})] = \epsilon_x[n(\mathbf{r})] + \epsilon_c[n(\mathbf{r})]$, then [53]:

$$\epsilon_x[n(\mathbf{r})] = -\frac{3}{4}\left(\frac{3}{\pi}\right)^{1/3} n(\mathbf{r})^{1/3} \tag{2.4}$$

and $\epsilon_c[n(\mathbf{r})]$ has been determined from Quantum Monte Carlo simulations [28]. Unfortunately, the LDA approximation fails in situations where the density undergoes rapid changes such as in molecular systems.

The generalized gradient approximations (GGA) adds gradients of the density to the exchange correlation functional:

$$E_{xc}[n] = \int d\mathbf{r}\, F(\mathbf{r}, \nabla\mathbf{r}) \tag{2.5}$$

Two commonly used GGA functionals are the Becke-Lee-Yang-Parr (BLYP), with the Becke exchange functional [8] and the Lee-Yang-Parr correlation functional [85], and the Perdew-Wang (PW91) functional. The PW91 functional has the following exchange term:

$$E_x[n] = \int d\mathbf{r}\, n[\mathbf{r}]\, \epsilon_x(r_s, 0)\, F(s) \tag{2.6}$$

$$\epsilon_x(r_s, 0) = \frac{3k_F}{4\pi}$$

$$k_F = \left(3\pi^2 n\right)^{1/3}$$

$$s = \frac{|\nabla n|}{2k_F n}$$

$$F(s) = \frac{1 + 0.19645 s \sinh^{-1}(7.7956 s) + \left(0.2743 - 0.1508 e^{-100 s^2}\right) s^2}{1 + 0.19645 s \sinh^{-1}(7.7956 s) + 0.004 s^4}$$

and the following correlation term:

$$E_c[n] = \int d\mathbf{r}\, n[\mathbf{r}]\, (\epsilon_c(r_s, \zeta) + H(t, r_s, \zeta)) \tag{2.7}$$

$$t = \frac{|\nabla n|}{2 g k_s n}$$

$$g = \frac{(1+\zeta)^{2/3} + (1-\zeta)^{2/3}}{2}$$

$$k_s = \left(\frac{4k_F}{\pi}\right)^{1/2}$$

$$H = H_0 + H_1$$

$$H_0 = g^3 \frac{\beta^2}{2\alpha} \ln\left[1 + \frac{2\alpha}{\beta} \frac{t^2 + At^4}{1 + At^2 + A^2 t^4}\right]$$

$$H_1 = \nu \left[C_c(r_s) - C_c(0) - \frac{3C_x}{7}\right] g^3 t^2 \exp\left[-100 g^4 \left(\frac{k_s^2}{k_F^2}\right) t^2\right]$$

$$\alpha = 0.09$$

$$\beta = \nu C_c(0)$$

$$\nu = \frac{16}{\pi}\left(3\pi^2\right)^{1/3}$$

$$C_c(0) = 0.004235$$

$$C_x = -0.001667$$

$$A = \frac{2\alpha}{\beta} \frac{1}{\exp\left[-\frac{2\alpha \epsilon_c(r_s, \zeta)}{g^3 \beta^2}\right] - 1}$$

where analytical expressions for $\epsilon_c(r_s, \zeta)$ [148, 111] and $C_c(r_s)$ [113] are available. All of the calculations in this thesis make use of the PW91 functional.

2.1.2 Plane Wave Basis Sets

An important consideration when using the one-particle Kohn-Sham orbitals $\{\phi_i\}$ is determining how to express them in terms of simple analytic functions f_ν with well-known properties. In general, a linear combination of these basis functions can be used:

$$\phi_i(\mathbf{r}) = \sum_\nu c_{i\nu} f_\nu(\mathbf{r}; \{\mathbf{R}_I\}) \tag{2.8}$$

For systems with periodic lattices, it is useful to describe the unit cell by Bravais lattice vectors $\mathbf{a}_1, \mathbf{a}_2, \mathbf{a}_3$, which can be combined into a 3x3 matrix: $\mathbf{h} = [\mathbf{a}_1, \mathbf{a}_2, \mathbf{a}_3]$. Then the volume Ω of the cell is defined as the determinant of $\mathbf{h}$.

The reciprocal lattice vectors $\mathbf{b}_i$ are defined as:

$$\mathbf{b}_i \cdot \mathbf{a}_j = 2\pi\delta_{ij} \tag{2.9}$$

which in turn can be arranged in a 3x3 matrix: $2\pi\left(\mathbf{h}^t\right)^{-1} = [\mathbf{b}_1, \mathbf{b}_2, \mathbf{b}_3]$. Therefore, the reciprocal space vectors $\mathbf{G}$ are given as:

$$\mathbf{G} = 2\pi\left(\mathbf{h}^t\right)^{-1}\mathbf{g} \tag{2.10}$$

and $\mathbf{g} = [i, j, k]$ is a triple of integer values.

Plane waves can therefore build a complete and orthonormal basis:

$$f_{\mathbf{G}}^{PW}(\mathbf{r}) = \frac{1}{\sqrt{\Omega}} \exp[i\mathbf{G} \cdot \mathbf{r}] \tag{2.11}$$

Therefore, a periodic function $u(\mathbf{r})$ can be expanded in this basis as:

$$u(\mathbf{r}) = u(\mathbf{r} + \mathbf{L}) = \frac{1}{\sqrt{\Omega}} \sum_{\mathbf{G}} u(\mathbf{G}) \exp[i\mathbf{G} \cdot \mathbf{r}] \tag{2.12}$$

where $\mathbf{L}$ is the set of direct lattice vectors connecting equivalent points in different cells, and $u(\mathbf{r})$ and $u(\mathbf{G})$ are related by a three-dimensional Fourier transform.

The Kohn-Sham potential is periodic:

$$V^{KS}(\mathbf{r}) = V^{KS}(\mathbf{r}+\mathbf{L}) \tag{2.13}$$

and the Kohn-Sham orbitals can be expressed as:

$$\phi_i(\mathbf{r},\mathbf{k}) = \frac{1}{\sqrt{\Omega}} \sum_{\mathbf{G}} c_i(\mathbf{G},\mathbf{k}) \exp[i\mathbf{G}\cdot\mathbf{r}] \tag{2.14}$$

where $\mathbf{k}$ is a vector in the first Brillouin zone. Finally, the density can also be expanded into the plane wave basis:

$$\begin{aligned} n(\mathbf{r}) &= \frac{1}{\sqrt{\Omega}} \sum_i \int d\mathbf{k}\, f_i(\mathbf{k}) \sum_{\mathbf{G},\mathbf{G}'} c_i^*(\mathbf{G}',\mathbf{k})\, c_i(\mathbf{G},\mathbf{k}) \exp[i(\mathbf{G}+\mathbf{k})\cdot\mathbf{r}] \\ &= \sum_{\mathbf{G}} n(\mathbf{G}) \exp[i\mathbf{G}\cdot\mathbf{r}] \end{aligned} \tag{2.15}$$

In practice, the infinite sums over $\mathbf{G}$ vectors and cells must be truncated. The integral over the Brillouin zone is approximated by a finite sum:

$$\int d\mathbf{k} \rightarrow \sum_{\mathbf{k}} w_k \tag{2.16}$$

where w_k are the weights of the integration points. Also, at each $\mathbf{k}$-point, only $\mathbf{G}$ vectors with a kinetic energy lower than a maximum cutoff E_{cut} are included:

$$\frac{1}{2}|\mathbf{k}+\mathbf{G}|^2 \leq E_{cut} \tag{2.17}$$

Many theoretical studies on base adsorption and reactivity on zeolites have been previously performed, but most of them have relied on the cluster approximation, which models the zeolite by treating only a few atoms at the acid site without considering the effects of the rest of the framework. The dangling bonds of the cluster are

saturated with hydrogen atoms, which affects the acidity of the cluster. This would be a problem for the calculations in Chapter 3. Also, the cluster model also ignores the long-range electrostatic potential. Recent theoretical approaches to remedy these probles have employed the embedded cluster model, which embeds the clusters in a set of point charges chosen to reproduce the bulk potential. However, this approach still neglects the interaction of an adsorbed molecule with the rest of the zeolite framework. Therefore, in this thesis the zeolite has been modeled as a full periodic lattice. The E_{cut} used is 55 Rydbergs.

2.1.3 Pseudopotentials

In general, all-electron calculations are poorly suited for infinite crystalline systems, since a very large number of plane waves are required to accurately describe the rapidly oscillating electronic wavefunctions in the core region. In order to minimize the size of the plane wave basis, the core electrons are replaced by pseudopotentials. Pseudopotentials are needed that correctly represent the wavefunction in the core; inside the sphere of radius r_c, the pseudopotential and the wavefunction, along with its first and second derivative, should be smooth and non-oscillatory so that a relatively small number of plane waves can be used while still maintaining an identical norm, or net charge density. Also, the pseudopotentials should produce pseudo-wavefunction solutions, or eigenvalues, that approach the full wavefunction outside the core radius r_c. Finally, the pseudopotentials should be transferable, or usable in calculations of comparable accuracy in different chemical structures.

Norm-conserving pseudopotentials, such as those generated by Trouiller and Martins [141], are semi-local, which means that the local part is dependent on the radius only, and the long-range part is dependent on the angular momentum. This means that each angular momentum component of the wavefunction will see a different potential. Therefore, the pseudopotential is given by:

$$V^{PP}(\mathbf{r}) = V^{PP}_{\text{local}}(\mathbf{r}) + \sum_{l} V^{PP}_{\text{semi-local}}(\mathbf{r})\, P_l \tag{2.18}$$

where P_l . In general, the semi-local potential can be expressed as a sum of spherical harmonics.

Kleinman and Bylander [] transformed a semi-local potential into a nonlocal one:

$$V^{KB}_{\text{nonlocal},l}(\mathbf{r}) = \frac{|V_{\text{semi-local},l}(\mathbf{r})\,\Phi^{PP,0}_l(\mathbf{r})\rangle\langle\Phi^{PP,0}_l(\mathbf{r})\,V_{\text{semi-local},l}(\mathbf{r})|}{\langle\Phi^{PP,0}_l(\mathbf{r})\,|V_{\text{semi-local},l}(\mathbf{r})\,|\Phi^{PP,0}_l(\mathbf{r})\rangle} \tag{2.19}$$

Kerker [] and Troullier and Martins [141] proposed a pseudo-wavefunction in the core that would behave as r^l for small r, and which has no nodes:

$$R^{PP}_l(r) = \begin{cases} R^{AE}_l(r) & \text{if } r \geq r_c \\ r^l \exp[p(r)] & \text{if } r \leq r_c \end{cases} \tag{2.20}$$

Kerker set the polynomial $p(r)$ to be of degree $n = 4$, while Troullier and Martins set $n = 10$:

$$p(r) = c_0 + \sum_{i=2}^{n} c_i r^i \tag{2.21}$$

2.1.4 Molecular Dynamics

The Newtonian equation of motion is derived [90] below from the time-dependent Schrödinger equation:

$$i\hbar\frac{\partial}{\partial t}\Phi(\{\mathbf{r}_i\},\{\mathbf{R}_I\};t) = \mathcal{H}\Phi(\{\mathbf{r}_i\},\{\mathbf{R}_I\};t) \tag{2.22}$$

where the Hamiltonian is given by:

$$\begin{aligned}\mathcal{H} &= -\sum_I \frac{\hbar^2}{2M_I}\nabla_I^2 - \sum_i \frac{\hbar^2}{2m_e}\nabla_i^2 + \underbrace{\sum_{i<j}\frac{e^2}{|\mathbf{r}_i-\mathbf{r}_j|} - \sum_{I,i}\frac{e^2 Z_I}{|\mathbf{R}_I-\mathbf{r}_i|} + \sum_{I<J}\frac{e^2 Z_I Z_J}{|\mathbf{R}_I-\mathbf{R}_J|}}_{V_{n-e}(\{\mathbf{r}_i\},\{\mathbf{R}_I\})} \\ &= -\sum_I \frac{\hbar^2}{2M_I}\nabla_I^2 \underbrace{- \sum_i \frac{\hbar^2}{2m_e}\nabla_i^2 + V_{n-e}\left(\{\mathbf{r}_i\},\{\mathbf{R}_I\}\right)}_{\mathcal{H}_e(\{\mathbf{r}_i\},\{\mathbf{R}_I\})} \\ &= -\sum_I \frac{\hbar^2}{2M_I}\nabla_I^2 + \mathcal{H}_e\left(\{\mathbf{r}_i\},\{\mathbf{R}_I\}\right) \end{aligned} \tag{2.23}$$

for the electronic $\{\mathbf{r}_i\}$ and nuclear $\{\mathbf{R}_I\}$ degrees of freedom. The latter three terms on the right hand side of the first expression in Equation 2.23 refer to the bare electron-electron, electron-nuclear, and the nuclear-nuclear Coulombic interactions, respectively.

To solve the Schrödinger equation (Equation 2.22), the total wavefunction $\Phi(\{\mathbf{r}_i\},\{\mathbf{R}_I\};t)$ must be separated into its electronic and nuclear components. Assume that Φ is of the form:

$$\Phi\left(\{\mathbf{r}_i\},\{\mathbf{R}_I\};t\right) \approx \Psi\left(\{\mathbf{r}_i\};t\right)\chi\left(\{\mathbf{R}_I\};t\right) exp\left[\frac{i}{\hbar}\int_{t_0}^{t} dt' \widetilde{E}_e\left(t'\right)\right] \tag{2.24}$$

where the phase factor $\widetilde{E}_e$ is given by:

$$\widetilde{E}_e = \int d\mathbf{r} d\mathbf{R}\; \Psi^*\left(\{\mathbf{r}_i\};t\right)\chi^*\left(\{\mathbf{R}_I\};t\right)\mathcal{H}_e\Psi\left(\{\mathbf{r}_i\};t\right)\chi\left(\{\mathbf{R}_I\};t\right) \tag{2.25}$$

and both the nuclear and electronic wavefunctions are normalized to unity at every instant of time, i.e. $\langle\chi;t|\chi;t\rangle = 1$ and $\langle\Psi;t|\Psi;t\rangle = 1$.

After substituting Equation 2.25 into Equations 2.22 and 2.23, left-multiplying by $\langle\Psi|$ and $\langle\chi|$, respectively, and imposing energy conservation $d\langle\mathcal{H}\rangle/dt \equiv 0$, the resulting equations are:

$$i\hbar\frac{\partial\Psi}{\partial t} = -\sum_i \frac{\hbar^2}{2m_e}\nabla_i^2\Psi + \left\{\int d\mathbf{R}\chi^*\left(\{\mathbf{R}_I\};t\right)V_{n-e}\left(\{\mathbf{r}_i\},\{\mathbf{R}_I\}\right)\chi\left(\{\mathbf{R}_I\};t\right)\right\}\Psi \tag{2.26}$$

$$i\hbar\frac{\partial\chi}{\partial t} = -\sum_I \frac{\hbar^2}{2M_I}\nabla_I^2\chi + \left\{\int d\mathbf{r}\Psi^*\left(\{\mathbf{r}_i\};t\right)\mathcal{H}_e\left(\{\mathbf{r}_i\},\{\mathbf{R}_I\}\right)\Psi\left(\{\mathbf{r}_i\};t\right)\right\}\chi \tag{2.27}$$

These coupled equations are the basis of the time-dependent self-consistent field (TD-SCF) method [53], in which both the electrons and the nuclei move quantum mechanically in time-dependent effective potentials. Note that the electronic and nuclear dynamics are obtained by averaging over the nuclear and electronic wavefunctions, respectively, using quantum mechanical expectation values $\langle\ldots\rangle$. This mean-field description is a consequence of approximating Φ as a simple product of electronic and nuclear wavefunctions.

Next, the nuclei are approximated as classical point particles. This is done by first re-expressing the nuclear wavefunction as:

$$\chi\left(\{\mathbf{R}_I\};t\right) = A\left(\{\mathbf{R}_I\};t\right)exp\left[iS\left(\{\mathbf{R}_I\};t\right)/\hbar\right] \tag{2.28}$$

where A is the amplitude factor and S is the phase, both of which are real and $A > 0$. Equation 2.27 can then be re-expressed as:

$$\frac{\partial S}{\partial t} + \sum_I \frac{1}{2M_I}\left(\nabla_I S\right)^2 + \int d\mathbf{r}\Psi^*\mathcal{H}_e\Psi = \hbar^2\sum_I \frac{1}{2M_I}\frac{\nabla_I^2 A}{A} \tag{2.29}$$

$$\frac{\partial A}{\partial t} + \sum_I \frac{1}{M_I}\left(\nabla_I A\right)\left(\nabla_I S\right) + \sum_I \frac{1}{2M_I}A\left(\nabla_I^2 S\right) = 0 \tag{2.30}$$

Equation 2.29 contains one term that depends on $\hbar$ and A, which vanishes in the classical limit $\hbar \to 0$. The resulting equation is now isomorphic to the equations of motion in the Hamilton-Jacobi formulation:

$$\frac{\partial S}{\partial t} + \mathcal{H}\left(\{\mathbf{R_I}\}, \{\nabla_I S\}\right) = 0 \tag{2.31}$$

with the classical Hamiltonian function:

$$\mathcal{H}\left(\{\mathbf{R_I}\}, \{\mathbf{P_I}\}\right) = T\left(\{\mathbf{P_I}\}\right) + V\left(\{\mathbf{R_I}\}\right) \tag{2.32}$$

defined in terms of the generalized nuclear coordinates $\{\mathbf{R_I}\}$ and their conjugate momenta $\{\mathbf{P_I}\} \equiv \nabla_I S$. The Newtonian equation of motion for the nuclei 2.27 can finally be expressed as:

$$\begin{aligned} \frac{d\mathbf{P}_I}{dt} &= -\nabla_I \int d\mathbf{r}\ \Psi^* \mathcal{H}_e \Psi \\ &= -\nabla_I V_e^E\left(\{\mathbf{R}_I(t)\}\right) \\ &= M_I \frac{d^2\mathbf{R}_I(t)}{dt^2} \end{aligned} \tag{2.33}$$

where the nuclei move classically in an effective potential V_e^E due to the electrons.

The nuclear density $|\chi\left(\{\mathbf{R}_I\}; t\right)|^2$ can be approximated classically as a product of delta functions $\prod_I \delta\left(\mathbf{R}_I - \mathbf{R}_I(t)\right)$ centered at the instantaneous positions $\{\mathbf{R}_I(t)\}$, even though the electrons are treated quantum mechanically. Therefore, in the classical limit, for the position operator:

$$\int d\mathbf{R} \chi^*\left(\{\mathbf{R}_I\}; t\right) \mathbf{R}_I \chi\left(\{\mathbf{R}_I\}; t\right) \overset{\hbar \to 0}{\to} \mathbf{R}_I(t) \tag{2.34}$$

and for the nuclear-electronic potential operator:

$$\int d\mathbf{R} \chi^*\left(\{\mathbf{R}_I\}; t\right) V_{n-e}\left(\{\mathbf{r}_i\}, \{\mathbf{R}_I\}\right) \chi\left(\{\mathbf{R}_I\}; t\right) \overset{\hbar \to 0}{\to} V_{n-e}\left(\{\mathbf{r}_i\}, \{\mathbf{R}_I(t)\}\right) \tag{2.35}$$

Equation 2.26 can thus be re-expressed a time-dependent wave equation for the electrons:

$$i\hbar\frac{\partial\Psi}{\partial t} = -\sum_i \frac{\hbar^2}{2m_e}\nabla_i^2\Psi + V_{n-e}\left(\{\mathbf{r}_i\},\{\mathbf{R}_I(t)\}\right)\Psi$$
$$= \mathcal{H}_e\left(\{\mathbf{r}_i\},\{\mathbf{R}_I(t)\}\right)\Psi\left(\{\mathbf{r}_i\},\{\mathbf{R}_I(t)\}\right) \quad (2.36)$$

The electronic motion is thus coupled to the classical nuclear motion at time t through $V_{n-e}\left(\{\mathbf{r}_i\},\{\mathbf{R}_I(t)\}\right)$.

One main question is how to determine the form of the potential V_e^E. In classical molecular dynamics, the potential is approximated *a priori* as a truncated expansion of many-body contributions:

$$V_e^E \approx V_e^{approx}\left(\{\mathbf{R}_I\}\right) = \sum_{I=1}^{N} v_1\left(\mathbf{R}_I\right) + \sum_{I<J}^{N} v_2\left(\mathbf{R}_I,\mathbf{R}_J\right) + \sum_{I<J<K}^{N} v_3\left(\mathbf{R}_I,\mathbf{R}_J,\mathbf{R}_K\right) + \cdots \quad (2.37)$$

As mentioned previously, this approach fails for simulating reactions involving bond breakage and bond formation.

In Ehrenfest molecular dynamics, Equations 2.33 and 2.36 are solved simultaneously, so that the interatomic forces can be computed from $\nabla_I\langle\mathcal{H}\rangle$ for each configuration $\{\mathbf{R}_I(t)\}$ generated by molecular dynamics. The Ψ used will be the Ψ_0 that initially minimizes $\langle\mathcal{H}_e\rangle$, and will stay in its respective minimum throughout the simulations, even as the nuclei move. Unfortunately, this method is not commonly used today; electronic motion is about 100 times faster than nuclear motion, so the largest possible time step is that which allows the accurate integration of Equation 2.36, about 0.1 fs. The need for extremely small time steps makes the Ehrenfest method impractical for systems with many active degrees of freedom, such as those typically seen in condensed matter problems.

In the Born-Oppenheimer approach, the ground state electronic wavefunction Φ_0 is minimized at each molecular dynamics step, given the set of fixed nuclear positions at that instance in time. The minimization is typically accomplished through repeated matrix diagonalizations of the Hamiltonian of the time-independent elec-

tronic Schrödinger equation:

$$\mathcal{H}_e \Psi_0 = E_0 \Psi_0 \tag{2.38}$$

The time-dependence of the electronic motion is a consequence of the nuclear motion, not intrinsic as in Ehrenfest molecular dynamics. The main disadvantage of Born-Oppenheimer molecular dynamics is that it is computationally intensive since the time-independent Schrödinger equation must be solved self-consistently at each time step.

The ideal MD method should combine the advantages of the Ehrenfest and Born-Oppenheimer approaches: integrate the equations of motion on a long time scale set by the nuclear motion, and take advantage of the smooth time-evolution of the dynamically evolving electronic structure, without having to explicitly diagonalize or minimize the Hamiltonian. The Car-Parrinello approach [26] is an attempt to do this, along with using state-of-the-art electronic structure calculations.

The solution of Equation 2.38 is therefore accomplished not by computationally expensive matrix diagonalizations, but rather by a variation on the simulated annealing method [81]. In this approach, an objective function $\mathcal{O}(\{\beta\})$ is minimized with respect to the parameters $\{\beta\}$ by generating a succession of $\{\beta\}$'s with a Boltzmann-type probability distribution via either a Monte Carlo procedure or molecular dynamics.

In this case, the objective function is the ground-state Kohn-Sham energy functional E^{KS} (Equation 2.1), and the parameters are the coefficients of expansion for the Kohn-Sham orbitals $\{\phi_i\}$, the nuclear positions $\{\mathbf{R}_I\}$, and any external constraints $\{\alpha_\mu\}$ imposed on the system.

Following this, a Lagrangian is postulated:

$$\mathcal{L}_{CP} = \underbrace{\sum_I \frac{1}{2} M_I \dot{\mathbf{R}}_I^2 + \sum_i \frac{1}{2} \mu_i \langle \dot{\phi}_i | \dot{\phi}_i \rangle}_{\text{kinetic energy}} + \underbrace{\sum_\nu \frac{1}{2} \mu_\nu \dot{\alpha}_\nu^2}_{\text{orthonormality}} - \underbrace{E^{KS}\left[\{\phi_i\}, \{\mathbf{R}_I\}, \{\alpha_\nu\}\right]}_{\text{Kohn-Sham energy}} \tag{2.39}$$

The Euler-Lagrange equations are:

$$\frac{d}{dt}\frac{\partial \mathcal{L}}{\partial \dot{\mathbf{R}}_I} = \frac{\partial \mathcal{L}}{\partial \mathbf{R}_I} \tag{2.40}$$

$$\frac{d}{dt}\frac{\partial \mathcal{L}}{\partial \dot{\phi}_i^*} = \frac{\partial \mathcal{L}}{\partial \phi_i^*} \tag{2.41}$$

where $\phi_i^* = \langle \phi_i |$. Then the Car-Parrinello equations of motion on the nuclear positions $\{\mathbf{R}_I\}$ and orbitals $\{\phi_i\}$ are given by Equations 2.43 and 2.42, respectively:

$$\mu_i \ddot{\phi}_i(t) = -\frac{\partial E}{\partial \phi_i^*(t)} + \sum_k \Lambda_{ik}\phi_k(t) \tag{2.42}$$

$$M_I \ddot{\mathbf{R}}_I(t) = -\nabla_{\{\mathbf{R}_I\}} E \tag{2.43}$$

$$\mu_\nu \ddot{\alpha}_\nu = -\frac{\partial E}{\partial \alpha_\nu} \tag{2.44}$$

where μ_i are the "fictitious mass" parameters assigned to the orbital motion, which exists only to perform the simulated annealing optimization, and Λ_{ik} are Lagrange multipliers. By slowly varying the $\{\phi_i\}$'s, $\{\mathbf{R}_I\}$'s, and $\{\alpha_\mu\}$'s, the temperature of the system can be slowly reduced. As $T \to 0$, the equilibrium state of minimal E is reached. The nuclei evolve in time at the physical temperature $T \propto \sum_I M_I \dot{\mathbf{R}}_I^2$, whereas the orbitals evolve according to a "fictitious temperature" $\sum_i \mu_i \langle \dot{\phi}_i | \dot{\phi}_i \rangle$.

In practice, the electrons stay "cold", or close to the ground-state Born-Oppenheimer surface, while adiabatically following the slow motion of the nuclei, which are simultaneously kept at a hot temperature. The use of the fictitious kinetic energy for the electronic orbitals eliminates the need to explicitly diagonalize the Kohn-Sham Hamiltonian. Instead, the equations of motion are solved by integration.

2.2 Reaction Path Finding Methods

2.2.1 Constrained Molecular Dynamics

One search and optimization approach for finding initial reaction paths that has been used successfully [142, 87] is constrained molecular dynamics [27, 37]. The advantage of this method is that only the reactants and some coordinate to drive the reaction need to be specified beforehand; the products appear over the course of the simulations, assuming that the driving coordinate was chosen appropriately. In this approach, the molecular system is taken from the reactants through the transition state to the products by applying a constraint on a putative coordinate, $q(\mathbf{r})$, that defines the progress of the reaction passing from one stable state to another. This coordinate can be as simple as an interatomic distance, angle, asymmetric stretch, or a many-body coordinate. At each $\xi_1 = q(\mathbf{r}_1), \xi_2 = q(\mathbf{r}_2), \ldots$, a molecular dynamics simulation is run in order to obtain an ensemble of configurations in time. In practice, for solid systems in heterogeneous catalysis, the system is initially equilibrated for about 0.5 ps before applying a Nosé-Hoover chain thermostat [102, 89] on the nuclear degrees of freedom, and running a 1 ps simulation at a constant temperature. One picosecond of averaging has been found to be enough to calculate properties such as the force on the constraint with only small statistical uncertainties [87].

The contribution to the free energy F from each constrained reaction coordinate is given by [44]:

$$\frac{\partial F}{\partial \xi_i} = \frac{\langle |Z_\xi|^{-1/2} \left(-\lambda + \frac{kT}{2} \sigma_j \left[Z_\xi \right]_{ij} \left(\nabla' \xi_j \cdot \nabla' log |Z_\xi| \right) \right) \rangle_\xi}{\langle |Z_\xi|^{-1/2} \rangle_\xi} \tag{2.45}$$

where λ is the Lagrange multiplier on the constraint, which is proportional to the negative of the force due to the constraint, and the second term is a correction term that accounts for the variation of an infinitesimal volume element in generalized coordinates.

The elements of the matrix Z_ξ are given by:

$$[Z_\xi]_{ij} = \sum_{k=1}^{N} \frac{1}{m_k} \frac{\partial \xi_i}{\partial x_k} \frac{\partial \xi_j}{\partial x_k} \tag{2.46}$$

For practicality, the following substitution can be made:

$$\nabla' log|Z_\xi| = Tr\left(Z_\xi^{-1} \nabla' Z_\xi\right) \tag{2.47}$$

since it is difficult to take the derivative of $|Z_\xi|$. Also, $\nabla' = \frac{1}{\sqrt{m_i}\nabla}$.

The final expression for relating the change in free energy to the value of each constrained reaction coordinate is:

$$\frac{\partial F}{\partial \xi_i} = \frac{\langle |Z_\xi|^{-1/2} \left(-\lambda + \frac{kT}{2} \sigma_j \left[Z_\xi\right]_{ij} \left(\nabla' \xi_j \cdot Tr\left(Z_\xi^{-1} \nabla' Z_\xi\right)\right)\right) \rangle_\xi}{\langle |Z_\xi|^{-1/2} \rangle_\xi} \tag{2.48}$$

As will be seen later in Section 5.2, if all of the reaction coordinates are based on distances between two atoms, Equation 2.45 reduces to:

$$\frac{\partial F}{\partial \xi_i} = \frac{\langle |Z_\xi|^{-1/2} \left(-\lambda\right) \rangle_\xi}{\langle |Z_\xi|^{-1/2} \rangle_\xi} \tag{2.49}$$

In the case of only one distance-based constraint, Equation 2.49 reduces to:

$$\frac{dF}{d\xi} = -\langle \lambda \rangle_\xi \tag{2.50}$$

When calculating the free energy F, it is assumed that 0.5 ps is enough time for thermal equilibration, so that the all of the degrees of freedom, except for the constrained coordinate(s), are correctly sampled. There may be some barriers to system relaxation such that portions of phase space may not be adequately reached and sampled; in general the computed F is an upper bound to the true F at the transition state.

Also, initially the value of the constrained reaction coordinate is close to its value in the unconstrained system, so the computed F is a good measure of how the free energy of the reactants increases as the value of the reaction coordinate is increased or decreased. Eventually, as the system resembles the product state, the computed F is a

measure of how the free energy of the products depends on the value of the constrained reaction coordinate. However, in the transition state region, the computed F may be slightly lower than the true F since it is an average over the reactant-like and product-like configurations, which are lower in energy than the transition state. Only when the chosen q exactly drives the reaction from reactants to products will the computed F correspond to the true F at the transition state.

2.2.2 Testing the Reaction Coordinate via Calculation of the Committor

Therefore, the validity of the reaction coordinate, q, at describing the movement of the system between free energy states needs to be tested. One way to do this is by calculating the distribution of commitment probabilities, or committors. The committor describes the partitioning of short dynamic trajectories, originating at the assumed transition state region and with randomly chosen initial momenta sampled from a Maxwell distribution, into the various free energy states, in this case A and B [19]; these free energy basins of attraction are characterized by order parameters. If the trajectory ends up in A, meaning that the order parameters corresponding to the final configuration of the trajectory are characteristic of the A basin, the corresponding commitment variables are $P_A = 1$ and $P_B = 0$; conversely, if the trajectory ends up in B, the corresponding commitment variables are $P_A = 0$ and $P_B = 1$.

The assumed transition state region is defined by the configurations along the constrained molecular dynamics trajectories that connect A and B. Therefore, although the initial configuration of the system in the transition state region has one or two coordinates initially set at some value, all atoms are free to move during the molecular dynamics simulations for the committor calculations.

There are four possibilities for the shape of the committor distribution, which can help in determining the correctness of q. If it is unimodal and sharply peaked at $P_A = P_B = 0.5$, as shown in Figure 2-1(b), this means that half of the short

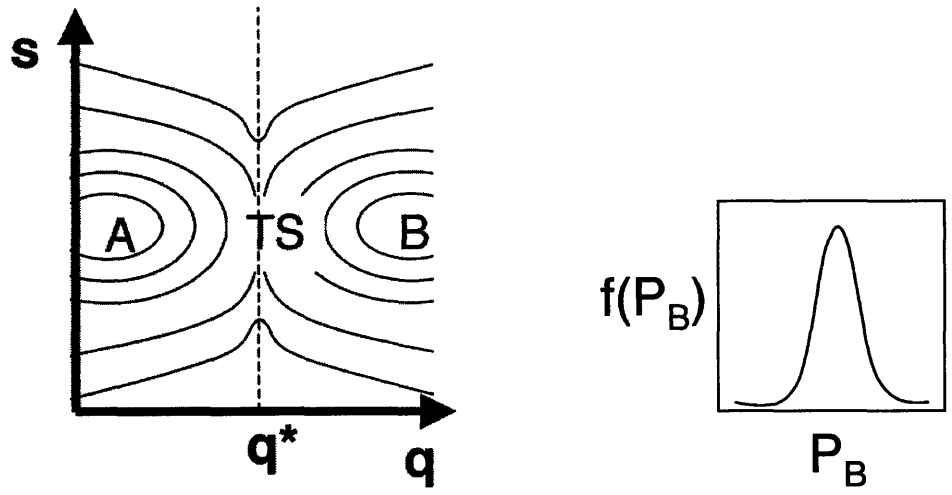

(a) (b)

Figure 2-1: (a) Free energy landscape for systems with dividing surface at $q = q^*$ passing through saddle point only, so linear reaction coordinate can be used to drag system from reactants to products, and (b) Corresponding unimodal committor distribution

trajectories will end up in A and the other half in B. Therefore, a linear reaction coordinate, q, can be chosen that moves in the slowest ascent direction from the reactants to the transition state, passes through a dividing surface at the saddle point ($q = q^*$), and moves in the steepest descent direction from the transition state to the products. All values of $q < q^*$ belong to the reactant free energy basin, and all values of $q > q^*$ belong to the product free energy basin. This situation describes a well-behaved free energy landscape, depicted in Figure 2-1(a), that has been properly captured by q.

The second possibility is for the committor distribution to be bimodal and peaked at both $P_B = 0$ and $P_B = 1$, as shown in Figure 2-2(b). This suggests that the final configuration of each trajectory, i.e. whether it ends up in A or B, depends only on its initial configuration. The corresponding free energy landscape is shown in Figure 2-2(a). The dividing surface at $q = q^*$ actually transgresses both the reactant and product basins, and barely crosses the saddle point, so that a linear reaction coordinate is not adequate for describing this system. In fact, the true reaction

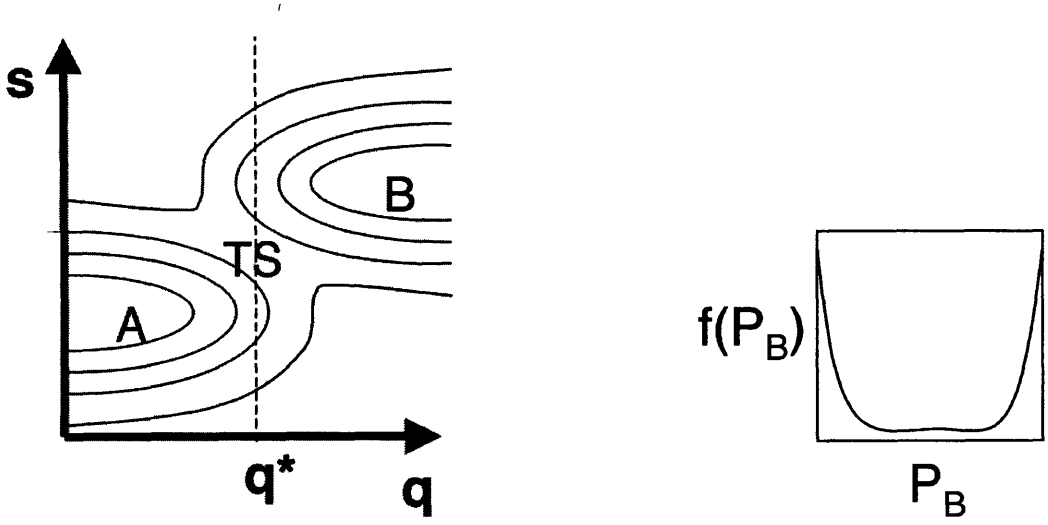

(a) (b)

Figure 2-2: (a) Free energy landscape for systems with dividing surface at $q = q^*$ passing through reactant and product basins in addition to saddle point, so that multiple reaction coordinates are needed to describe the system, and (b) Corresponding bimodal committor distribution

coordinate is likely to be some combination of q and s.

The third possibility is for the committor distribution to be flat across all P_B's. The saddle region is quite broad in the free energy landscape shown in Figure 2-3(a), which suggests diffusive motion along s when $q = q^*$. In the fourth possibility, the committor distribution is skewed in one direction, as reflected by the single peak at either $P_A = 0$ or $P_B = 0$. As shown by the free energy landscape in Figure 2-4(a), the reaction coordinate is orthogonal to q. Almost none of the configurations belonging to any value of q lie on the transition state surface.

Although the shape of the committor distribution can verify the correctness of the chosen reaction coordinate(s), it cannot help in determining more appropriate ones. However, the paths corresponding to $P_A = P_B = 0.5$ can be used as the initial dynamic trajectories used to seed the transition path sampling algorithm. Also, since the transition path sampling algorithm converges toward the correct mechanism, the correct reaction coordinates can be deduced from the dynamic trajectories by observing the structural changes undergone by the reactants.

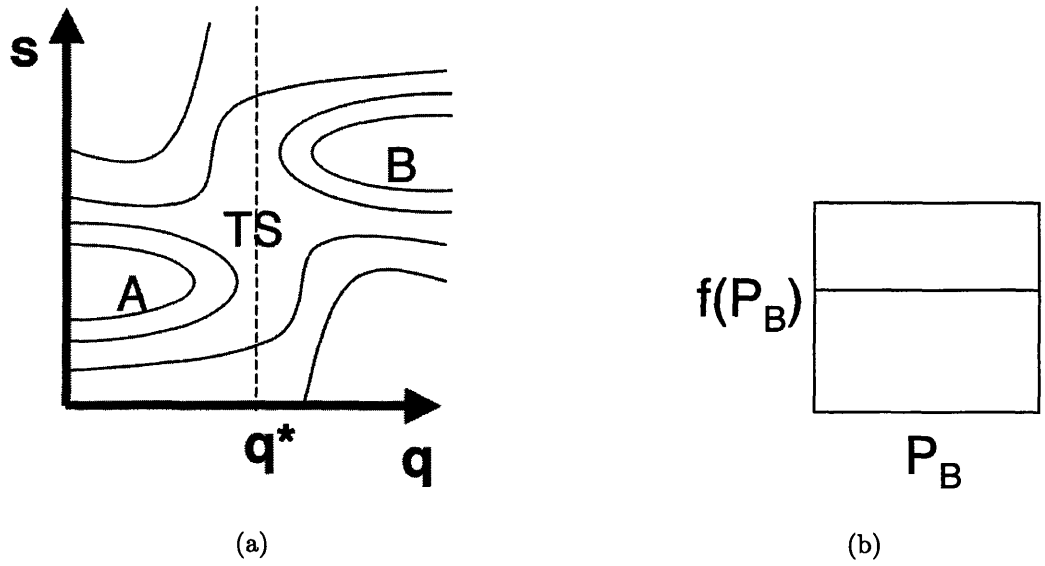

Figure 2-3: (a) Free energy landscape for systems with dividing surface at $q = q^*$ passing through diffuse saddle region, so that multiple reaction coordinates are needed to describe the system, and (b) Corresponding flat committor distribution

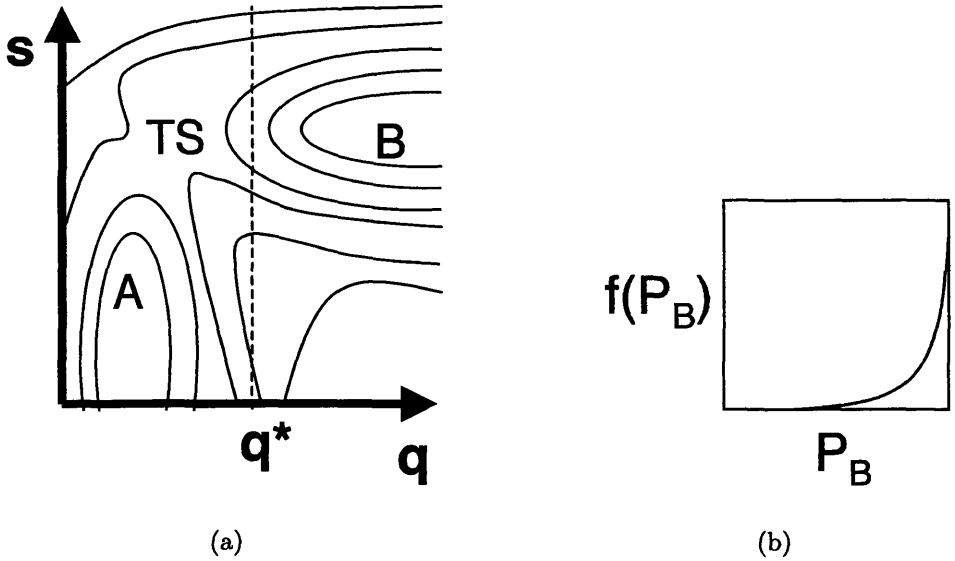

Figure 2-4: (a) Free energy landscape for systems with dividing surface at $q = q^*$ passing through only one free energy basin only, so that the true reaction coordinate is orthogonal to the chosen reaction coordinate and consequently the transition state surface has not been captured, and (b) Corresponding skewed committor distribution

2.2.3 Transition Path Sampling

There are several methods available for obtaining reaction pathways. The traditional approach has been to find transition states, local saddle points, and then follow the imaginary mode to find the reactants and products associated with the transition state. Recent approaches have made use of a two point boundary condition, where the reactants and products are fixed, and a straight line interpolation of images or replicas of the system is initially used to connect these two states. Another method called the nudged elastic band (NEB) [78] works by simultaneously optimizing the configuration of intermediate images along the reaction pathway, which are connected to each other by springs. The method converges toward the minimum energy path (MEP) by projecting out the perpendicular component of the spring force and the parallel component of the true force acting on each image. The NEB method converges quickly given rapid minimization schemes [35], and has been used in numerous applications, including dissociative adsorption at metal surfaces [96], diffusion of water in ice [7], and protein oxidation [36].

The NEB method is particularly useful when accurate Hessians are not available or are difficult to calculate. Convergence, however, can be slow, although new methods help to speed this up [35]. Unfortunately, both reaction mode finding and NEB give information only at a temperature of 0 K, whereas it is likely that the dynamics of the atoms and molecules at finite temperatures will affect the reaction. A more comprehensive approach would involve sampling various dynamic pathways that are representative of the true reaction process. Transition path sampling [31, 48, 46, 18, 47, 19, 17] is such an approach.

Processes in heterogeneous catalysis typically occur over timescales much larger than those directly accessible via molecular simulations. While surface reactions may occur over timescales of 1 μs or larger, molecular simulation methods can probe directly timescales at only ns or even only ps, if quantum mechanical approaches are employed. This wide disparity in timescales poses serious computational difficulties for addressing these "rare events".

Instead of capturing the overall reaction, it is more efficient to focus on the dynamical bottleneck, namely the transition state surface, separating two stable free energy states such as different chemical species, different phases of a condensed material, or different configurations of a polymer. If the location of the transition state is known, then the system can first be moved reversibly to the transition state surface, and from there many short trajectories can be initiated and run to generate an ensemble of dynamic pathways that are representative of the reaction mechanism. This two-step scheme [1, 10, 29, 30] can be used to compute the probabilities for reaching the transition state and successfully crossing the surface, thus giving the rate for the rare event. The transition state is defined as the ensemble of all states through which the system can pass going from reactants to products, not just a single saddle point.

For large systems such as those typically seen in heterogeneous catalysis, the potential energy surface is riddled with a large number of saddle points, the difference in energies of which are roughly on the scale of thermal energies, $k_B T$. All of these must be properly sampled to compute rate constants accurately.

Transition path sampling provides a means of sampling, via a Monte Carlo procedure, trajectories that connect reactants and products. In other words, transition path sampling is a random walk through the ensemble of all paths of time $\mathcal{T}$ that connect the two metastable free energy states A and B. All that is required to begin this random walk is an initial trajectory of time $\mathcal{T}$ that connects A and B. This initial trajectory can be very far from a representative pathway at the temperature of interest, but after an equilibration period, the bias in the algorithm drives the system to the most important regions of trajectory space. The result is an ensemble of dynamic paths, all of the same length, $\mathcal{T}$, which are representative of the true reaction process.

Two ways of generating new trajectories for the Monte Carlo test are shooting and shifting. In a shooting move [18], depicted in Figures 2-5(a) and 2-5(b), a new transition path is created by slightly changing an existing one that connects A and B. First, a time t is randomly chosen on an existing path o. Second, the momentum of the system p_t^o is changed by a small amount δp. In practice, a random atom and

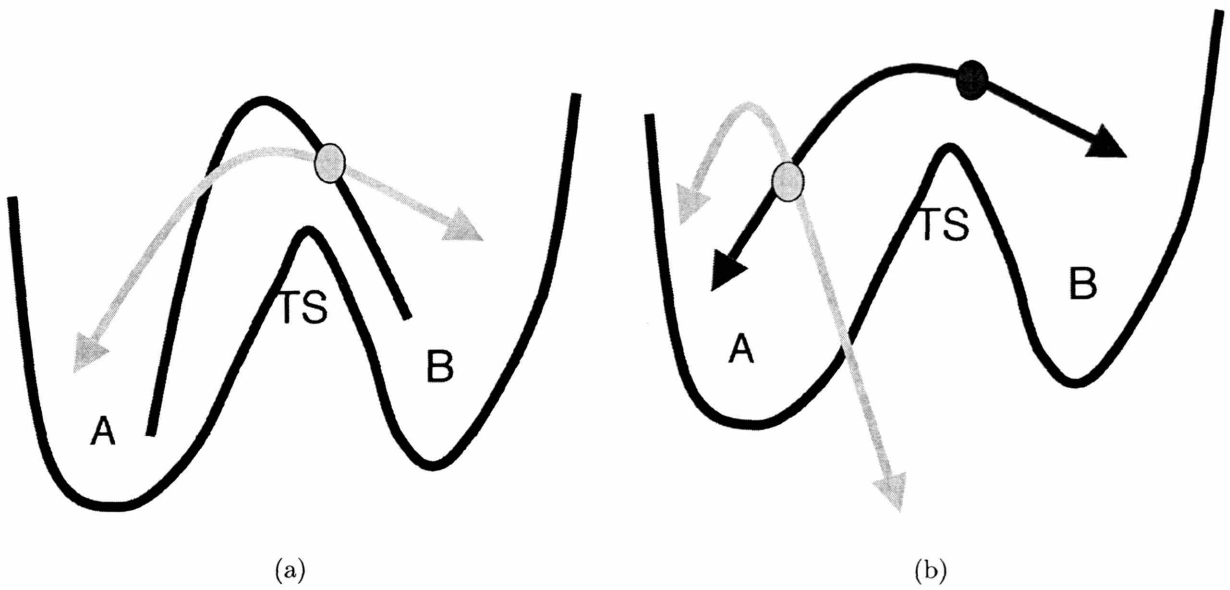

(a) (b)

Figure 2-5: Depiction of shooting algorithm for transition path sampling. (a) Initial dynamic path o (black), random time slice (gray circle) from which molecular dynamics is run forward and backward in time, and new path n (gray) connecting metastable free energy basins A and B, (b) Accepted dynamic path o (black), random time slice (gray circle), and new path n (gray), which is rejected because it does not connect A and B

random velocity component (v_x, v_y, v_z) of that atom are selected, and a new velocity component of that atom is defined such that it lies within a fixed-width Gaussian or Maxwellian distribution of the old velocity component. The velocities of all the atoms are then rescaled so that the total kinetic energy is unchanged. Then, with the new momentum of the system p_t^n, molecular dynamics simulations are run from t backward in time to $t = 0$ and forward in time to $t = \mathcal{T}$. The new path n is then accepted or rejected into the transition path ensemble according to a Metropolis criterion. The new trajectories conserve the total linear and angular momenta of the system, as well as maintaining detailed balance, which means that the probability of generating new momenta from the old set is the same as the reverse probability of generating the old momenta from the new set.

In the particular case where the molecular dynamics simulations are run in the microcanonical ensemble, the Metropolis acceptance probability is 100% if the new path

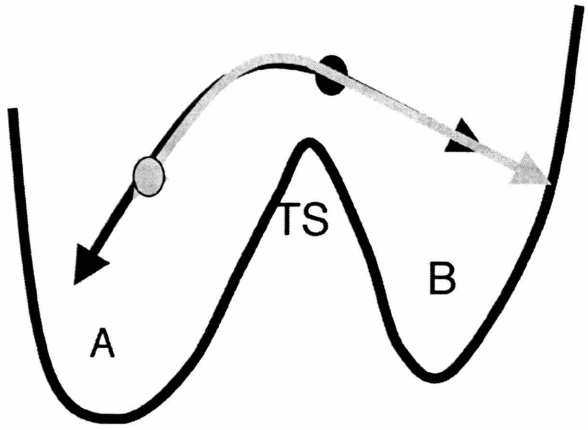

Figure 2-6: Depiction of shifting move for transition path sampling. Accepted dynamic path (black), random time slice (gray circle) from which molecular dynamics is run forward in time, and new path (gray), which is the same length as the old path, and is accepted because it connects A and B

connects A and B, as seen in Figure 2-5(a), and 0% if not, as seen in Figure 2-5(b). This sequence of acceptances and rejections ensures that the correct transition path ensemble is sampled. For efficient sampling, the acceptance of the new trajectories should be around 50%. This can be accomplished by adjusting the magnitude of the momentum displacement δp.

The efficiency of the path sampling can also be enhanced by shifting the paths in time, as shown in Figure 2-6. In a shifting move [18], a segment of length δt is deleted from either the beginning or end of an existing path o that connects A and B. A new trajectory segment of length δt is then grown from the opposite end of the path, so that the new path n is still of the same total length $\mathcal{T}$. In a forward shifting move, n is identical to o for $t = \delta t$ to $t = \mathcal{T}$, and in a backward shifting move, n is identical to o for $t = 0$ to $t = \mathcal{T} - \delta T$. Shifting only selects a slightly translated part of an existing trajectory in order to make the sampling more efficient. However, it is very useful when combined with shooting moves for facilitating convergence of path-averaged quantities. This is particularly true if the shooting algorithm is "stuck" sampling the same path over and over without generating a new accepted trajectory in the transition path ensemble.

Chapter 3

Characterization of Acid Sites in Chabazite

3.1 Introduction

The nature of the acid sites in zeolites and the factors contributing to enhanced catalytic activity have been the subject of much study in the literature. In particular, the issue of whether all of the acid sites in a particular zeolite are homogeneous or heterogeneous in acid strength requires the development of a systematic way to quantify acidity. To address this, a detailed density functional theory (DFT) investigation of the reactivity of the acid sites in the zeolite chabazite is performed. Energies of adsorption of bases, deprotonation energies, and vibrational frequencies are calculated.

The model system used in this study is a chabazite framework that has been modified with chemical and structural defects, in order to determine if there exist intrinsic differences in acid site strengths in the same zeolite, and whether there exists a correlation between the structural properties and the energetics of acid sites. Calculations are presented of four properties: 1. Deprotonation energies, 2. Base adsorption energies, which can be measured experimentally using temperature programmed desorption, 3. O-H vibrational frequencies, which can be probed using infrared spectroscopy, and bond lengths at the acid site, and 4. Topological visualiza-

tion of the electron localization function. In particular, base adsorption energies and O-H vibrational frequencies have been used to quantify differences in acidity between different zeolites, so similar measures can be confidently used to quantify differences in acid strengths in the same zeolite.

The bases studied are methanol, acetonitrile, ammonia, and pyridine. These four bases are chosen in particular because they exhibit a range of basicity and have been studied by other researchers in different contexts using different experimental methodologies [57]. When acetonitrile adsorbs to the acid site, changes in the IR spectrum have been observed [91]. Temperature-programmed desorption of amines, such as ammonia and pyridine, is probably the most widely used method to measure heats of adsorption and the concentration of acid sites. Methanol has been extensively studied theoretically and computationally as an adsorption probe molecule for the acid sites [59, 64, 65, 120, 14, 67, 127, 145, 94]. However, many of the quantum calculations performed on these bases, methanol in particular, use several different zeolite models. The hope is that by performing a large set of calculations using the same methods on chabazite, insight will be gained into the factors affecting zeolite acidity.

3.2 Computational Methodology

In order to calculate properties of the various chabazite structures and electronic energies, density functional theory [72, 83, 104] (DFT) was used. This method allows the computation of energetic and spectroscopic properties with as much accuracy as possible for a large and complex chemical system. The exchange-correlation energy used is the generalized gradient approximation (GGA) of Perdew and Wang (PW91) [110]. Norm-conserving Troullier-Martins pseudopotentials [141] were used to reduce the computational cost relative to all-electron calculations, while maintaining an accurate net charge density for the nuclei and core electrons.

In general, DFT can predict structural properties within 0.05 Å and 1-2 °, overall adsorption and reaction energies within 20-30 kJ/mol, and spectroscopic data within

a few percent of experiment [100]. It is generally considered that relative errors are less than absolute ones, so 10 kJ/mol can be taken as the relative error on energies for this system. The PW91 functional was chosen because it includes interactions between adsorbates and the zeolite framework and gives accurate bond lengths and other structural properties. While dispersive interactions are not included physically, it has been shown that PW91 accurately models van der Waals interactions, for example in Ar-Ar [143] and N_2-N_2 [41] interactions.

All calculations were performed using the Car-Parrinello Molecular Dynamics (CPMD) code, version 3.3 [75]. This code employs a plane-wave basis set with periodic boundary conditions, in order to model chabazite as an infinite crystalline system. A plane-wave cutoff of 55 Ry was chosen to match the cutoffs used by Payne et al. [120, 122], and also because it is quite accurate, as will be seen in Section 3.3.3. Only the Γ point was sampled in the Brillouin zone.

During the geometry optimizations, all atoms, including those in the zeolite framework, were free to move; however, the lattice vectors of the unit cell are fixed. Govind et al. [62] calculated the difference in total energy of faujasite, using a fixed unit cell and a fully optimized cell, to be only 0.2 kJ/mol, so the use of fixed lattice parameters is accurate while reducing the computatonal cost. The main model system contained 1 aluminum T-site per unit cell, for a Si/Al ratio of 11. The presence of only one aluminum substituent, itself a chemical defect, per unit cell allows the consideration of just the interaction between the probe molecule and the acid site and siliceous framework. Chabazite models with 2 Al atoms per unit cell, both in the 8T ring, were also considered, as was a chabazite model with a silanol defect into the framework.

3.3 Results and Discussion

3.3.1 Proton Position on Acid Site Oxygens

First, it is necessary to determine whether there are one or two possible proton positions per acid site. Cook et al. [40] performed calculations on a cluster model

of the T12 acid site of H-ZSM-5, and found only one stable proton position forming a 10° angle with the Al-O-Si plane. Smith et al. [128], however, performed neutron diffraction experiments on chabazite that showed a single proton position situated at an out-of-plane angle of either 45° or 19°, depending on the acid site considered. The results of deuterium NMR experiments on H-ZSM-5 by Kobe et al. [82] suggested a proton out-of-plane angle of 55°. Their results implied that two proton positions per oxygen are possible.

Kobe et al. [82] proposed a model involving motional averaging, whereby the Brønsted acid deuteron can jump between lobes on the sp^3-hybridized oxygen. The justification for this model, as opposed one where an sp^2-hybridized oxygen is in a planar Al-OH-Si structure, is that the latter model cannot produce certain peaks visible in the ^{2}NMR spectrum of ZSM-5. Although the observed Al-OH-Si angles in chabazite (around 130°) are not close to either 120° (sp^2) or 109.5° (sp^3), we can attribute this discrepancy to the distortions in the zeolite lattice when Al is substituted for Si. In order to maximize proton overlap with the oxygen lone pairs, the H atom is restricted to the plane bisecting the Al-O-Si angle.

Two methods were used to evaluate the characteristics of protons in various positions: a topological analysis and a constrained geometry optimization. For the topological analysis, the Electron Localization Function [9, 142] (ELF) was computed, as presented in Equation 3.1. The ELF is normalized between 0 and 1 and describes the probability of finding an electron near another electron with the same spin.

$$ELF = \frac{1}{1+\chi^2} \tag{3.1}$$

$$\chi = \frac{\sum_i |\nabla\psi_i|^2 - \frac{1}{4}\frac{(\nabla\rho)^2}{\rho}}{C\rho^{\frac{5}{3}}} \tag{3.2}$$

The ELF isosurfaces for chabazite with one active site per unit cell are shown in Figure 3-1; $\chi = 0.87$ was chosen for ease of visualization of the lobe features. There is one large lobe corresponding to the most stable proton position, and a much smaller

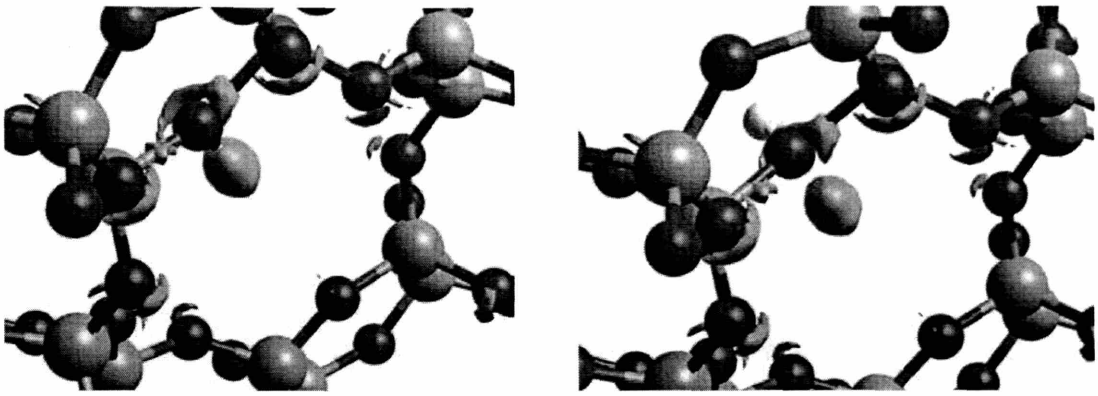

(a) (b)

Figure 3-1: ELF isosurfaces ($\chi = 0.87$) for chabazite with one active site per unit cell. (a) corresponds to out-of-plane angle = 35.7° and (b) corresponds to out-of-plane = -39.5°, where the proton is situated out of the Al-O-Si plane

U-shaped lobe corresponding to a possible metastable proton position. This suggests that there may be two possible proton positions.

Geometry optimizations were then performed on the chabazite structure, constraining the proton position at various out-of-plane angles relative to the Al-O-Si plane. The total energy of chabazite as a function of out-of-plane angle is shown in Figure 3-2, with the reference zero energy corresponding to the optimized structure without constraints. There are two minima: a deeper minimum at an out-of-plane angle of 35.7° corresponding to the optimized structure, and a shallower minimum, approximately 6.30 kJ/mol less stable, at an out-of-plane angle of -39.5°, as indicated by the ELF isosurfaces. The magnitude of the out-of-plane angle of the more stable position is consistent with the results of Smith et al. [128], but higher than the calculated 13.7° out-of-plane angle of Jeanvoine et al. [76] for the O3 site. The out-of-plane angles corresponding to the two minima are similar in magnitude, and thus are further evidence supporting the sp^3-hybridized model for oxygen, with its lone pairs symmetric across the Al-O-Si plane.

A similar study of the O2 acid site was performed, and the most stable proton position was found to form a 8.68° angle with the Al-O-Si plane; this value compares

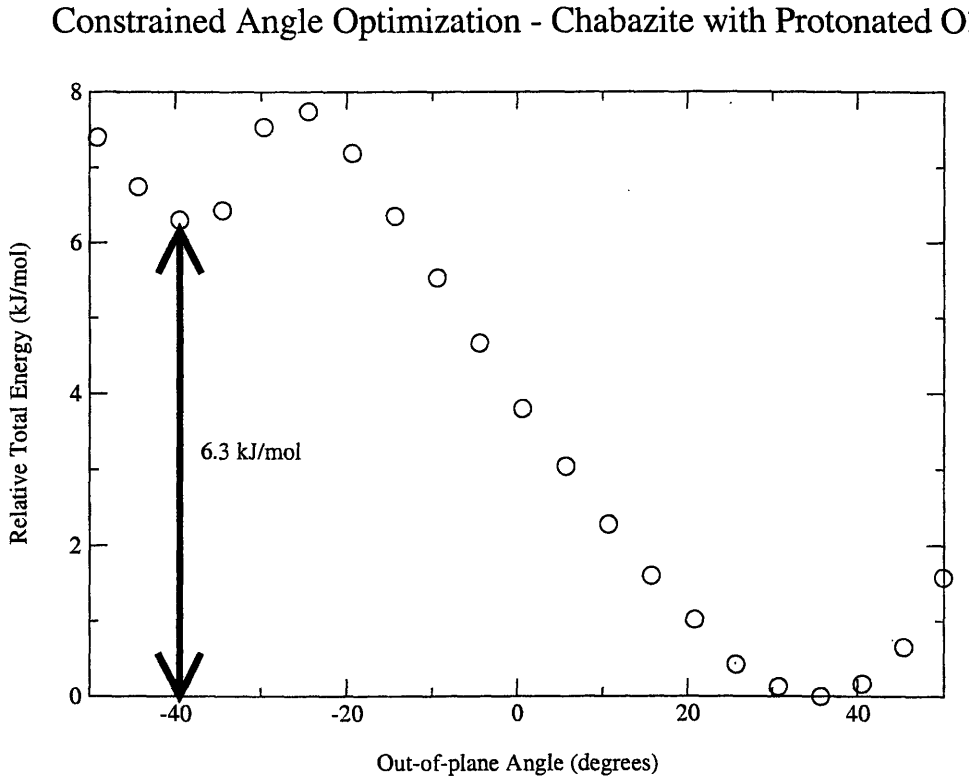

Figure 3-2: Total energy (kJ/mol) vs. constrained proton out-of-plane angle for chabazite with proton at O3

more favorably to the 11.6° angle calculated by Jeanvoine et al. [76] for the O2 site, and the 10° angle found by Cook et al. [40] for ZSM-5. A second, much less stable, proton position was also found for the O2 site. In conclusion, it is likely that there are two minima for a proton position at each acid site, though one of these proton positions is more energetically stable than the other.

3.3.2 Deprotonation Energy and Stability of Acid Sites

The deprotonation energies of each of the four possible acid sites corresponding to the single aluminum substituent were calculated, as shown in Figure 3-3 and numbered O1-O4 according to the chabazite topology labeling [25]. In this labeling scheme, sites O2 and O3 are part of the large 8T ring, while sites O1 and O4 are part of the smaller 6T ring. There have been several published studies aimed at understanding the properties of the zeolite acid sites and quantifying differences between the four oxygen acid sites [128, 120, 67, 94, 76, 121, 22, 140].

Selected geometric parameters, including the O-H bond length and the Al-O-Si bond angle at each of the protonated acid sites, and energetic parameters, including proton affinities and O-H vibrational stretching frequencies, are shown in Table 3.1. All vibrational frequencies were calculated using the harmonic approximation from finite differences of first derivatives. Although it has been shown by Mihaleva et al. that anharmonic effects must be included for the most accurate comparison to experimental stretching frequencies, the relative ordering of the harmonic and anharmonic fundamentals between the four acid sites is not changed [95]. The experimental O-H stretching frequencies on chabazite are 3603 cm^{-1} and 3579 cm^{-1} at the O1 and O3 sites, respectively [128]. A comparison of the calculated relative energies in this study to other published studies is shown in Table 3.2.

The neutron diffraction results of Smith et al. [128] suggest that protons are observed only on O1 and O3. Although most of the other researchers find that the O1 site is the most stable, the results of this study were such that the O2 site is the most stable. The difference between these results and those of other researchers is likely due to slight differences in methodology. The difference in deprotonation energy

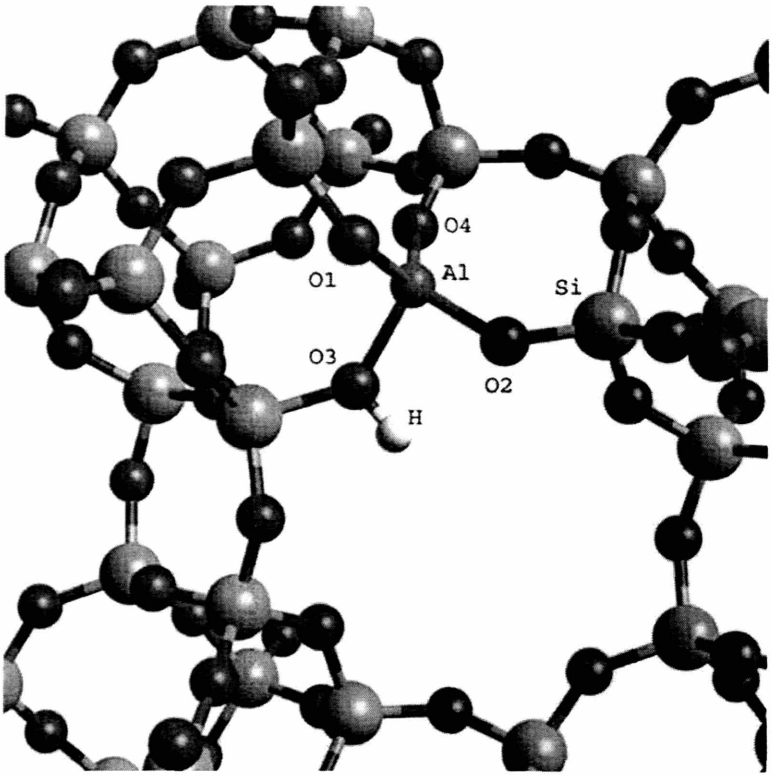

Figure 3-3: Four non-equivalent oxygen acidic sites in chabazite

Table 3.1: Selected geometric and energetic parameters at the four tetrahedral acid sites in chabazite (1 Al/unit cell)

Acid Site	Al-O-Si Bond Angle (°)	O-H Bond Length (Å)	Deprotonation Energy (kJ/mol)	O-H Vibrational Frequency (cm^{-1})
O1	129.8	0.977	1178.7	3578
O2	133.5	0.979	1180.9	3541
O3	130.9	0.980	1174.6	3514
O4	134.6	0.980	1179.1	3532

between the O2 and O1 sites is only about 2 kJ/mol. Also, the results of the current study are compared to those of the other researchers, no distinct trends are seen in the stability of the other acid sites. Therefore, these results imply that the four acid sites have approximately the same stability, within the accuracy of the calculations.

Also, the small differences in the magnitude and the order of the deprotonation energies among the results in Table 3.2 can be attributed to differences in models and methodology. The range of relative energies of the four acid sites is around 6-10 kJ/mol, which corresponds to an energy difference of $2k_BT$ at 400 °C. Functional approximations to the exchange and correlation energies are used, and since the absolute accuracy of the energies calculated with DFT has been shown to be about 20-30 kJ/mol [100], 10 kJ/mol can be taken as a good estimate of the relative accuracy of the energies among the four acid sites. Other small sources of inaccuracy in the calculations may include the use of fixed unit cell lattice parameters instead of letting the system volume relax as well, and the incomplete basis sets used. Also, the energy surface is likely to be highly corrugated so that there are many local minima. Current, state of the art geometry optimization methods (i.e. direct inversion of the iterative subspace, steepest descent, and preconditioned conjugate gradients) can only guarantee convergence to a local minimum. In Section 3.3.1 it was shown that the difference in relative total energies between the local and global minima is around 6.3 kJ/mol. Perhaps some of the differences in acid site energies can be attributed to not fully optimizing the zeolite framework structures, especially if the PW91 functional is unable to adequately treat the negative charge of the chabazite anion in the calculation of the deprotonation energies.

By just considering deprotonation of each unit cell, a divergent Coulomb term is being introduced in the lattice energy, which is unphysical. This can be rectified by adding a uniform positive background charge to the deprotonated unit cell. Eichler et al. [54] compared the deprotonation energy for the removal of a single proton from a single unit cell and a double (2x1x1) supercell, where only one active site is protonated per cell. The deprotonation energy changes by only 1.6 kJ/mol. There are also small errors introduced by the different structural relaxation when one or two

Table 3.2: Comparison of relative deprotonation energies between different acid sites in chabazite (1 Al/unit cell), calculated by us and various researchers

	Relative Energies (kJ/mol) of Acid Sites			
	O1	O2	O3	O4
This work	**2.2**	**0**	**6.3**	**1.8**
Shah [120] (periodic)	0	6.8	3.9	8.6
Shah [121] (periodic)	0	7.7	4.8	13.5
Haase [67] (periodic)	0		9.5	
Jeanvoine [76] (periodic)	0	8.8	5.2	5.0
Brändle [22] (embedded cluster)	0	17.0	12.9	12.5
Mihaleva [94] (cluster, Gaussian98)	1.5	5.0	5.7	0
Mihaleva [94] (cluster, DGauss)	0	1.7	2.8	0.8
Treesukol [140] (embedded cluster)	0	15.8	16.7	15.9
Smith [128] (exp)	*		*	

acid sites are deprotonated in the 2x1x1 supercell, but these should not affect these results appreciably.

Although it has been shown in the studies of both Smith et al. [128] and Vitale et al. [146] that the O1 and O3 sites are the only protonated sites in chabazite, based on our energetic studies the O2 and O4 sites seem to be the most stable. It is not possible to explain why only the O1 and O3 protons are observed experimentally, so factors outside of the scope of these calculations must be involved.

The most likely explanation is that all four acid sites at a given aluminum substituent in chabazite have approximately the same deprotonation energy, and therefore are roughly homogeneous in acid strength.

3.3.3 Adsorption of Bases

Adsorption energies on chabazite were calculated for four bases: acetonitrile, methanol, ammonia, and pyridine. The weak bases acetonitrile and methanol were chosen because they are commonly used in hydrogenation reactions involving zeolites. Ammonia and pyridine were chosen because they are commonly used as base probes in temperature programmed desorption, a widely used experimental method for characterizing zeolite acidity. The adsorption of these bases on O3-protonated chabazite

Table 3.3: Calculated and literature values for proton affinities (kJ/mol) of base adsorbates used in this study

Base	Proton Affinities (kJ/mol) of Base Adsorbate		
	This work	Aue and Bowers [2] (exp)	Error
Acetonitrile	805.3	798.7	6.6 (0.8%)
Methanol	757.1	773.6	-16.5 (2.1%)
Ammonia	877.3	857.7	19.6 (2.3%)
Pyridine	957.8	922.2	35.6 (3.9%)

Table 3.4: Adsorption energies (kJ/mol) of bases on chabazite (1 Al/unit cell)

Acid Site	Adsorption Energies of Bases (kJ/mol)			
	Acetonitrile	Methanol	Ammonia	Pyridine
O1	82.7	94.0	149.3	153.6
O2	83.6	91.6	142.9	161.2
O3	69.7	91.7	144.5	153.5
O4	79.4	90.9	135.7	162.6

is illustrated in Figure 3-4.

The gas-phase proton affinities of the four bases are given in Table 3.3. Ammonia and pyridine have much higher proton affinities than acetonitrile and methanol, and ammonia and pyridine are able to induce proton transfer from the chabazite framework.

The adsorption energies of bases on chabazite are given in Table 3.4, and a comparison of our results to the ranges reported in the literature from both calculated and experimental results is shown in Table 3.5 for methanol and ammonia adsorption. The adsorption energies of ammonia and pyridine are about 60 kJ/mol higher than those of acetonitrile and methanol; this suggests that higher gas-phase base proton affinities, and the corresponding proton transfer reactions, result in more strongly bonded zeolite-base complexes. This trend was also seen by Biaglow et al. [12], who showed that the heats of adsorption of amines in H-ZSM-5 scaled with their gas-phase proton affinities.

The stability trend, in order from most stable to least stable, of the zeolite-base

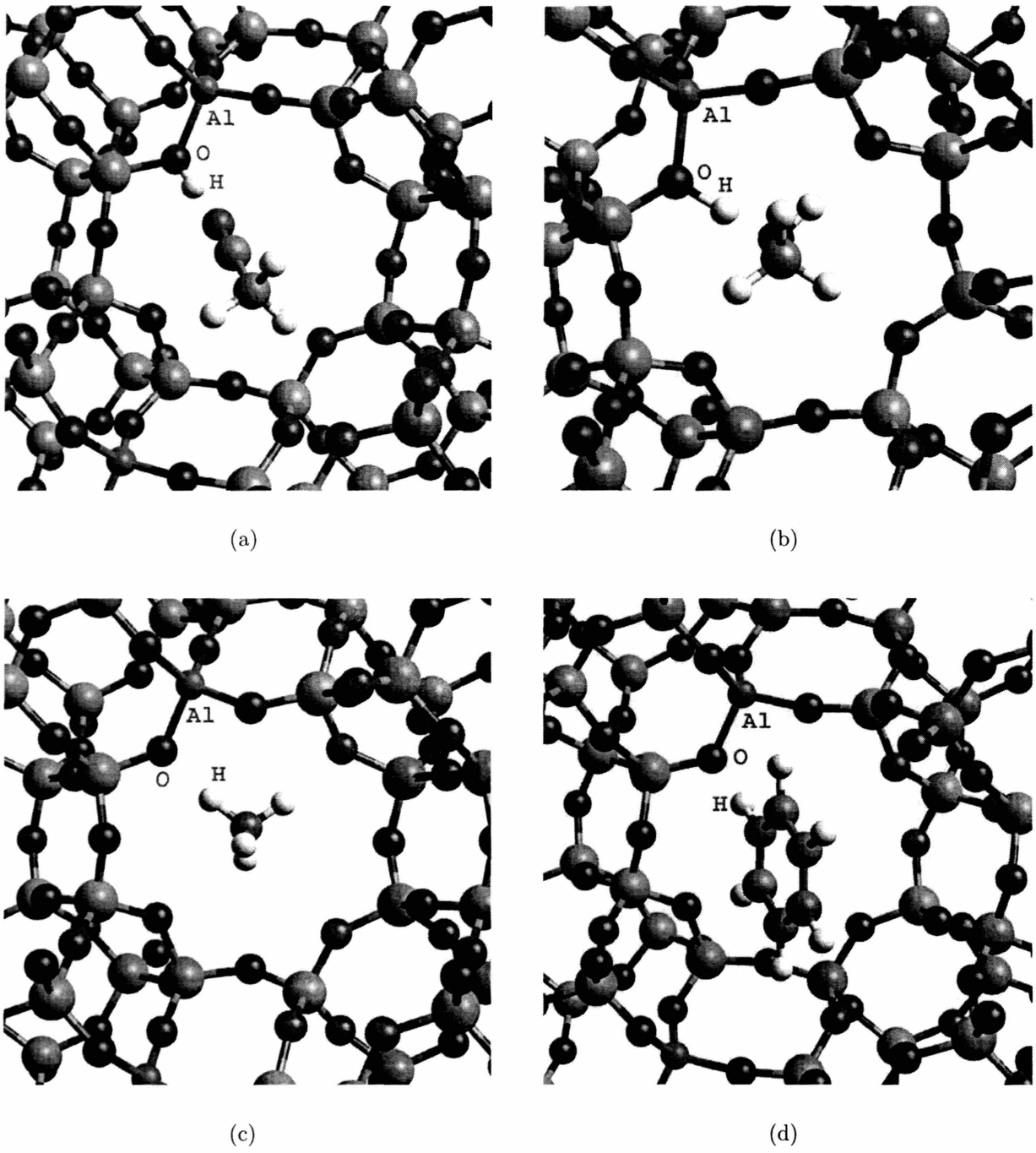

Figure 3-4: (a) Acetonitrile, (b) Methanol, (c) Ammonia, (d) Pyridine adsorbed to chabazite with proton on O3

Table 3.5: Comparison of our calculated adsorption energies of methanol and ammonia on chabazite (1 Al/unit cell) to those calculated or measured experimentally by other researchers

	Adsorption Energy of Bases (kJ/mol)	
	Methanol	Ammonia (kJ/mol)
This work	90.9-94.0	135.7-149.3
Gale [59] (cluster)	63.5-79.8	
Shah [120] (periodic)	82	
Haase [67] (periodic)	93.6-94.1	
Mihaleva [94] (cluster)	96-105	
Sauer [22, 21] (embedded cluster)		100-109
Truong [147] (embedded cluster)		166-190
Messow [92] (HZSM-5, exp)	63	
Haase [65] (HZSM-5, exp)	120	
Dumesic [123] (HZSM-5, exp)		150
Gorte [105] (HZSM-5, exp)		150
Derouane [52] (HZSM-5, exp)		145
Joly [77] (HY, exp)		125

complexes is shown in Equation 3.3:

$$\begin{aligned} Acetonitrile &: O2 > O1 > O4 > O3 \\ Methanol &: O1 > O3 > O2 > O4 \\ Ammonia &: O1 > O3 > O2 > O4 \\ Pyridine &: O4 > O2 > O1 > O3 \end{aligned} \tag{3.3}$$

This suggests that geometric factors are important; the smaller bases, ammonia and methanol, are slightly more stable when situated in smaller channels and hence adsorbed to the O1 site, whereas the larger bases, acetonitrile and pyridine, prefer to be situated in the 8T ring and thus adsorbed to the O2 site. Derouane et al. [50] also proposed in a model for confinement effects that bases prefer to adsorb in the smallest pores that can accomodate them, in order to maximize their van der Waals interactions with the zeolite framework, and we do see a slight size dependence in our results. A similar trend is not seen among bases of similar strengths, but rather among bases of different sizes, for example acetonitrile and methanol. It is

also important to note that the relative stabilities differ only by 10 kJ/mol, which is within the accuracy of the DFT calculations so most likely any trends are not significant (see Section 3.3.2) and the bases do not actually prefer one acid site over another, as demonstrated by ammonia TPD experiments [123, 105].

In conclusion, there is a definite correlation between base adsorption energies and gas-phase proton affinities, and there may be a correlation between base size and the preferred zeolite acid site for adsorption. However, for a given base, the difference in adsorption energies between the four acid sites is very low.

3.3.4 Concentration of Framework Substituents

The ratio of Si/Al in industrial chabazite is about 4.5 [150]. In the model chabazite system described in the previous sections, there is only one Al site per unit cell, giving a Si/Al ratio of 11. It is therefore important to determine how the base adsorption energy varies as a function of the concentration of Al substituents in the silicate framework. Three models of chabazite with 2 Al/unit cell were thus constructed. The two aluminum atoms cannot be separated by only one oxygen atom by Loewenstein's rule [88], so there are three possible configurations for the two aluminum substituents around the 8T ring, as shown in Figure 3-5; only the 8T ring was chosen for the location of the additional aluminum substituent in order to isolate the effect of the extra electronic charge from any steric effects. These structures are designated as "ortho", "meta", and "para", analogous to the nomenclature used for aromatic compounds. In all three cases, the O3 proton from Section 3.3.2 was chosen to be protonated to match that given in the original chabazite coordinates of Smith et al. [128], in order to have these 2 Al/unit cell models start from the same base structure as for the 1 Al/unit cell models and not propagate any errors in the geometry optimizations. It is anticipated that the deprotonation energies on chabazite with 2 Al/unit cell and O1 as the protonated site are not vastly different from those with O3 as the protonated site, since the acid sites in chabazite have roughly similar deprotonation energies, as seen in Section 3.3.2. The proton affinities and O-H vibrational frequencies for all three structures are shown in Table 3.6. The "ortho" and "para" configurations, with

Table 3.6: Deprotonation energies and O-H vibrational frequencies at the two acid sites in chabazite (2 Al/unit cell)

2 Al Configuration	Deprotonation Energy (kJ/mol)	O-H Vibrational Frequency (cm^{-1})
O3 and O1 ("ortho")	1190.4 (O3)	3557
	1176.0 (O1)	3542
O3 and O2 ("meta")	1167.5 (O3)	3544
	1153.5 (O2)	3581
O3 and O3 ("para")	1188.5 (O3)	3576
	1191.7 (O3)	3588
O3 only	1175	3514

their perfectly symmetric distribution of Al substituents around the 8T ring, were found to be more stable than the "meta" configuration. Barbosa and van Santen also found that the "ortho" and "para" structures, with a $[ZnOZn]^{2+}$ cluster instead of two protons as the charge neutralizers, were more stable than the corresponding "meta" structure [4].

The adsorption energies of acetonitrile, methanol, ammonia, and pyridine on these three structures, as illustrated in Figure 3-5, are shown in Table 3.7, and compared to the analogous base adsorption energies on chabazite with 1 Al/unit cell with the proton on O3 (henceforth referred to as "CHA"). For methanol, as shown in Figure 3-6, a slight increase in adsorption energy is seen when comparing "ortho" to "meta" to "para"; there does not seem to be a similar trend trends in the adsorption energies for acetonitrile. There may be small geometrical or steric factors that affect the methanol adsorption energy. The methanol C-O bond does not lie in the plane of the two chabazite protons in "ortho", but does lie in the plane in "meta" and "para". In "ortho", since the chabazite protons are only 3.29 Å apart and in close proximity to the methanol proton, there may be some repulsive interactions that slightly destabilize the chabazite-methanol complex. By comparison, the chabazite protons are more than 4.0 Å apart in the "meta" and "para" structures. The two framework protons in "ortho" and "para" are roughly equidistant to the framework oxygen closest to the O-H and N-H groups of methanol and ammonia, respectively, so the symmetric

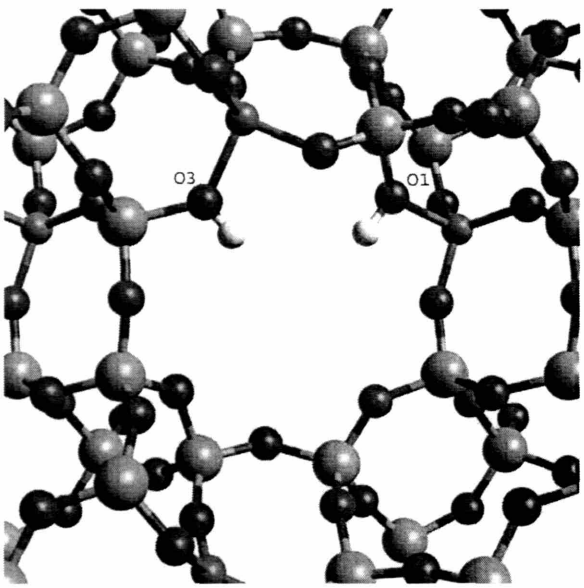

(a)

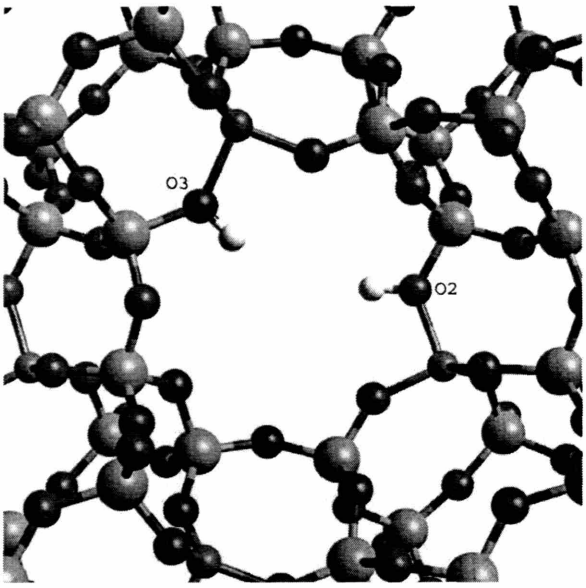

(b)

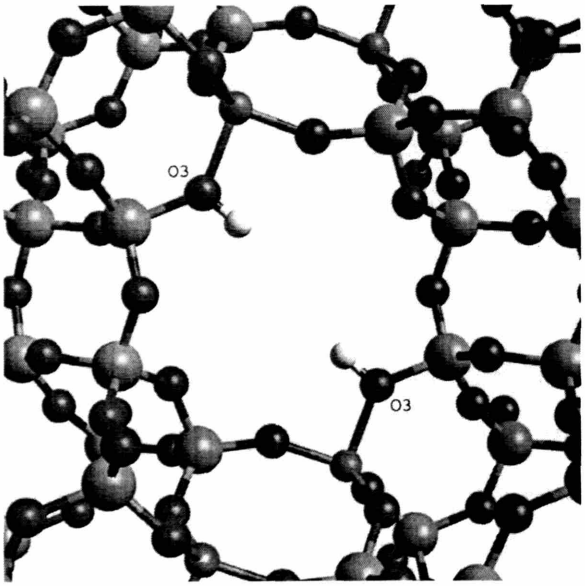

(c)

Figure 3-5: Chabazite with 2 Al/unit cell, with protons on: (a) 'O3 and O1 ("ortho"), (b) O3 and O2 ("meta"), and (c) O3 and O3 ("para")

Table 3.7: Adsorption energies of bases on chabazite with 1 Al/unit cell and 2 Al/unit cell

2 Al Configuration	Base Adsorption Energy (kJ/mol)			
	Acetonitrile	Methanol	Ammonia	Pyridine
O3 and O1 ("ortho")	72.3	80.1	140.9	150.4
O3 and O2 ("meta")	64.0	88.0	144.1	152.2
O3 and O3 ("para")	69.1	97.5	125.6	147.4
O3 only	69.7	91.7	144.5	153.5

structural topology and corresponding electronic density may help to stabilize the base. However, the extra strain in the "ortho" structural framework that arises from the Al atoms being in close proximity may work to slightly destabilize the base.

The adsorption energies of ammonia and pyridine on "ortho" and "meta" are similar in magnitude to the adsorption energies of ammonia and pyridine on our structure with 1 Al/unit cell, with "ortho" being slightly lower due to steric effects. This was also seen by Meusinger and Corma [93], who observed that acid strength, as measured by proton transfer reactions, decreased for zeolites with two AlO_4 tetrahedra separated by only one SiO_4 tetrahedra, which is similar to our "ortho" case. Also, for both of these bases, the adsorption energy on "para" is slightly lower. As shown in Figure 3-7 and Table 3.8, the optimized non-acidic proton positions are almost identical for the three structures, with out-of-plane angles ranging from -43.1 to -52.0°. During the process of ammonia adsorption, the non-acidic proton distorts to minimize the Coulombic repulsion with the ammonium ion. Hence the optimized structures of the acid site containing the non-acidic proton are roughly identical for all three structures, yet when the base is present, the framework distortion leads to some variation in the base adsorption energies.

The range of adsorption energies in Table 3.7 is below 10 kJ/mol for both large-sized bases acetonitrile and pyridine, whereas the range of adsorption energies is between 15-20 kJ/mol for the smaller bases methanol and ammonia. In Section 3.3.3, confinement effects were shown to be important, so the smaller bases may be affected by the positioning of the acid site protons around the 8T ring, and thus the strength

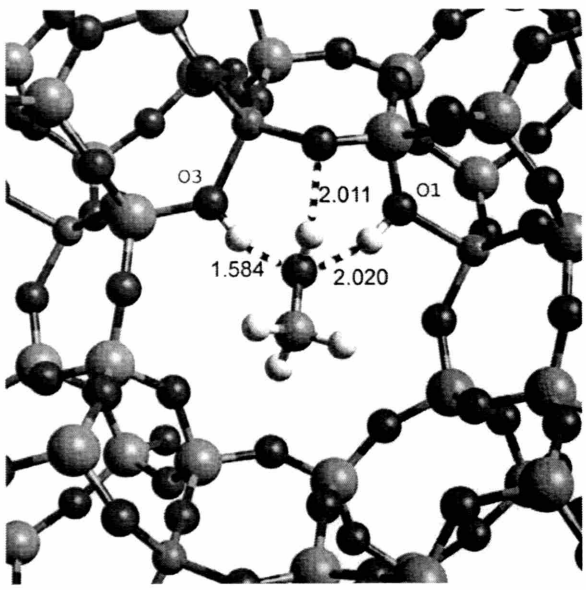

(a)

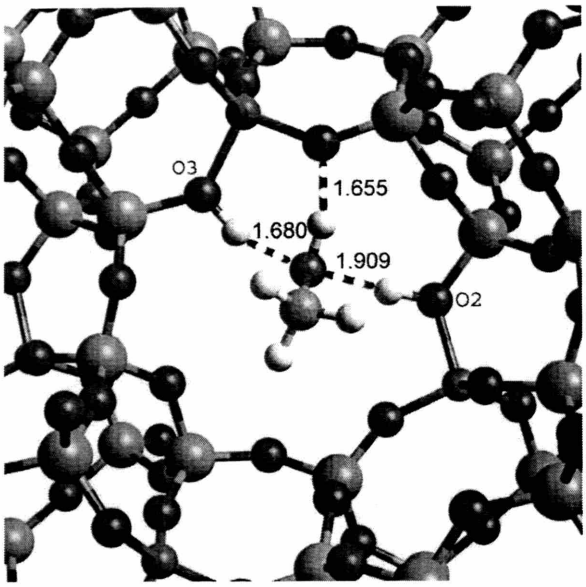

(b)

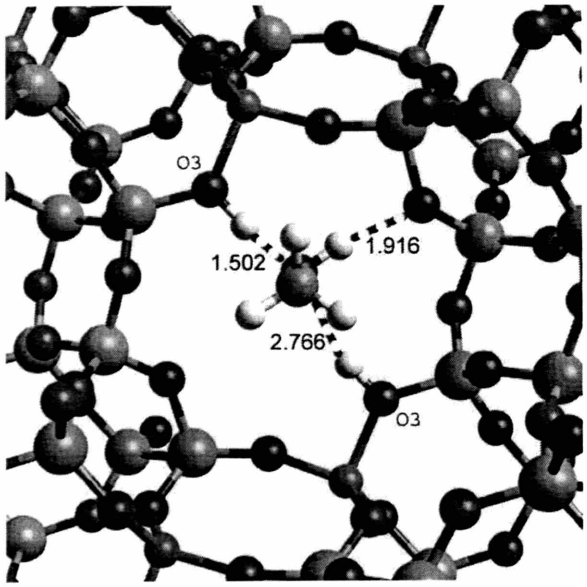

(c)

Figure 3-6: Methanol adsorbed on chabazite with 2 Al/unit cell, with protons on: (a) 'O3 and O1 ("ortho"), (b) O3 and O2 ("meta"), and (c) O3 and O3 ("para")

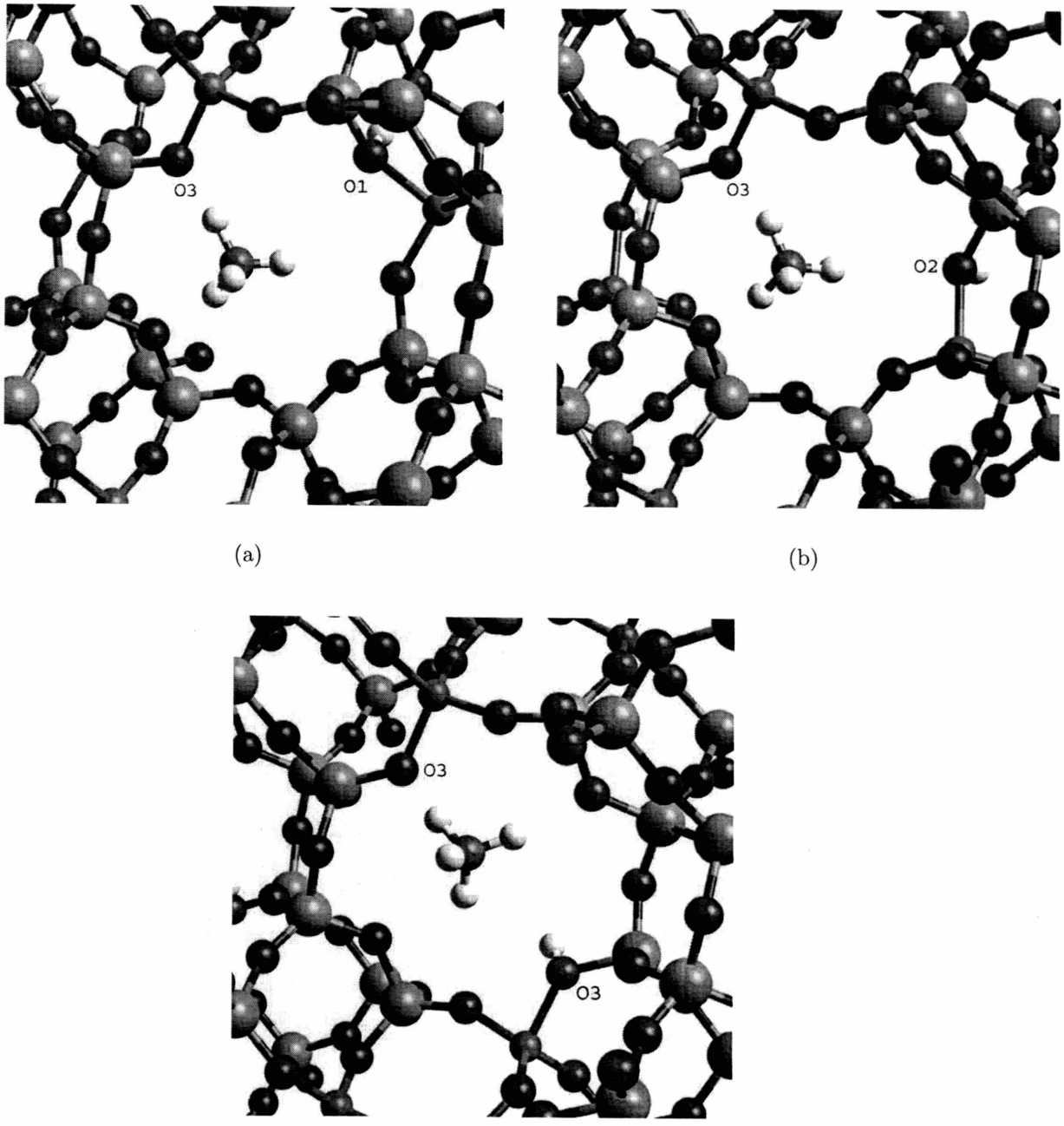

Figure 3-7: Ammonia adsorbed on chabazite with 2 Al/unit cell, with protons on: (a) 'O3 and O1 ("ortho"), (b) O3 and O2 ("meta"), and (c) O3 and O3 ("para")

Table 3.8: Non-acidic chabazite proton out-of-plane angle with and without ammonia adsorbed to chabazite framework

2 Al configuration	Out-of-plane Angle (°)	
	CHA only	CHA-NH_3
O3 and O1 ("ortho")	28.7	-52.0
O3 and O2 ("meta")	23.3	-49.8
O3 and O3 ("para")	-11.9	-43.1

of the hydrogen bonds stabilizing the zeolite-base complex.

An ELF visualization was then performed on the optimized "ortho", "meta", and "para" structures with ammonia. In Figure 3-8, the ELF lobe on the acidic oxygen is smaller in "para" than in either "ortho" or "meta". This indicates a slightly reduced acid strength for "para" that could explain the slightly lower ammonia adsorption energy.

Experimentally, it has been shown that in high silica zeolites (Si/Al > 10) such as ZSM-5, catalytic activity, as measured by the rate of hexane cracking, increases linearly with Al content [63]; in essence, the catalytic activity per acid site remains constant. Even for low silica zeolites such as faujasite (Si/Al > 4.5), the activity per Al atom is constant [45]. Only for very low-silica zeolites does the specific activity increase with decreasing aluminum content. In this work, Si/Al ratios of 11 and 5 were studied in the chabazite models. Methanol and ammonia were used to probe only one acid site, although there were two acid sites in the framework. Although the results suggest that the strength of the acid sites in chabazite, as measured by the energies of adsorption of small bases, is also constant amidst changes in Al content in the framework, it must be stressed that acidity is not necessarily a measure of catalytic activity.

In conclusion, although there are some variations, roughly 5-17 kJ/mol, in the adsorption energies on "ortho", "meta", and "para", for all bases, there are no consistent trends that seem to be universally applicable, and the presence of additional aluminum substituents does not significantly affect the strength of any individual acid site.

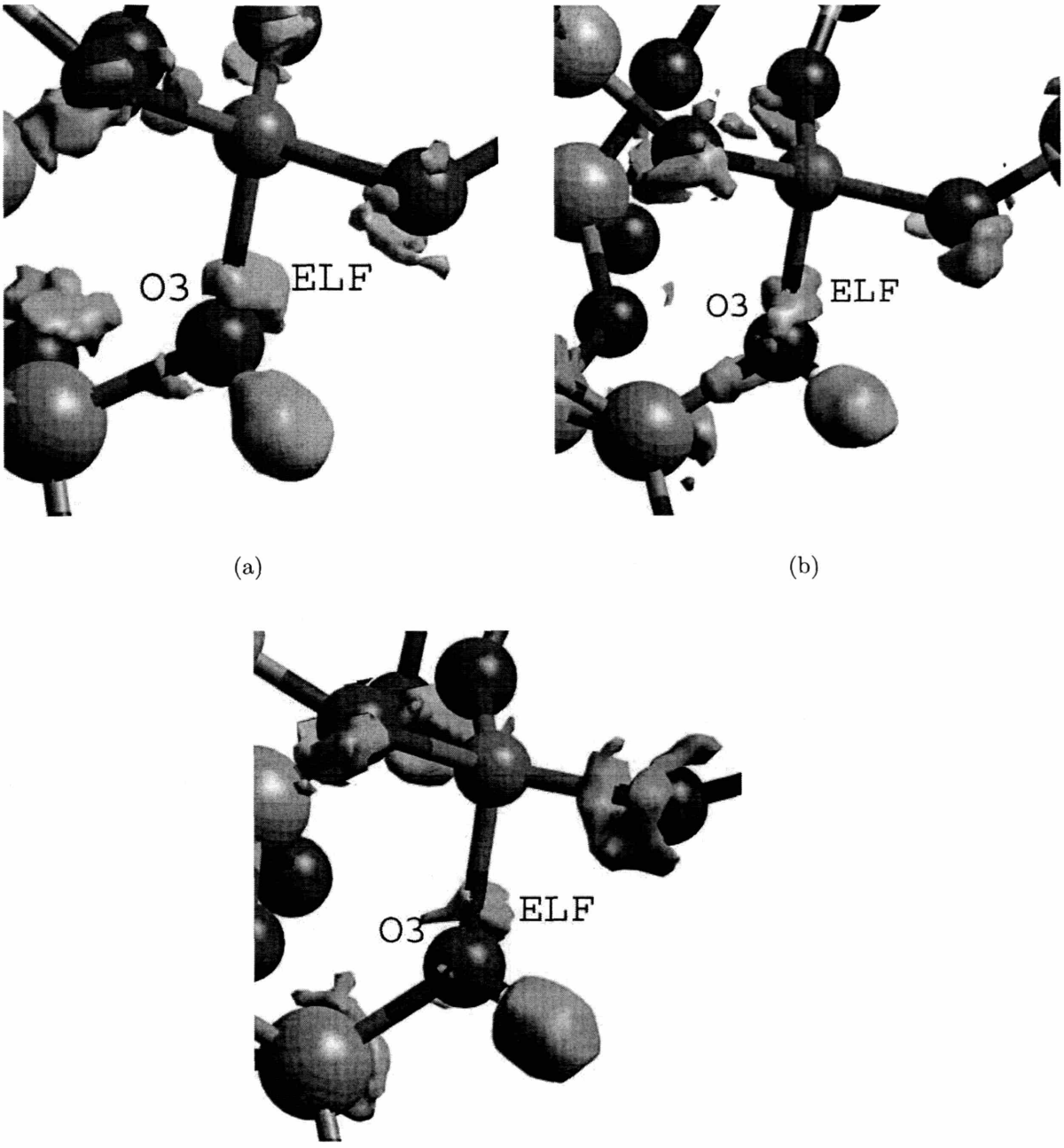

(a) (b)

(c)

Figure 3-8: ELF isosurfaces ($\chi = 0.87$) on O3 proton of chabazite with 2 Al/unit cell, with protons on: (a) 'O3 and O1 ("ortho"), (b) O3 and O2 ("meta"), and (c) O3 and O3 ("para")

3.3.5 Framework Defects

Finally, the effect of the presence of zeolite framework defects on the strength of acid sites was investigated. Both the natural and synthetic environments of chabazite contain significant amounts of water, which is either physisorbed or chemisorbed to the framework [130]. During the synthesis of chabazite, two nonbridging siloxy (≡Si-O-) species associated with the adamantane templates [150] can undergo calcination and acid treatment to form a vicinal hydroxyl group pair (≡Si-OH$\cdots$HO-Si≡). Upon thermal decomposition and ion exchange, the vicinal silanols are dehydrated to form an Si-O-Si linkage. The reverse can also happen, whereby the Si-O-Si linkage is hydrolyzed to form two vicinal silanol groups [84].

Geometry optimization calculations were performed on chabazite with a vicinal silanol defect near the acid site, as shown in Figure 3-9. In setting up the silanol defect model, an ≡Si-O-Si≡ linkage was replaced with an ≡Si-OH HO-Si≡ unit, essentially hydrolyzing an Si-O bond. The hydrolysis reaction is important because zeolites are commonly used as molecular sieves, so it is not unreasonable to assume that water molecules are present. There are several possible configurations for the silanol defect, but this one was chosen because the energy of formation was only 5.78 kJ/mol, making it likely to occur in a zeolite system. The heat of formation, which was calculated with the PW91 functional, is comparable to the value of 8 kJ/mol calculated using the B3-LYP functional [106], although Pascale et al. did not have an Al substituent in their chabazite unit cell. For comparison, the heat of formation for a hydrogarnet defect, where four hydrogen atoms bonded to four oxygen atoms substitute for a tetrahedral Si atom, is about 54 kJ/mol [106]. Pascale et al. also state that the BLYP functional tends to give Si-O and O-H bonds that are too long, which is why the PW91 functional was used in all of the calculations for this study.

The proton affinities and O-H vibrational frequencies at the acid site of chabazite with and without a silanol defect are shown in Table 3.9; the adsorption energies of methanol and ammonia at the acid site are shown in Table 3.10. It seems that the presence of the silanol defect results in slight decreases in both the methanol and

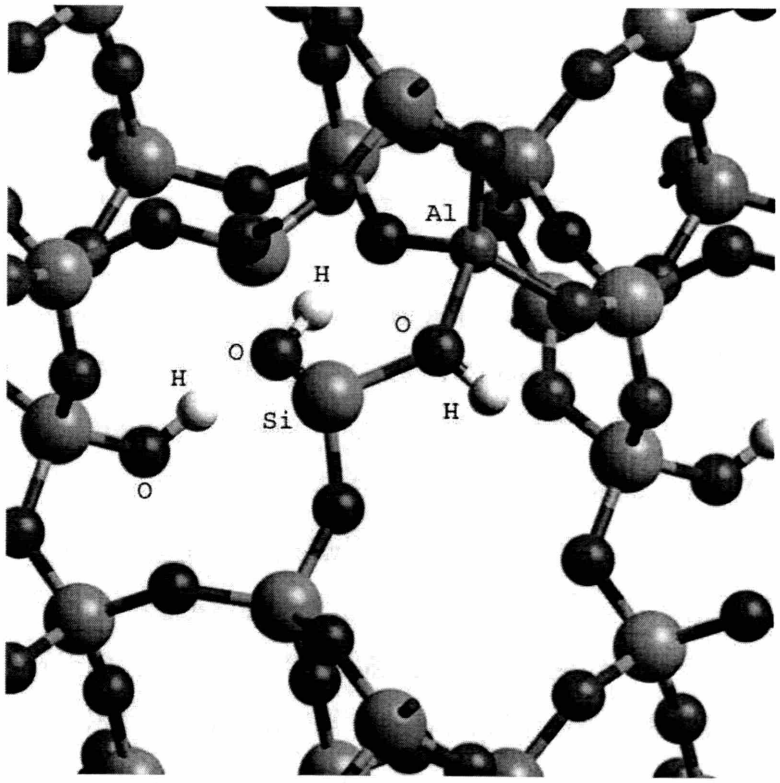

Figure 3-9: Chabazite with silanol framework defect near acid site

Table 3.9: Deprotonation energies and O-H vibrational frequencies at the acid site

CHA with	Deprotonation Energy (kJ/mol)	O-H Vibrational Frequency (cm^{-1})
Silanol Defect	1186.8	3522
No Defect	1180.9	3514

Table 3.10: Methanol and ammonia adsorption energies (kJ/mol) on chabazite (1 Al/unit cell) with and without silanol defect

	Base Adsorption Energy (kJ/mol)	
CHA with	Methanol	Ammonia
Silanol Defect	88.2	129.0
No Defect	91.7	144.5

ammonia adsorption energies. The chabazite O-H bond is not weakened much in the presence of the silanol defect; the O-H vibrational frequencies (3522 cm^{-1} with the silanol defect versus 3514 cm^{-1} with no defect) and bond lengths (0.980 Å in both cases) are roughly the same.

The ELF isosurfaces shed some light on what is happening at the acid site. In Figure 3-10, the ELF lobe at the acid site oxygen is smaller for chabazite with the silanol defect than for the defect-free chabazite. A possible explanation is that the substitution of H for Si at the silanol defect site results in a greater partial positive charge at the defect site. Some electron density is then shifted in the direction of the charge gradient, away from the acid site to the defect site. It can be concluded that the presence of a vicinal silanol framework defect does not affect appreciably the frequency of vibration of the O-H group, nor the heat of adsorption of small bases at the acid site.

3.3.6 Implications for Solid Acidity Scale

Based on these results, the four Brønsted sites corresponding to the Al substituent have roughly the same acid strength. It is difficult, given the results, to determine

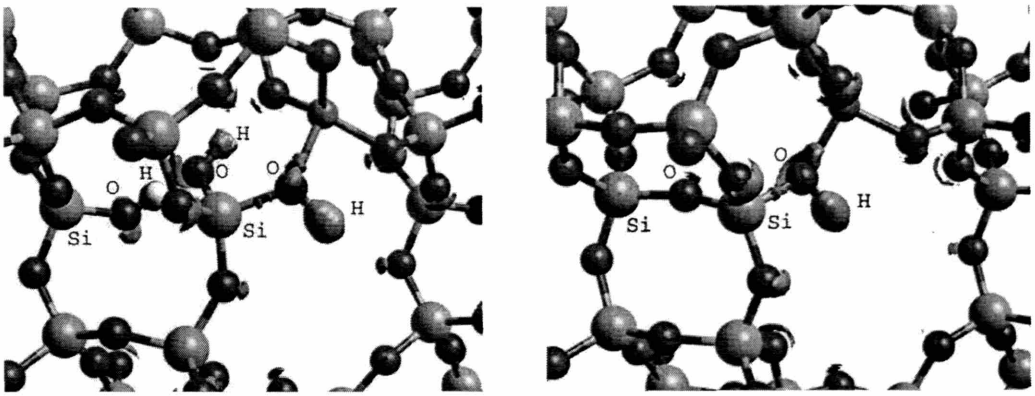

(a) (b)

Figure 3-10: ELF isosurfaces ($\chi = 0.87$) for Chabazite (a) with silanol defect, (b) without silanol defect

which of the characterization methods employed – base adsorption energies, acid site deprotonation energies, or structural parameters – is the best for characterizing acid site strength. However, the deprotonation energy is widely thought to be the best [124]. The results also suggest that small bases have similar adsorption energies on chabazite with 1 Al/unit cell, 2 Al/unit cell, and with a vicinal silanol framework defect. Therefore, neither the number of Al substituents in the zeolite unit cell nor the presence of structural defects near the acid site significantly affect the strength of the individual acid sites in chabazite.

It should be emphasized that the results do not imply that the O-H groups on different zeolites have the same strength, since the only zeolite considered in this study is chabazite. For example, Freude et al. [58] found that the enhanced catalytic activity of mordenite relative to zeolite Y is due to the higher acid strength of the O-H groups. They did note that the acidity should be constant for zeolites with Si/Al ratios greater than 10. Sharma et al. [123] found that the enthalpies of adsorption of ammonia and pyridine on mordenite are higher than the corresponding enthalpies on ZSM-5. Mosqueda-Jiménez et al. [98] found that both the strength of the acid sites in Ni-ZSM-5, Ni-MOR, and Ni-MCM-22, as measured by the shift of the O-H vibrational frequency upon adsorption of benzene, and the concentration of the acid

sites were directly correlated to the conversion of NO with propane.

It is also important to note that enhanced "activity" is not necessarily correlated to enhanced "acidity". For example, there is no proven correlation between enhanced catalytic activity and decreased proton affinity or changes in the equilibrium constant for proton donation to a base [57]. Several experimental studies seem to support this statement. Brunner et al. [24] showed that the magnitude of ^{1}H NMR chemical shifts and vibrational frequencies of bridging hydroxyl groups do not change upon hydrothermal treatment, even though enhanced activity of *n*-hexane cracking was observed. Biaglow et al. [11] found that the decomposition temperature of isopropylamine is the same on SAPO-5 and H-ZSM-5, and does not appear to be sensitive to the strength of the acid sites, since the strength of the sites in SAPO-5 is assumed to be intermediate between H-[Fe]-ZSM-5 and H-[Al]-ZSM-5 as measured by the materials' ability to protonate propene. Parillo and Gorte [105] showed that the rate of proton transfer is not correlated to the rate of alkane cracking since they occur at significantly different temperatures. Babitz et al. [3] performed solid-state NMR experiments showing that either the activation energy for hexane cracking is insensitive to differences in acid site strength, or there are no differences in acid strength among ZSM-5, mordenite, and Y zeolites.

Soscún et al. [135] recently defined a possible acidity scale in terms of a quantity described as the "intrinsic acidity" of the O-H groups. The intrinsic acidity is defined as the ratio between the O-H distance and the frequency of the O-H vibration mode. Soscún et al. showed that there exists a linear correlation between the intrinisic acidity and the total charge; however, all of the calculations were performed on cluster models of zeolites. The intrinsic acidity was calculated on the periodic models, as shown in Table 3.11. The intrinsic acidity was found to not correlate with the calculated adsorption energies, but the small differences in magnitude between the calculated intrinsic acidities (roughly 1.66%) shows that all four acid sites do have approximately the same acidity. Of course, the validity and usefulness of the intrinsic acidity factor needs to be further investigated.

Table 3.11: Intrinsic acidity [135] for the four acid sites in chabazite (1 Al/unit cell)

Acid Site	O-H Bond Length (Å)	O-H Vibrational Frequency (cm^{-1})	Intrinsic Acidity
O1	0.977	3578	2.73×10^{-12}
O2	0.979	3541	2.77×10^{-12}
O3	0.980	3514	2.79×10^{-12}
O4	0.980	3532	2.77×10^{-12}

3.4 Conclusions

Characterization via DFT and topological visualization of the acid sites in chabazite with varying framework defects, including multiple Al substituents in the 8T ring and a vicinal silanol defect near the acid site, was performed. It was confirmed, using both ELF visualization and constrained geometry optimizations, that there are two minima for proton positions on the oxygens at the acid site. The four acidic oxygens at the aluminum T-site all have roughly the same deprotonation energy, which is not strictly correlated to the O-H bond length or stretch vibrational frequency. Furthermore, the adsorption energy of various bases at each acid site oxygen is roughly the same and correlates well only with the gas-phase proton affinity of the base. These results reinforce the conclusion that the construction of a universal scale for quantifying zeolite acidity is likely to be problematic. Also, the deprotonation energies and base adsorption energies are not significantly changed with the presence of additional aluminum substituents in the zeolite framework, nor with silanol framework defects near the acid site.

Chapter 4

Methanol Coupling Reaction in Chabazite: Introduction and New Reaction Mechanism

4.1 Introduction

A reaction that has attracted considerable academic and industrial interest is the coupling reaction of two methanol molecules in a zeolite, to form higher chain hydrocarbons such as gasoline (MTG) or olefins (MTO) [150, 6, 126, 13, 15, 16, 20, 119, 137, 114, 139, 5, 42, 74, 117, 138, 131, 62, 132, 115, 116, 70]. The MTG process was developed in the late 1970's and commercialized in 1986 by Mobil [33, 32] as a response to the global energy crisis and a new interest in synfuels and other alternative gasoline sources. When the price of gasoline dropped, there was no longer a pressing need for the MTG process, however, methanol continued to be produced. Recently, interest has shifted to the MTO process, which was developed by Mobil and UOP/Norsk Hydro in 1996 [138]. Olefin and gasoline production can be coupled, since zeolites such as H-ZSM-5 and zeotypes such as SAPO-34 can oligomerize light olefins into a gasoline-like mixture of paraffins, higher olefins, aromatics, and naphthalenes.

It has been thought that the formation of the first C-C bond is the rate-limiting

step of these processes, but unfortunately, the reaction or reactions comprising this process have never been isolated experimentally, nor has a mechanism been definitely agreed upon. In fact, there have been over 20 proposed mechanisms for C-C bond formation [138]. Most of these are derived from the oxonium ylide (Figure 4-1(a)) or carbene (Figure 4-1(b)) mechanisms, both of which involve the formation of a CH_2: moiety which can then insert itself into hydrocarbon chains. The oxonium ylide mechanism requires the prior formation dimethyl ether, forms a trimethyloxonium ion intermediate, and results in the formation of ethylene. The carbene mechanism requires the prior formation of a surface methoxy group at the zeolite acid site.

Recently, indirect mechanisms (Figure 4-2(a)) have been proposed [70] that involve a pool of hydrocarbon species, including methylbenzenes and cyclic carbenium ions such as those in Figure 4-2(b). These hydrocarbons tend to form in the pores of zeolites by the reaction of impurities in the methanol feed, and serve to stabilize the intermediates and transition states of the C-C bond forming process. In particular, the dangling methyl groups on the hydrocarbons may be the organic reaction centers, not the surface methoxy groups that have been proposed. Haw et al. [132] have recently lent support to the hydrocarbon pool mechanism by contradicting the assumption that methanol or dimethyl ether can react by themselves to form olefins in the MTO process. They fed purified methanol and dimethyl ether reagents at 375 °C over a bed of H-ZSM-5 catalyst, and found that no olefin products were formed. Only in the presence of impure methanol were ethylene and propylene formed.

It has been thought, from four computational studies that address directly the formation of the first C-C bond, that the formation of surface methoxy groups and/or dimethyl ether are necessary first steps towards the formation of ethanol and higher hydrocarbons. Blaszkowski and van Santen [15] conclude that the first C-C bond is formed via reaction of a surface methoxy group with methanol or dimethyl ether and that pathways involving trimethyloxonium are not favorable. Tajima et al. [139] propose what they call the "methane-formaldehyde mechanism" in which a methanol reacts directly with a surface methoxy species to form methane and formaldehyde as stable intermediates. These then react to form ethanol, which is dehydrated to

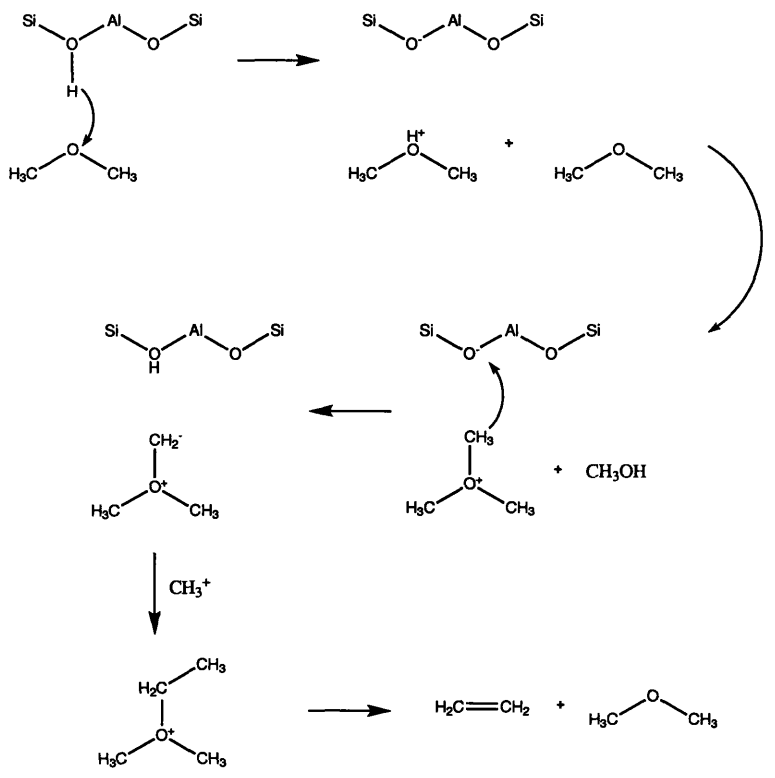

(a)

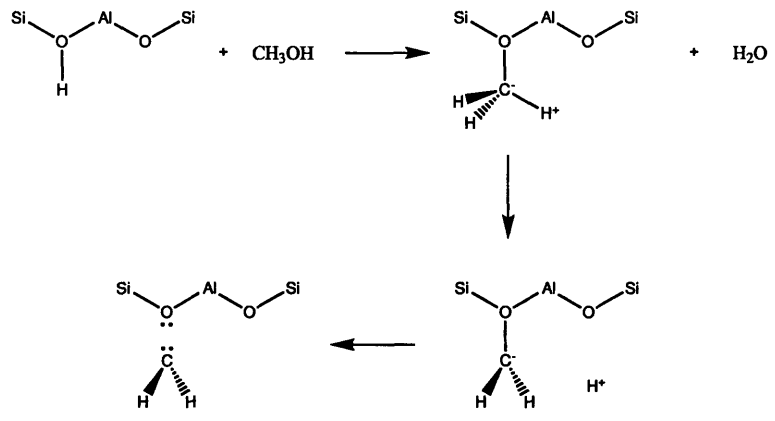

(b)

Figure 4-1: Proposed mechanisms for C-C bond forming in the methanol coupling reaction, requiring the formation of (a) Oxonium ylide [144, 103] and (b) Carbene [33, 86, 39]

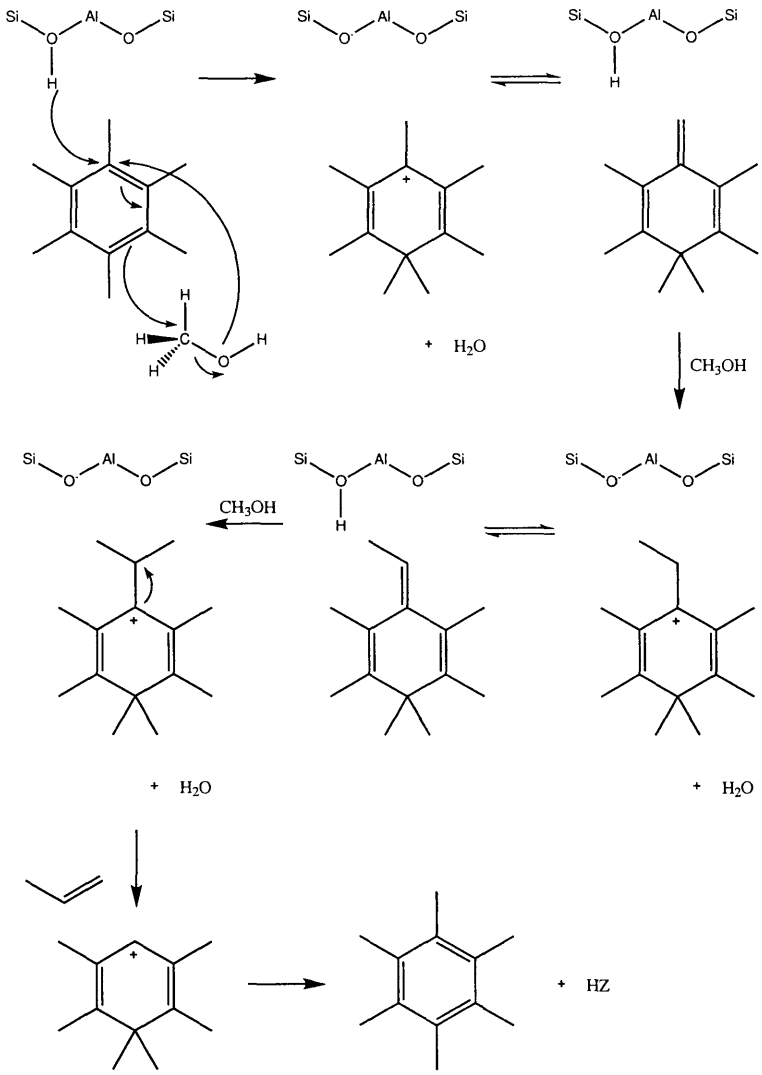

(a)

(b)

Figure 4-2: (a) Proposed mechanisms for C-C bond forming in the methanol coupling reaction through an initial methylbenzene catalyst [70], (b) Possible cations in the hydrocarbon pool [60, 149, 134, 133]

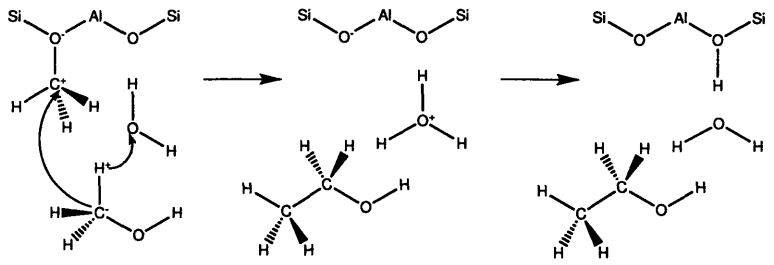

Figure 4-3: C-C bond forming mechanism of Blaszkowski and van Santen [15]

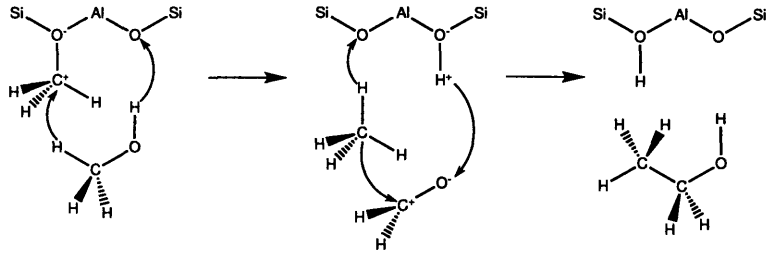

Figure 4-4: C-C bond forming mechanism of Tajima et al. [139]

ethylene. They found that their proposed pathway is more favorable than those incorporating oxonium ylide species, carbenes, or CO. Hutchings et al. [74] propose the interaction of a surface methoxy species with a second methanol molecule to form a surface ethoxy species, which after β-elimination forms ethylene. These three studies were all performed using small cluster models and static calculations. In the fourth study, Govind et al. [62] performed static calculations on a periodic model of two methanol molecules in ferrierite, and again proposed the reaction of a surface methoxy species with methanol or dimethyl ether to form ethanol or methyl-ethyl-ether; water does not play any visible role in their mechanism.

Despite the insight gained from these studies, they suffer from two major simplifications. First, the cluster calculations do not take into account the effects of the zeolite lattice, which include molecular shape selectivity, or short-range repulsions, and confinement effects, or long range attractions. Second, they do not take into account thermal effects caused by the dynamics of the motion of reactants and intermediates and entropic effects. In fact, the view of static transition-states as single saddle points can be only pictorial at best. In reality, the potential energy

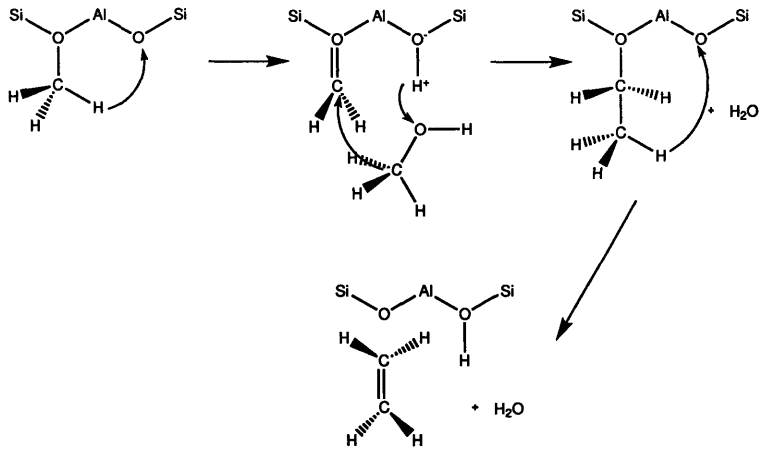

Figure 4-5: C-C bond forming mechanism of Hutchings et al. [74]

hypersurface would be quite rough, possessing many accessible saddle points.

Instead, the emphasis of this work was to find a dynamic mechanism for C-C bond formation from methanol reactants in the zeolite chabazite, without postulating *a priori* intermediates. Chabazite has been shown to be catalytically active for the coupling of methanol [150], and in these calculations, a model containing 1 Al substituent per unit cell was used.

4.2 Computational Methodology

Density functional theory [72, 83, 104], with the PW91 functional [110], was used to calculate electronic structure and energetics, and a plane-wave basis set code with periodic boundary conditions [75] was used to model the zeolite as an infinite crystalline system. The plane-wave cutoff chosen was 55 Ry. This is very close to plane-wave cutoffs used by other researchers [120, 122], and it has been found to be quite accurate, yielding the gas-phase proton affinity of methanol as 183.7 kcal/mol compared to 185.1 kcal/mol experimentally [2]. Only the Γ point was sampled in the Brillouin zone. The fictitious electronic mass used was 1100 a.u., and timesteps of 7.0 a.u. (0.17 fs) were used for all runs.

The molecular dynamics simulations of two methanol molecules in the chabazite

unit cell were performed using the Car-Parrinello [26, 75] approach. This method combines a quantum mechanical treatment of the electrons via density functional theory and a classical treatment of the nuclei, which are moved via a molecular dynamics simulation. All simulations were performed at 400 °C, the industrial operating temperature for the MTO and MTG processes [80]. The actual loading is 5-6 methanol molecules per active site in the MTG process [97], but only two molecules per active site were considered to simplify the interactions.

To simulate the C-C bond formation process, initially the C-C interatomic distance was chosen as the reaction coordinate, and a series of non-zero temperature simulations were performed to sample across that reaction coordinate. This reaction coordinate was also chosen by Sauer et al. [118] in their study of the methanol coupling reaction. First, geometry optimizations were performed at 0 K of the two methanol molecules in chabazite, and next, from the optimized structure, the C-C distance was decreased and its value constrained. Initially, this decrease in distance occurred at 0.4 Å intervals, and closer to the transition state, it occurred at 0.2 Å intervals. At each point along the reaction coordinate, the ensemble averaged force due to the constraint was evaluated along the constrained direction. From these simulations, the free energy was computed as a function of the reaction coordinate by integrating the average force along the reaction coordinate [27, 136, 108, 44].

In order to determine properties averaged within the canonical ensemble, a Nosé-Hoover chain thermostat with a length of 4 and a characteristic frequency of 1500 cm^{-1} was used on the nuclear degrees of freedom [102, 73, 89]. Each constrained molecular dynamics simulation run lasted 1.5 ps. During the first 0.5 picoseconds, the system was equilibrated and during the next picosecond, accumulated data was averaged to determine properties of interest. One picosecond of averaging was found to be enough to calculate the properties reported in this paper with small statistical uncertainties. Because the initial equilibration period was discarded, all references to time along the trajectory are made starting after this equilibration period.

4.3 Results and Discussion

The overall reaction in the zeolite that was mapped is:

$$2CH_3OH \rightarrow CH_3CH_2OH + H_2O \tag{4.1}$$

4.3.1 Preliminary Reaction Mechanism Obtained Via Constrained Molecular Dynamics

As mentioned in Section 2.2.1, the free energy was computed as a function of the reaction coordinate using Equation 4.2 [136]:

$$\frac{dF}{d\xi} = -\langle\lambda\rangle_\xi \tag{4.2}$$

where F is the free energy, ξ is the value of the constraint, which in this case is the value of the C-C distance, and λ is the Lagrange multiplier due to the constraint, which is equal to the negative of the force along the constrained C-C direction. Because the constraint used in this study is a simple distance constraint, the expression can be simplified greatly to the term on the right hand side of Equation 4.2 [27]. Thus, the ensemble-averaged force on the constraint can be used to determine the free energy as a function of the reaction coordinate by integrating the average force along the reaction coordinate.

The free energy versus C-C distance was plotted in Figure 4-6. The free energy of the unconstrained system, where C-C = 5.14 Å, was set to be zero. Figure 4-6 shows that the free energy change needed for the C-C distance to decrease from 5.14 Å to 3.8 Å is only 3.1 kJ/mol, which would be rapidly and easily attained at 400 °C. C-C = 1.8 Å is already past the peak of the free energy curve at 1.94 Å, so the free energy barrier for the system to move across the constraint is calculated to be $\Delta F^{TS} = 223.5$ kJ/mol.

To separate the energetic from the entropic terms in the free energy, an equilibrated frame of the C-C = 2.0 Å trajectory was selected, the bond length was reduced

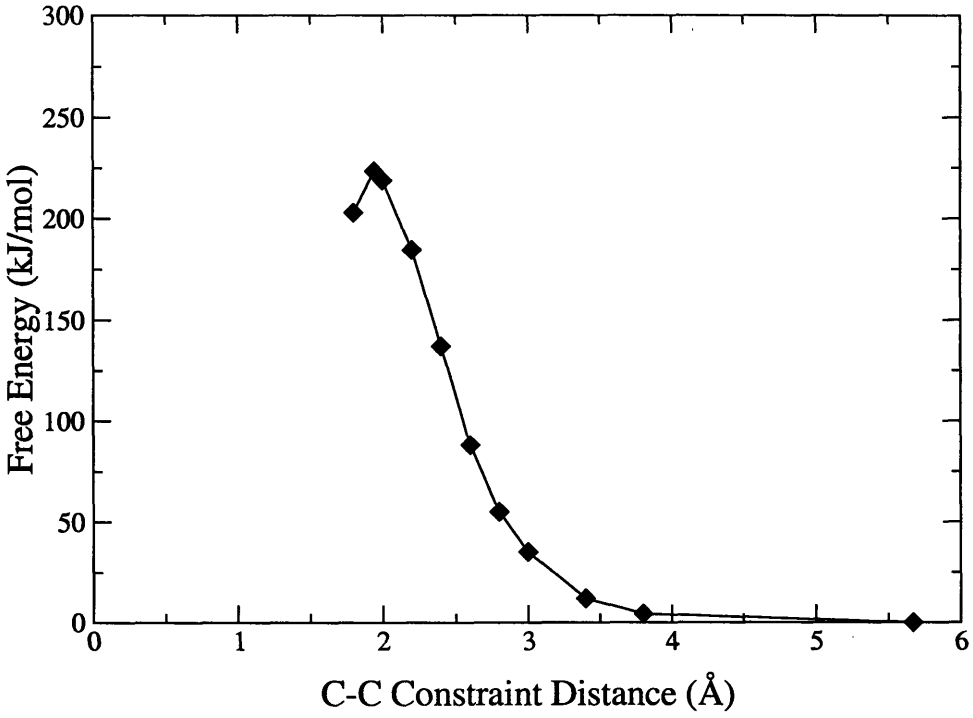

Figure 4-6: Free energy barrier for the methanol-methanol coupling reaction in the constrained ensemble (T = 673 K)

to 1.94 Å, and a geometry optimization was performed. For Reaction 4.1, this yields $\Delta U^{TS}(0K)$ = 173.8 kJ/mol, and $\Delta S^{TS}(673K)$ = -0.0738 kJ/mol·K. The calculated $\Delta U^{TS}(0K)$ for this study is 10.0 kJ/mol lower than that calculated by Tajima et al. [139] and 77.2 kJ/mol lower than that calculated by Blaszkowski and van Santen [15]. The energetic term is also lower than the value obtained with mass spectrometry experiments on the most similar C-C bond forming reaction found in the literature, where 212.26 kJ/mol of thermal energy was needed for the gas-phase reaction [129]:

$$[CH_3OHCH_3]^+ \rightarrow C_2H_5^+ + H_2O \tag{4.3}$$

There exist only limited experimental values for free energy barriers and reaction rate constants for the C-C bond forming process. Chen and Reagan [34] developed a kinetic model for olefin formation in ZSM-5:

$$
\begin{aligned}
A &\xrightarrow{k_1} B \\
A + B &\xrightarrow{k_2} B \\
\frac{dA}{dt} &= -k_1 A - k_2 AB
\end{aligned}
\tag{4.4}
$$

where A represents the oxygenates and B represents the olefins in the system. Using an autocatalytic assumption:

$$
\begin{aligned}
A_0 - A = B - B_0 &\Rightarrow A_0 - A \approx B \\
1 - \frac{A_0}{A} &= 1 - \frac{1 + \frac{A_0}{R}}{\frac{A_0}{R} + exp\left(k_2 \left(1 + R\right) t\right)}
\end{aligned}
\tag{4.5}
$$

where $R = \frac{k_1}{k_2}$, they determined that k_2 ranged in value between 0.1 and 1.1 s^{-1}. These experiments were performed at $T = 370$ °C, so their free energy barrier can be calculated using transition state theory:

$$
\begin{aligned}
\nu &= \frac{kT}{h} = 1.34 \times 10^{13} s^{-1} \\
K^{\ddagger} &= \frac{k_2}{\nu} = \text{between } 7.46 \times 10^{-15} \text{ and } 8.21 \times 10^{-14} \\
\Delta F^{ts} &= -kTlnK^{\ddagger} = \text{between 161 and 174 kJ/mol}
\end{aligned}
\tag{4.6}
$$

where ν is the prefactor to the rate constant k_2, and $K^{\ddagger}$ is the equilibrium constant of the reaction. While this experimental range of ΔF^{ts} is lower than the free energy barrier of 223.5 kJ/mol calculated in this study, it is important to note that ZSM-5 is known to be more active than chabazite for the MTO reaction [150], there may be a difference in reaction rates for olefin versus alcohol formation, and the kinetic model is highly simplified. Furthermore, the calculated value of 223.5 kJ/mol should be taken as an upper bound, considering, as shown below, that the simple distance constraint does not characterize the reaction process fully.

No significant chemical events occur until the C-C distance is 2.2 Å . In this

trajectory (snapshots in Figure 4-7), first a proton is transferred from the zeolite acid site to one of the methanol molecules, forming a methoxonium cation, which subsequently splits into a methyl cation and water, breaking the C-O bond. Then the remaining methanol transfers one of its protons to the methyl cation, forming methane and "protonated formaldehyde" (CH_2OH^+). These three intermediates are stable for at least 2.0 ps. When the C-C distance is 1.8 Å , the water extracts a proton from methane, as seen by the snapshots in Figure 4-8. Then, a concerted simultaneous transfer of a proton from H_3O^+ to protonated formaldehyde occurs, just as the latter transfers a proton back to the chabazite acid site, and the final formation of an ethanol-like species. When the C-C constraint is released, the C-C bond is formed and ethanol is formed.

From the results of the constrained molecular dynamics simulations, it can be concluded that the process, which produces ethanol and water, involves stable intermediates of methane, protonated formaldehyde, and water, which would imply a two step reaction. However, from Figure 4-6, it seems that there is only one transition state in the overall reaction. Therefore, it was necessary to determine whether the transition state region is indeed being sampled or not.

The committor distribution corresponding to the C-C = 2.2 Å trajectory (Figure 4-9(a)) was bimodal (Figure 2-2(b)). The committor distribution corresponding to the C-C = 1.8 Å trajectory (Figure 4-9(b)) was skewed in the $P_B = 1$ direction (Figure 2-4(b)), indicating that the transition state region had not been properly captured. Therefore, the C-C distance is an inadequate reaction coordinate, and while these constrained molecular dynamics trajectories do suggest intermediates and products of the methanol coupling reaction, they do not represent a reaction mechanism.

Although the constrained molecular dynamics trajectories with the C-C distance constraint were unphysical, they did give insight into the reaction process, initial dynamic trajectories, likely reactants and products, and an upper bound on the free energy barrier of reaction.

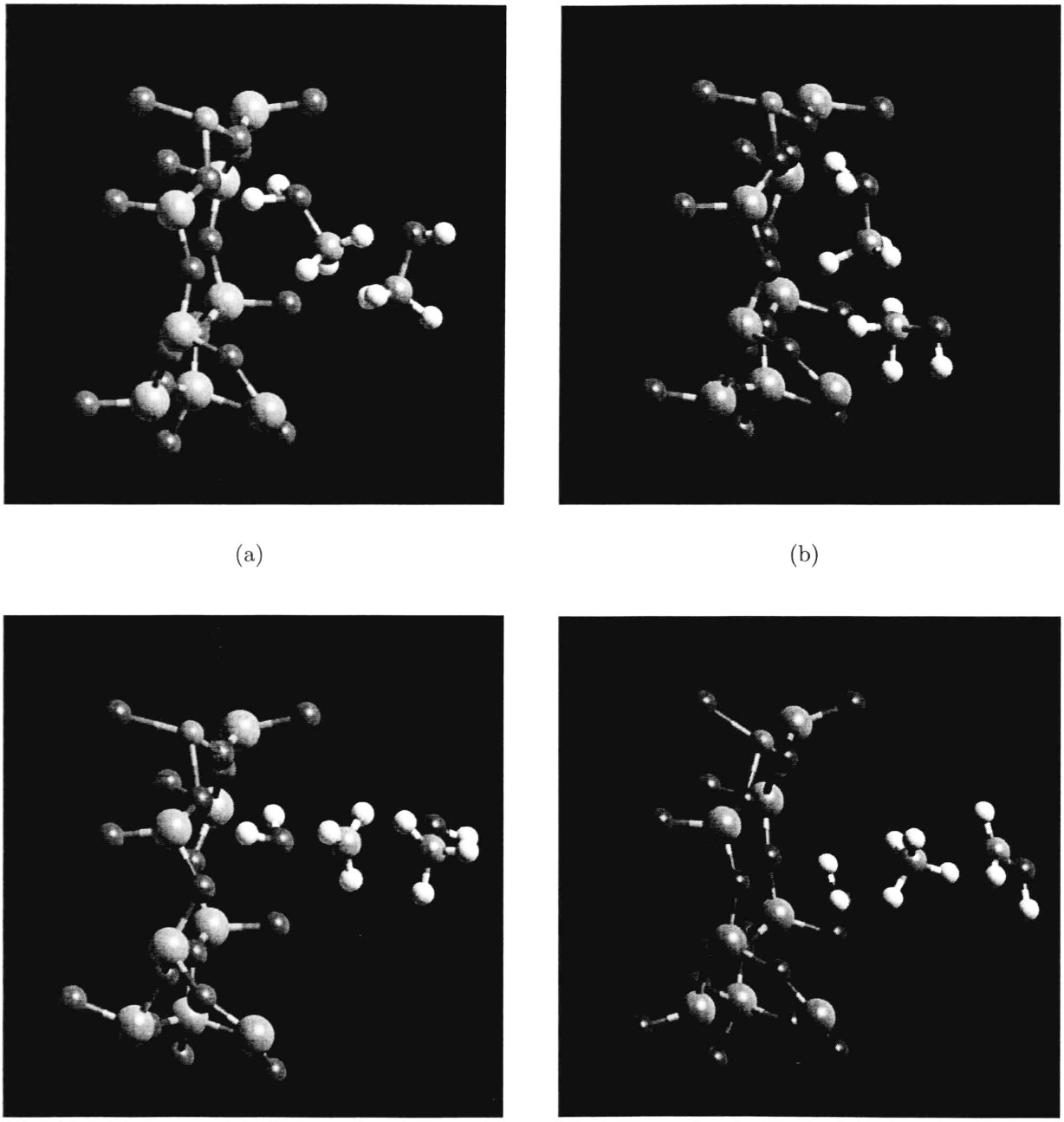

(a) (b)

(c) (d)

Figure 4-7: Snapshots from the C-C = 2.2 Å constrained dynamics trajectory, showing: (a) the initial physisorbed system, (b) the protonation of methanol, (c) the breaking of a C-O bond to form water and methyl cation, and (d) the extraction of a proton from the second methanol to form methane and protonated formaldehyde

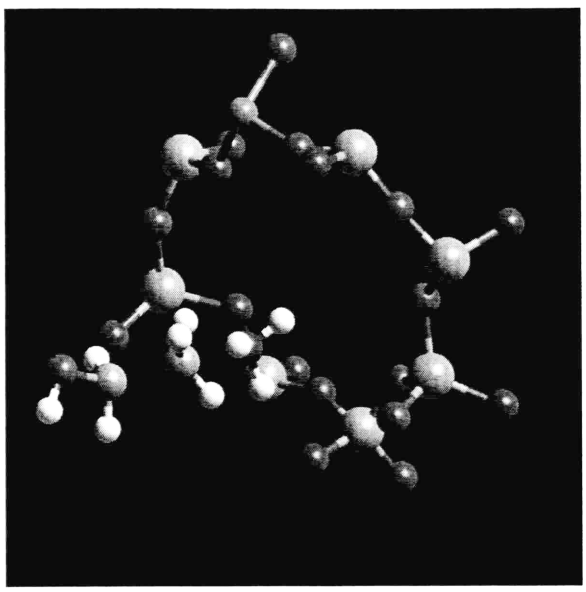

(a)

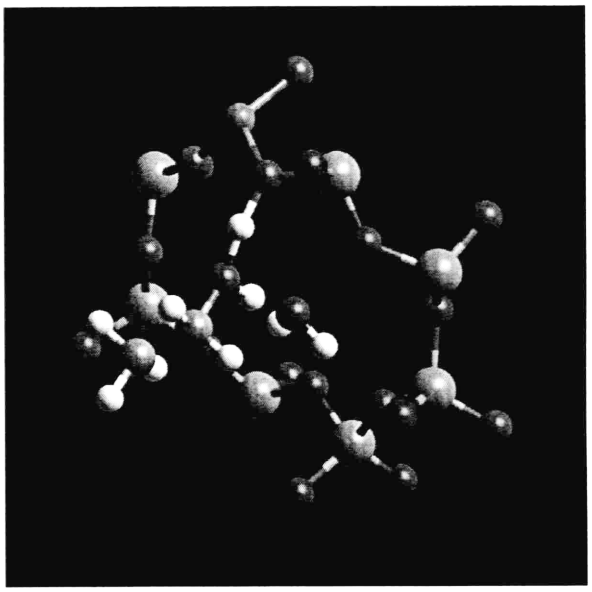

(b)

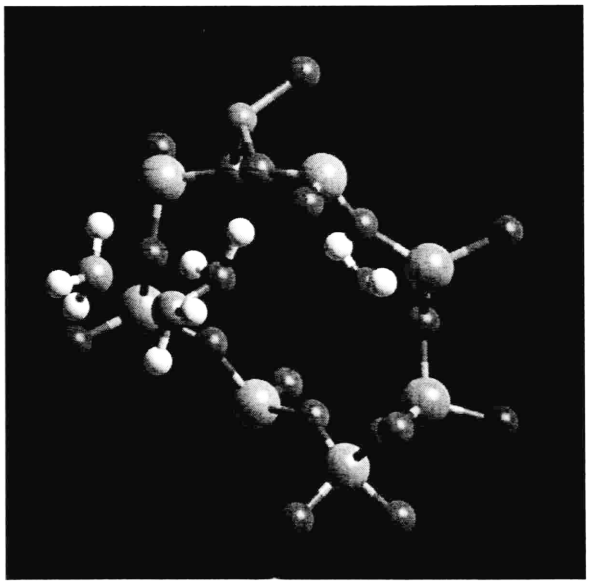

(c)

Figure 4-8: Snapshots from the C-C = 1.8 Å constrained dynamics trajectory, showing: (a) the stable intermediates, (b) the concerted transfer of a proton from water to protonated formaldehyde to the zeolite, and (c) the final ethanol-like product

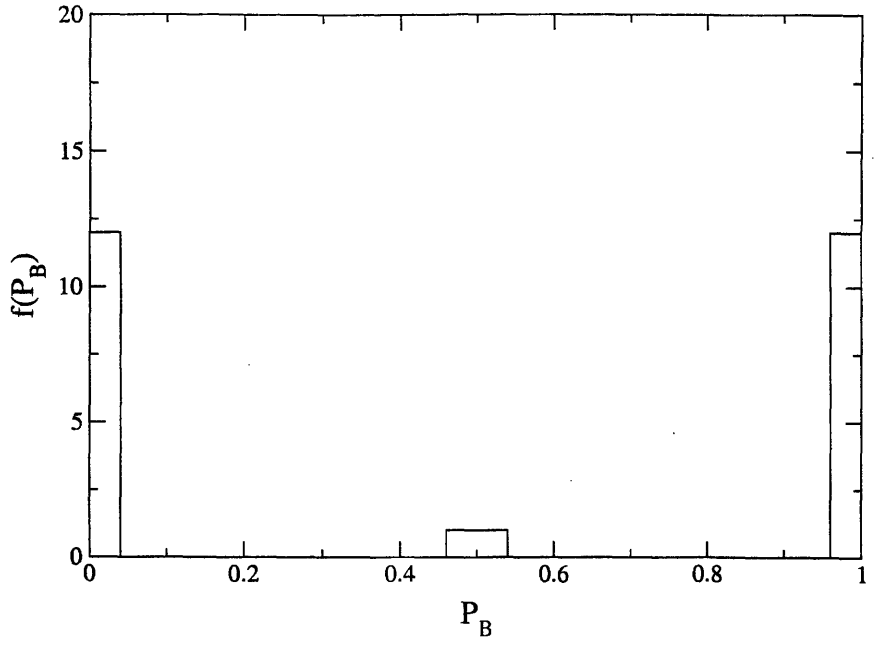

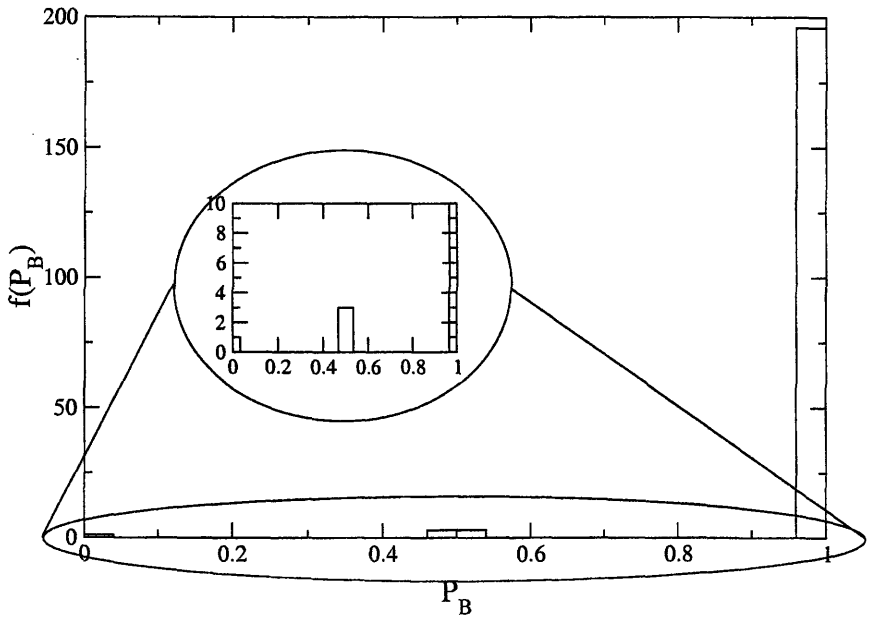

(b)

Figure 4-9: Committor probability distributions for the (a) C-C = 2.2 Å and (b) C-C = 1.8 Å constrained trajectories

4.3.2 Dynamic Mechanism Obtained Via Transition Path Sampling

A mechanism for ethanol and water formation from two methanol molecules was then obtained via transition path sampling calculations. Two hundred iterations of the shooting algorithm were performed, and this was found to be sufficient for converging path-averaged quantities. All shooting paths were 0.06 ps in length ($\mathcal{T}$). The simulations were run in the microcanonical ensemble, with an initial temperature of 400 °C. Two reaction steps were found: the breaking of the C-O bond to form H_2O, CH_4, and CH_2OH^+, and the forming of the C-C bond to form CH_3CH_2OH.

For the C-O bond breaking step, the shooting algorithm converged towards a mechanism (Figures 4-10) that was very similar to the pathway obtained using constrained molecular dynamics with the C-C distance fixed at 2.2 Å. First, one of the methanol molecules is chemisorbed to the zeolite acid site; chemisorption, involving proton transfer from the acidic oxygen to the base, is observed only when there is more than one methanol molecule per acid site, otherwise only physisorption is observed. Next, the C-O bond of the methoxonium cation slowly stretches until it breaks, leaving water and methyl cation. The main difference was the configuration of the intermediate step, whereby a proton is transferred from the second methanol molecule's CH_3 moiety to the methyl cation. The transition state structure $[H_2O \cdots CH_3 \cdots H \cdots CH_2OH]^+$ is almost linear, suggesting that there is some orbital overlap facilitating the proton transfer. The intermediates H_2O, CH_4, and CH_2OH^+ are stable for at least 2.0 ps.

For the C-C bond forming step, the shooting algorithm converged towards a mechanism (Figures 4-11) that was significantly different from the pathway obtained using constrained molecular dynamics with the C-C distance fixed at 1.8 Å. In the dynamic mechanism, the proton transfer from methane to water occurs concurrently with the formation of the C-C bond. The transition state structure is thus $[H_2O \cdots H \cdots CH_3 \cdots CH_2OH]^+$. After some time, H_3O^+ transfers a proton back to a zeolite acid site, but different from the original one. In that way, the catalyst is unchanged at the

end of the reaction.

The overall reaction diagram for the methanol coupling process is depicted in Figure 4-12.

4.4 Conclusions

The application of transition path sampling and constrained molecular dynamics methods to a problem in solid state catalysis has been demonstrated. In particular, a new mechanism was found for the C-C bond formation in the methanol coupling reaction that does not involve the formation of dimethyl ether or surface methoxy groups at the acid site. This mechanism at 400 °C proceeds through stable intermediates of water, methane, and protonated formaldehyde to form ethanol. The C-C bond forms directly and concurrently with a proton transfer from methane to water.

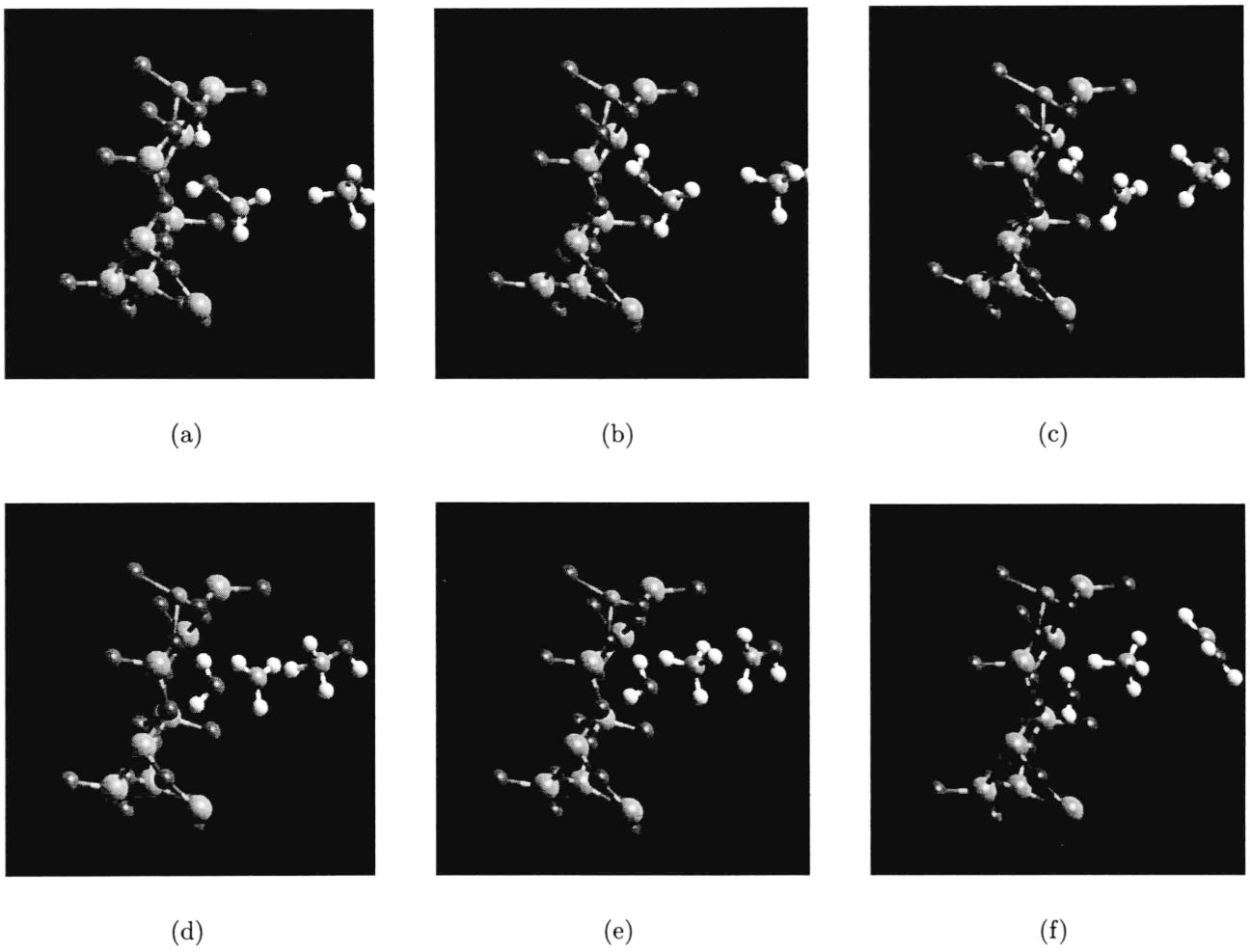

Figure 4-10: Mechanism for first step in the methanol coupling reaction. (a) Initial physisorption of methanol molecules, (b) Chemisorption of methanol, with complete proton transfer from zeolite acid site to methanol, (c) Breaking of C-O bond in the methoxonium cation, leaving water and methyl cation, (d) Linear transition state $[H_2O \cdots CH_3 \cdots H \cdots CH_2OH]^+$, (e) Final proton transfer from methanol to methyl cation, (f) Stable intermediate species H_2O, CH_4, and CH_2OH^+

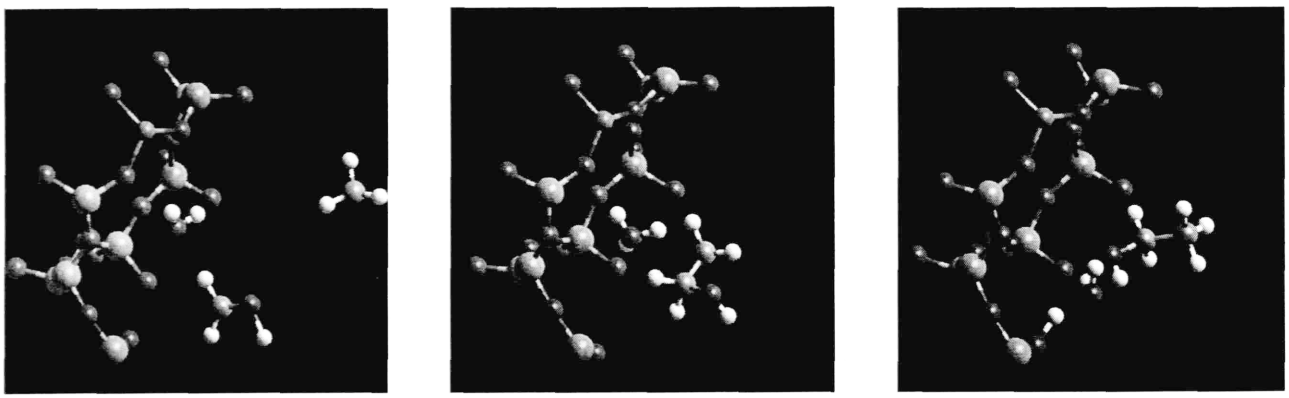

(a) (b) (c)

Figure 4-11: Mechanism for second step in the methanol coupling reaction. (a) Intermediate species H_2O, CH_4, and CH_2OH^+, (b) Simultaneous proton transfer from CH_4 to H_2O and formation of C-C bond, resulting in ethanol (c) Final proton transfer from H_2O back to the zeolite acid site of the adjacent unit cell, leaving the catalyst unchanged

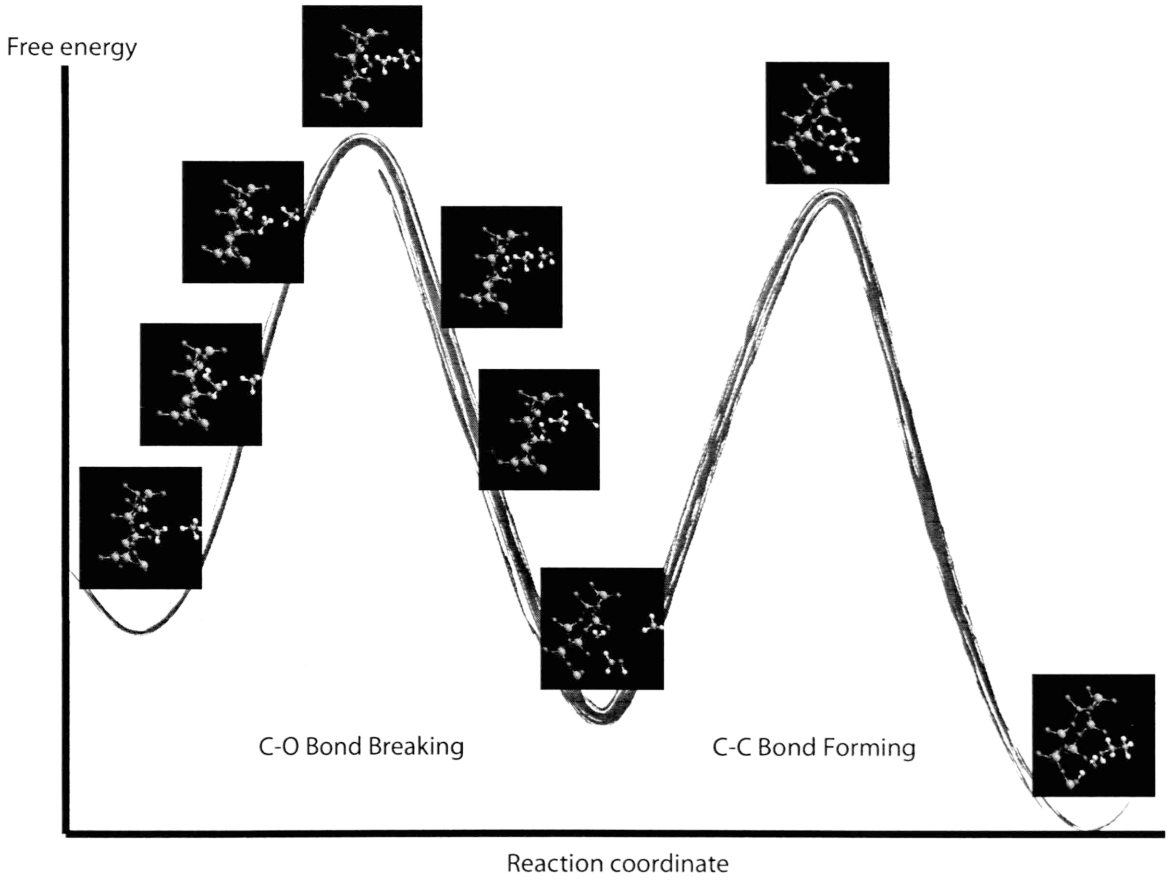

Figure 4-12: Overall reaction diagram for the methanol coupling process in chabazite, referencing Figures 4-10 and 4-11

Chapter 5

Methanol Coupling Reaction in Chabazite: Analysis of Free Energy Barriers and the Role of the Zeolite in Catalysis

5.1 Introduction

In Chapter 4, a new mechanism was computed for C-C bond formation in the methanol coupling reaction in chabazite. One of the goals mentioned in Chapter 1 is to gain some understanding of the role of zeolites in catalytic reactions. One way of doing this is to compute the mechanism and free energy barrier(s) for the methanol coupling reaction in the gas phase, and compare these to the mechanism and free energy barrier(s) of the analogous reactions in chabazite.

The free energy barrier was calculated to be 223.5 kJ/mol in Section 4.3.1. However, this barrier is incorrect since it was computed by sampling across the wrong reaction coordinate (C-C constraint). Therefore, new reaction coordinates need to be identified and free energy barriers computed for both steps of the methanol coupling reaction. The committor probability distributions shown in Figures 4-9(a) and 4-9(b)

indicate that multiple reaction coordinates are needed to describe these chemical processes.

For the C-O Bond Breaking step, one possible reaction coordinate is the C_1-O distance of the protonated methanol, which contains C_1. Another possible reaction coordinate is the [(C_1-H*) - (C_2-H*)] asymmetric stretch, which is a difference of C-H distances. H* denotes the proton that is transferred from the unprotonated methanol (containing C_2) to the methyl cation (containing C_1) once the C-O bond of the protonated methanol has been broken.

For the C-C Bond Forming step, the C_1-C_2 distance is still a valid reaction coordinate. Another possible reaction coordinate is the [(O-H*) - (C_1-H*)] asymmetric stretch, where H* denotes the proton that is transferred from methane (containing C_1) to water.

5.2 Computational Methodology

As previously stated in Equation 2.48, the contribution of each constrained reaction coordinate to the free energy is given as:

$$\frac{\partial F}{\partial \xi_i} = \frac{\langle |Z_\xi|^{-1/2} \left(-\lambda + \frac{kT}{2} \sigma_j \left[Z_\xi \right]_{ij} \left(\nabla' \xi_j \cdot Tr \left(Z_\xi^{-1} \nabla' Z_\xi \right) \right) \right) \rangle_\xi}{\langle |Z_\xi|^{-1/2} \rangle_\xi} \tag{5.1}$$

For C-O bond breaking, the two constraints and their partial derivatives can be written as:

$$
\begin{aligned}
\xi_1 &= \|x_{C_1} - x_O\| = \sqrt{(x_{C_1} - x_O) \cdot (x_{C_1} - x_O)} \\
\frac{\partial \xi_1}{\partial x_{C_1}} &= \frac{2\,(x_{C_1} - x_O)}{2\sqrt{(x_{C_1} - x_O) \cdot (x_{C_1} - x_O)}} \\
\frac{\partial \xi_1}{\partial x_O} &= \frac{-2\,(x_{C_1} - x_O)}{2\sqrt{(x_{C_1} - x_O) \cdot (x_{C_1} - x_O)}} \\
\xi_2 &= \|x_{C_1} - x_H\| - \|x_{C_2} - x_H\| \\
\frac{\partial \xi_2}{\partial x_{C_1}} &= \frac{2\,(x_{C_1} - x_H)}{2\sqrt{(x_{C_1} - x_H) \cdot (x_{C_1} - x_H)}} \\
\frac{\partial \xi_2}{\partial x_{C_2}} &= \frac{-2\,(x_{C_2} - x_H)}{2\sqrt{(x_{C_2} - x_H) \cdot (x_{C_2} - x_H)}} \\
\frac{\partial \xi_2}{\partial x_H} &= \frac{-2\,(x_{C_1} - x_H)}{2\sqrt{(x_{C_1} - x_H) \cdot (x_{C_1} - x_H)}} + \frac{2\,(x_{C_2} - x_H)}{2\sqrt{(x_{C_2} - x_H) \cdot (x_{C_2} - x_H)}}
\end{aligned}
\tag{5.2}
$$

Therefore, the matrix Z_ξ is:

$$
\begin{bmatrix}
\frac{1}{m_{C_1}} + \frac{1}{m_O} & \frac{1}{m_{C_1}} \frac{(x_{C_1} - x_O) \cdot (x_{C_1} - x_H)}{\|x_{C_1} - x_O\| \cdot \|x_{C_1} - x_H\|} \\
\frac{1}{m_{C_1}} \frac{(x_{C_1} - x_O) \cdot (x_{C_1} - x_H)}{\|x_{C_1} - x_O\| \cdot \|x_{C_1} - x_H\|} & \frac{1}{m_{C_1}} + \frac{1}{m_{C_2}} + \frac{2}{m_H} \left[1 - \frac{(x_{C_1} - x_H) \cdot (x_{C_2} - x_H)}{\|x_{C_1} - x_H\| \cdot \|x_{C_2} - x_H\|} \right]
\end{bmatrix}
\tag{5.3}
$$

and its determinant is:

$$
|Z_\xi| = \left(\frac{1}{m_{C_1}} + \frac{1}{m_O} \right) \left(\frac{1}{m_{C_1}} + \frac{1}{m_{C_2}} + \frac{2}{m_H} \left[1 - \frac{(x_{C_1} - x_H) \cdot (x_{C_2} - x_H)}{\|x_{C_1} - x_H\| \cdot \|x_{C_2} - x_H\|} \right] \right) - \frac{1}{m_{C_1}} \frac{1}{m_{C_1}}
\tag{5.4}
$$

We can expand the term:

$$
\nabla' \xi_j \cdot Tr \left(Z_\xi^{-1} \nabla' Z_\xi \right) = \sigma_{klm} \frac{1}{m_k} \frac{\partial \xi_j}{\partial x_k} \left[Z_\xi^{-1} \right]_{lm} \frac{\partial \left[Z_\xi \right]_{lm}}{\partial x_k}
\tag{5.5}
$$

To compute this term, we can follow a multistep approach, with $d(i,j) = \frac{\partial \xi_i}{\partial x_j}$ and $d_2(i,j,k) = \frac{\partial^2 \xi_i}{\partial x_j \partial x_k}$:

$$v_1(j,l,r) = \sum_{k=1}^{N} \frac{1}{m_k} d(j,k) d_2(l,r,k) \tag{5.6}$$

$$v_2(j,l,m) = \sum_{r=1}^{N} \frac{1}{m_r} \left[v_1(j,l,r) d(m,r) + v_1(j,m,r) d(l,r) \right] \tag{5.7}$$

$$v_3(j) = \sum_{lm} \left[Z_\xi^{-1} \right]_{lm} v_2(j,l,m) = \nabla' \xi_j \cdot Tr \left(Z_\xi^{-1} \nabla' Z_\xi \right) \tag{5.8}$$

However, we note that all the second derivatives $d_2(i,j,k)$ are zero, so the term in Equation 5.5 becomes zero. Thus, for both reaction coordinates describing the C-O bond breaking step, the relation between free energy and constraint forces collapses to:

$$\frac{\partial F}{\partial \xi_i} = \frac{\langle |Z_\xi|^{-1/2} (-\lambda) \rangle_\xi}{\langle |Z_\xi|^{-1/2} \rangle_\xi} \tag{5.9}$$

which was previously stated as Equation 2.49.

Equation 5.9 can be used for the two reaction coordinates describing the C-C bond breaking step. The reaction coordinates are:

$$\xi_1 = \|x_{C_1} - x_{C_2}\| = \sqrt{(x_{C_1} - x_{C_2}) \cdot (x_{C_1} - x_{C_2})} \tag{5.10}$$

$$\frac{\partial \xi_1}{\partial x_{C_1}} = \frac{2 (x_{C_1} - x_{C_2})}{2\sqrt{(x_{C_1} - x_{C_2}) \cdot (x_{C_1} - x_{C_2})}} \tag{5.11}$$

$$\frac{\partial \xi_1}{\partial x_{C_2}} = \frac{-2 (x_{C_1} - x_{C_2})}{2\sqrt{(x_{C_1} - x_{C_2}) \cdot (x_{C_1} - x_{C_2})}} \tag{5.12}$$

$$\xi_2 = \|x_O - x_H\| - \|x_{C_1} - x_H\| \tag{5.13}$$

$$\frac{\partial \xi_2}{\partial x_O} = \frac{2 (x_O - x_H)}{2\sqrt{(x_O - x_H) \cdot (x_O - x_H)}} \tag{5.14}$$

$$\frac{\partial \xi_2}{\partial x_{C_1}} = \frac{-2 (x_{C_1} - x_H)}{2\sqrt{(x_{C_1} - x_H) \cdot (x_{C_1} - x_H)}} \tag{5.15}$$

$$\frac{\partial \xi_2}{\partial x_H} = \frac{-2 (x_O - x_H)}{2\sqrt{(x_O - x_H) \cdot (x_O - x_H)}} + \frac{2 (x_{C_1} - x_H)}{2\sqrt{(x_{C_1} - x_H) \cdot (x_{C_1} - x_H)}} \tag{5.16}$$

and the determinant of the matrix Z_ξ is:

$$|Z_\xi| = \left(\frac{1}{m_{C_1}} + \frac{1}{m_{C_2}}\right)\left(\frac{1}{m_O} + \frac{1}{m_{C_1}} + \frac{2}{m_H}\left[1 - \frac{(x_O - x_H)\cdot(x_{C_1} - x_H)}{\|x_O - x_H\| \cdot \|x_{C_1} - x_H\|}\right]\right) - \frac{1}{m_{C_1}}\frac{1}{m_{C_1}} \tag{5.17}$$

Molecular dynamics simulations on the system are run with both reaction coordinates simultaneously constrained at various values. The λ due to each constraint is calculated at each grid point (ξ_1,ξ_2). Two-dimensional integration can then be used to calculate the change in free energy from Equation 5.9.

A first order Taylor expansion is given by:

$$F(x + \Delta x, y + \Delta y) = F(x, y) + F_x(x, y)\,\Delta x + F_y(x, y)\,\Delta y + \ldots \tag{5.18}$$

where F_x and F_y represent the partial derivatives of F with respect to x and y, respectively.

Alternatively, a two-dimensional trapezoidal integration can be used [49]. First, the integration is performed in one of the directions, x in Equation 5.19 and y in Equation 5.20:

$$F(x + \Delta x, y) = F(x, y) + \frac{1}{2}\left[F_x(x + \Delta x, y) + F_x(x, y)\right]\Delta x \tag{5.19}$$

$$F(x, y + \Delta y) = F(x, y) + \frac{1}{2}\left[F_y(x, y + \Delta y) + F_y(x, y)\right]\Delta y \tag{5.20}$$

Next, the integration is performed in the other direction:

$$F(x + \Delta x, y + \Delta y) = F(x, y + \Delta y) + \frac{1}{2}\left[F_x(x + \Delta x, y + \Delta y) + F_x(x, y + \Delta y)\right]\Delta x \tag{5.21}$$

$$F(x + \Delta x, y + \Delta y) = F(x + \Delta x, y) + \frac{1}{2}\left[F_y(x + \Delta x, y + \Delta y) + F_y(x + \Delta x, y)\right]\Delta y \tag{5.22}$$

Equations 5.21 and 5.22 can be summed and divided by 2 to get the final expres-

sion:

$$\begin{aligned} f(x+\Delta x, y+\Delta y) &= f(x,y) \\ &+ \frac{1}{4}\left[f_x(x+\Delta x, y+\Delta y) + f_x(x+\Delta x, y) + f_x(x, y+\Delta y) + f_x(x,y)\right]\Delta x \\ &+ \frac{1}{4}\left[f_y(x+\Delta x, y+\Delta y) + f_y(x+\Delta x, y) + f_y(x, y+\Delta y) + f_y(x,y)\right]\Delta y \end{aligned}$$

Equation 5.18 is a good approximation to Equation 5.23 only if the grid points (ξ_1,ξ_2) are finely spaced.

5.3 Results and Discussion

The free energy barriers for the C-O bond breaking and C-C bond forming steps, in both chabazite and the gas phase, are now presented and compared.

5.3.1 C-O Bond Breaking Step

For the C-O bond breaking step in chabazite, the two reaction coordinates were simultaneously constrained in a pairwise fashion at the following values:

- C_1-O distance (ξ_1): 1.361 (unconstrained), 1.4, 1.6, 1.8, 2.0, 2.15, 2.25, 2.35, 2.45, 2.55, 2.7, 2.9 Å
- [(C_1-H*) - (C_2-H*)] asymmetric stretch (ξ_2): 4.3 (unconstrained) 4.2, 4.0, 2.5, 1.0, 0.0, -0.6, -1.2, -1.8, -2.4 Å

The λ's due to each constraint are plotted, with a cubic spline interpolation to smooth out the surface, in Figures 5-1(a) and 5-1(b).

Equation 5.23 is then used to compute the free energy surface for C-O bond breaking in chabazite (Figure 5-2), sampled across the C_1-O distance and [(C_1-H*) - (C_2-H*)] asymmetric stretch reaction coordinates.

Based on the free energy surface in Figure 5-2, there are two possible dynamic pathways connecting the reactant and intermediate species: one involving two distinct

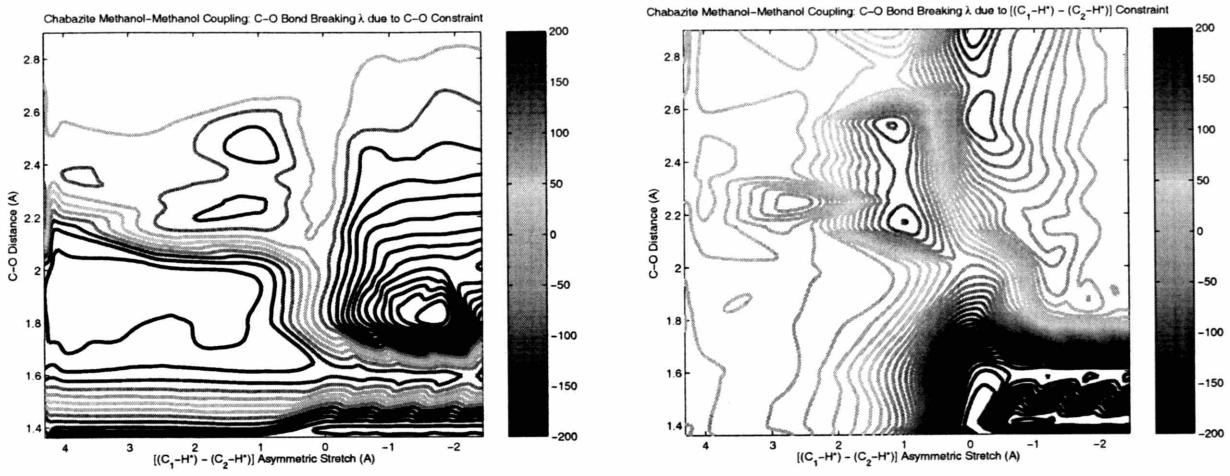

(a) (b)

Figure 5-1: λ due to (a) C_1-O distance and (b) [(C_1-H*) - (C_2-H*)] asymmetric stretch constrained reaction coordinates in chabazite

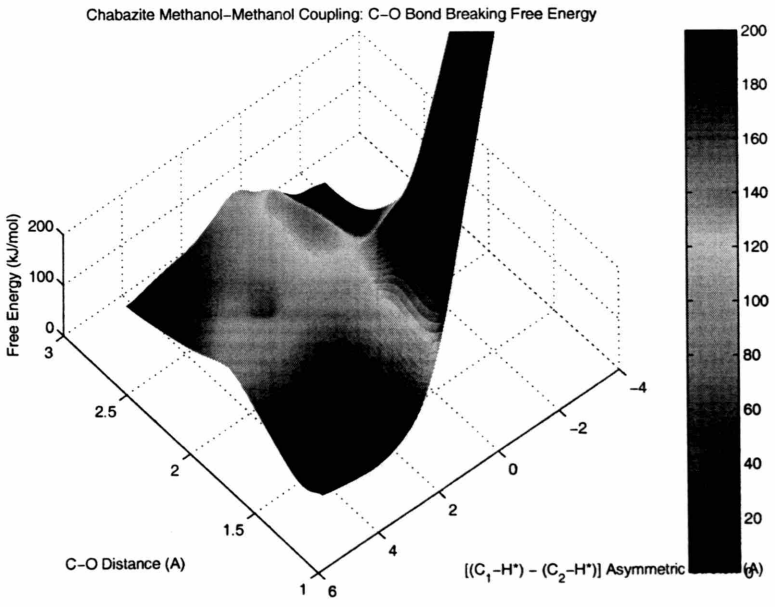

Figure 5-2: Free energy surface for C-O bond breaking in chabazite

steps, and the other passing over only one transition state to the intermediates. The two-step mechanism involves an initial C-O bond breaking, where the system ends up in a metastable free energy basin to the left of Figure 5-2. Then, the system must cross over another barrier into the intermediate basin. In the pseudo one-step pathway, the breaking of the C-O bond occurs simultaneously with the other methanol moving close enough to enable the proton transfer to the methyl cation.

The initial free energy barrier to cross into the metastable state is about 80.1 kJ/mol, the metastable state is 54.2 kJ/mol higher in free energy compared to the reactant state, and the second free energy barrier to cross from the metastable state to the intermediates is 37.8 kJ/mol. This gives a total free energy barrier of 117.9 kJ/mol, which makes this two-step pathway favored relative to the pseudo one-step pathway's barrier of 126.9 kJ/mol at the saddle point.

For the C-O bond breaking step in the gas phase, the two reaction coordinates were simultaneously constrained in a pairwise fashion at the following values:

- C_1-O distance (ξ_1): 1.518 (unconstrained), 1.6, 1.8, 2.0, 2.15, 2.25, 2.35, 2.45, 2.55, 2.7, 2.9 Å

- [(C_1-H*) - (C_2-H*)] asymmetric stretch (ξ_2): 4.011 (unconstrained), 4.0, 2.5, 1.0, 0.0, -0.6, -1.2, -1.8, -2.4, -3.0 Å

The λ's due to each constraint are plotted, with a cubic spline interpolation to smooth out the surface, in Figures 5-3(a) and 5-3(b).

Equation 5.23 is then used to compute the free energy surface for C-O bond breaking in the gas phase (Figure 5-4), sampled across the C_1-O distance and [(C_1-H*) - (C_2-H*)] asymmetric stretch reaction coordinates.

Again, the free energy surface shows two possible pathways, one two-step, the other pseudo one=step. The free energy of the metastable basin is 72.9 kJ/mol, so the free energy barriers for the two-step pathway are 135.9 kJ/mol and 79.9 kJ/mol for total of 215.8 kJ/mol. The free energy barrier for the one-step pathway is 150.1 kJ/mol, so it is the favored pathway.

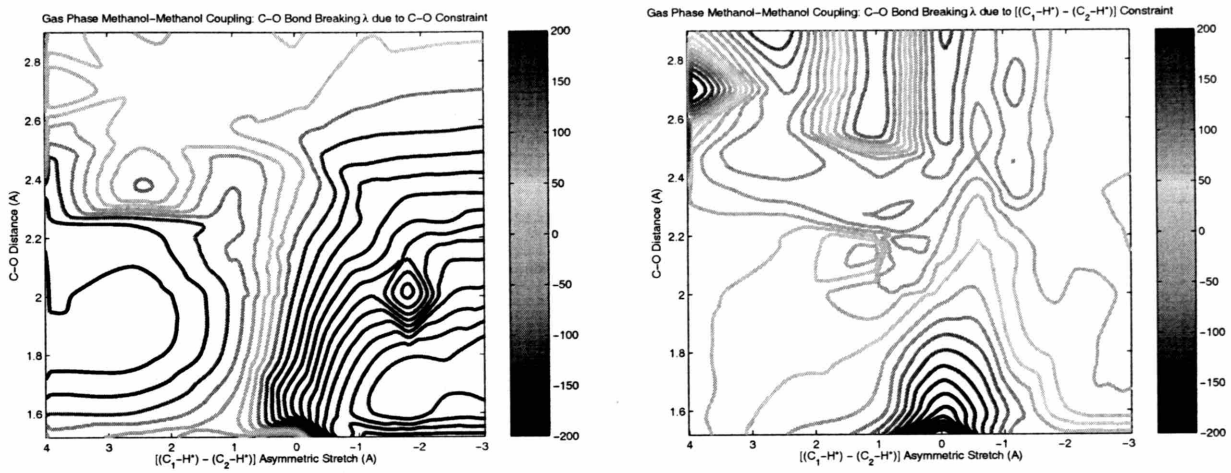

(a) (b)

Figure 5-3: λ due to (a) C_1-O distance and (b) [(C_1-H*) - (C_2-H*)] asymmetric stretch constrained reaction coordinates in the gas phase

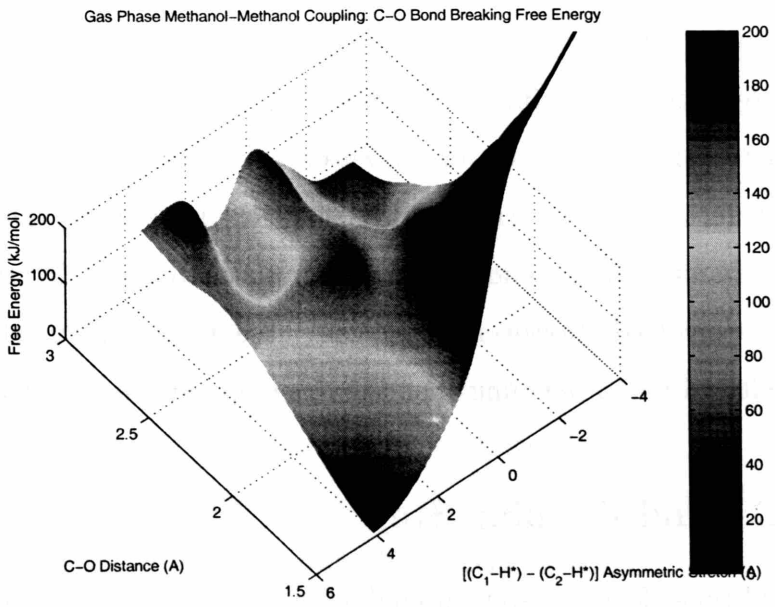

Figure 5-4: Free energy surface for C-O bond breaking in the gas phase

Table 5.1: Comparison of saddle point locations, based on the reaction coordinates C_1-O distance (Å) and [(C_1-H*) - (C_2-H*)] asymmetric stretch (Å) for C-O bond breaking in chabazite and in the gas phase

	One Step		Two Step: TS1		Two Step: TS2	
	C_1-O	[(C_1-H*) - (C_2-H*)]	C_1-O	[(C_1-H*) - (C_2-H*)]	C_1-O	[(C_1-H*) - (C_2-H*)]
Chabazite	2.2	0.0	2.1	2.1	2.9	0.7
Gas Phase	2.1	0.5	2.3	3.3	2.5	0.4

Table 5.2: Comparison of free energy barriers (kJ/mol) for one-step and two-step pathways for C-O bond breaking in chabazite and in the gas phase

	One Step	Two Step		
	ΔF	ΔF_{TS1}	ΔF_{TS2}	$\Delta F_{overall}$
Chabazite	**126.9**	80.1	37.8	**117.9**
Gas Phase	**150.1**	135.9	79.9	**215.8**

A comparison of the differences in the location of the saddle points and the heights of the free energy barriers is given in Tables 5.1 and 5.2, respectively. The difference in the overall free energy barrier between the reaction in the gas phase (150.1 kJ/mol) and in chabazite (117.9 kJ/mol) is a little more than 30 kJ/mol, but the overall form of the free energy surfaces is similar. In chabazite, the C-O bond breaking and the H* transfer are two distinct steps, and the water, once formed, does not play a role in the proton transfer at all. The framework is sufficient for keeping the methyl cation and second methanol in close enough proximity to enable the H* transfer without having the water involved. However, in the gas phase, the species must all be in close enough proximity to react, meaning that the one step pathway is favored.

5.3.2 C-C Bond Forming Step

For the C-C bond forming step in chabazite, the two reaction coordinates were simultaneously constrained in a pairwise fashion at the following values:

- C_1-C_2 distance (ξ_1): 3.706 (unconstrained), 3.4, 3.1, 2.8, 2.5, 2.2, 2.0, 1.8, 1.6 Å

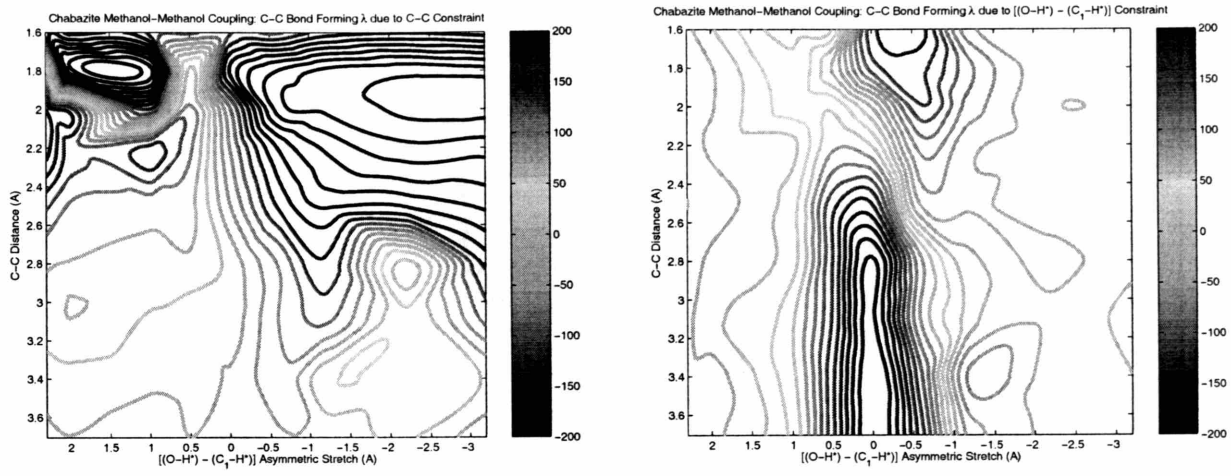

(a) (b)

Figure 5-5: λ due to (a) C_1-C_2 distance and (b) [(O-H*) - (C_1-H*)] asymmetric stretch constrained reaction coordinates in chabazite

- [(O-H*) - (C_1-H*)] asymmetric stretch (ξ_2): 2.3 (unconstrained), 2.0, 1.0, 0.5, 0.0, -0.6, -1.2, -2.2, -3.2 Å

The λ's due to each constraint are plotted, with a cubic spline interpolation to smooth out the surface, in Figures 5-5(a) and 5-5(b).

Equation 5.23 is then used to compute the free energy surface for C-C bond forming in chabazite (Figure 5-6), sampled across the C_1-C_2 distance and [(O-H*) - (C_1-H*)] asymmetric stretch reaction coordinates.

Only one saddle point is seen in Figure 5-6. The free energy barrier corresponding to this saddle point is 106.0 kJ/mol. Since the intermediate state is 11.1 kJ/mol lower in free energy than the reactant state, the corrected C-C bond forming barrier height is 94.9 kJ/mol. The products are 31.3 kJ/mol lower in free energy than the intermediate state. For the overall reaction, the ethanol and water products are 42.4 kJ/mol lower in energy than the two methanol reactants.

For the C-C bond forming step in the gas phase, the two reaction coordinates were constrained at the following values:

- C_1-C_2 distance (ξ_1; unconstrained = 4.335 Å): 4.3, 4.0, 3.7, 3.4, 3.1, 2.8, 2.5,

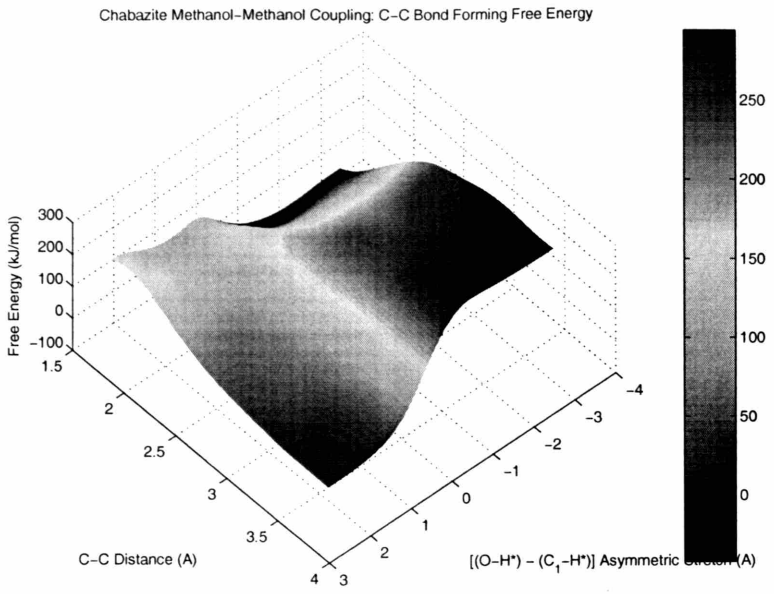

Figure 5-6: Free energy surface for C-C bond forming in the chabazite

2.2, 1.9, 1.6 Å

- [(O-H*) - (C_1-H*)] asymmetric stretch (ξ_2; unconstrained = 2.795 Å): 2.2, 1.6, 1.0, 0.5, 0.0, -0.6, -1.2, -2.2, -3.2, -4.2 Å

The λ's due to each constraint are plotted, with a cubic spline interpolation to smooth out the surface, in Figures 5-7(a) and 5-7(b).

Equation 5.23 is then used to compute the free energy surface for C-C bond forming in the gas phase (Figure 5-8), sampled across the C_1-C_2 distance and [(O-H*) - (C_1-H*)] asymmetric stretch reaction coordinates.

The free energy surface seems to show two pathways. On the left of Figure 5-8, one pathway crosses a saddle point (C_1-C_2 = 1.8 Å, [(O-H*) - (C_1-H*)] = 0.2 Å; ΔF = 128.5 kJ/mol) on its way to the product state, and this pathway corresponds to the simultaneous transfer of a proton from methane to water, and the formation of the C-C bond between the methyl anion and protonated formaldehyde. On the right hand side of Figure 5-8, the second pathway seems to go through a very low-lying saddle point (C_1-C_2 = 3.8 Å, [(O-H*) - (C_1-H*)] = 0.2 Å; ΔF = 50.0 kJ/mol), through a valley, into the product state. This second pathway is not representative of the reaction

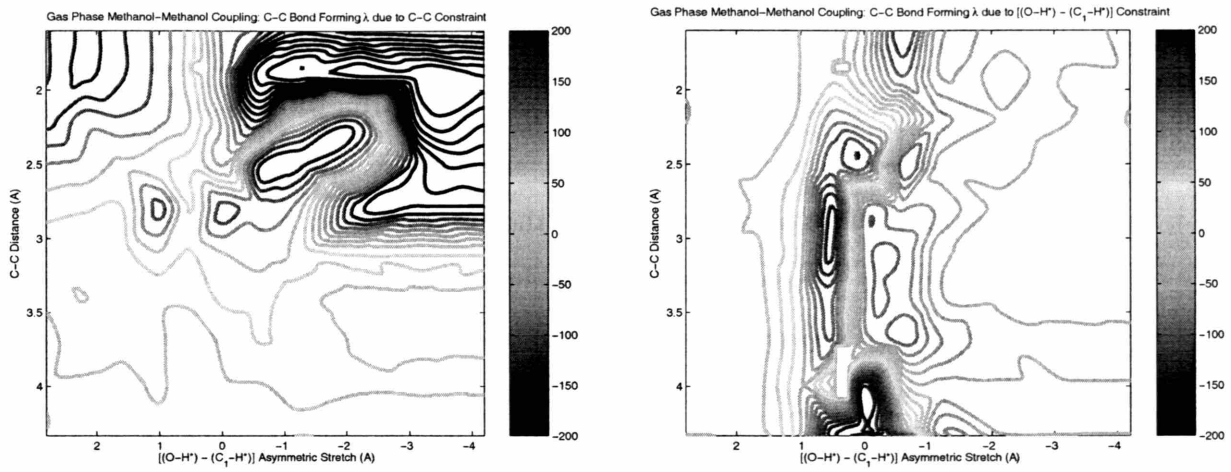

(a) (b)

Figure 5-7: λ due to (a) C_1-C_2 distance and (b) [(O-H*) - (C_1-H*)] asymmetric stretch constrained reaction coordinates in the gas phase

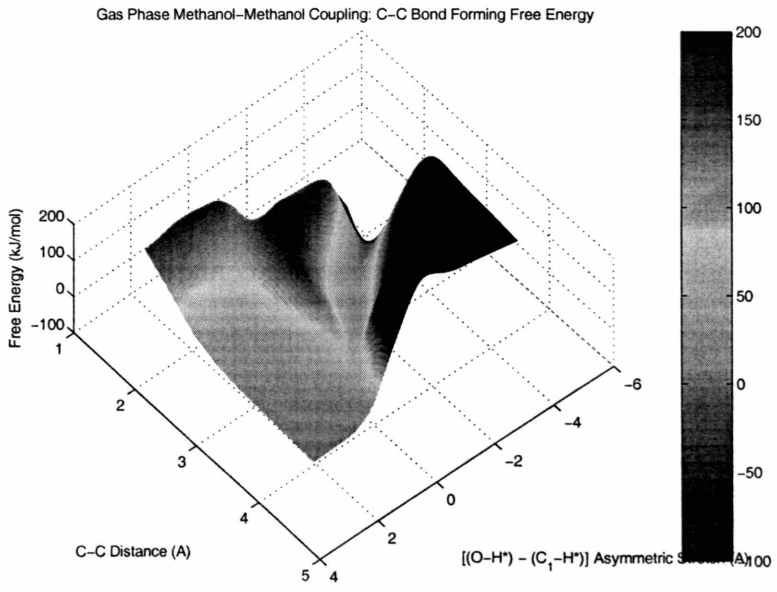

Figure 5-8: Free energy surface for C-C bond forming in the gas phase

of interest, as the low-lying saddle point corresponds to the concerted transfer of a proton from protonated formaldehyde to methane, and then from methane to water, much like what was seen in Figure 4-8 in Section 4.3.1. Methyl anion, with a proton affinity of 1743.5 kJ/mol [55], and water, with a proton affinity of 723.8 kJ/mol [2], are much more stable as the methane and hydroxonium cations, respectively, and are located in close proximity due to the constraint on the [(O-H*) - (C_1-H*)] asymmetric stretch. However, once formaldehyde is formed, it is very stable, and the constrained C_1-C_2 distance is large enough (3.7 Å) so that formaldehyde does not participate in any further reaction. Ethanol can never form even if the C_1-C_2 distance constraint is released, since there are no external physical constraints, such as a crystalline framework, keeping formaldehyde in close proximity with the other reactants. Therefore, this pathway does not lead to the formation of a C-C bond.

It is instructive to note that this low-lying pathway, corresponding to the formation of formaldehyde, methane, and hydroxonium cation with the C-C distance being relatively large, does not exist in the zeolite, as depicted by the free energy surface in Figure 5.6. In the zeolite, formaldehyde and the hydroxonium cation cannot be too far apart due to molecular shape selectivity from the framework. Even if proton transfer from CH_2OH^+ to H_2O occurs, it is reversible due to the close proximity of the two species, and eventually the preferred pathway for ethanol formation, where methane transfers a proton to water, will be followed. Unfortunately, in the gas phase, the formaldehyde is not at all close to the hydroxonium cation; in fact they are separated by methane and arranged in a linear configuration.

Instead, the pathway that does lead to ethanol formation must go through the higher saddle point, so the free energy barrier at the saddle point is 128.5 kJ/mol. However, the intermediate gas phase species are 30.7 kJ/mol higher in free energy compared to the gas phase reactants (methanol and methoxonium cation). Therefore, the corrected saddle point height is 159.2 kJ/mol. The products are 67.0 kJ/mol lower in free energy than the reactants.

A comparison of the saddle point locations and free energy barriers to C-C bond forming, given in Table 5.3, shows that the chabazite framework does keep the hy-

Table 5.3: Comparison of saddle point locations, based on the reaction coordinates C_1-C_2 distance (Å) and [(O-H*) - (C_1-H*)] asymmetric stretch (Å), and free energy barriers (kJ/mol) for C-C bond forming in chabazite and in the gas phase

	C-C	[(O-H*) - (C_1-H*)]	ΔF
Chabazite	2.0	1.0	**106.0**
Gas Phase	1.8	0.2	**128.5**

Table 5.4: Free energy barriers at various points along methanol coupling reaction pathway

	Reactants	$\Delta F_{\text{C-O bond breaking}}$	Intermediates	$\Delta F_{\text{C-C bond forming}}$	Products
Chabazite	0	117.9	-11.1	94.9	-42.4
Gas Phase	0	150.1	30.7	159.2	-67.0

drocarbons in close enough proximity to react. The molecular shape selectivity effect is not too large, since the difference in free energy barriers is about 22.5 kJ/mol and the location of the saddle points is similar. The transition state in chabazite is more reactant-like, with H* closer to methane, whereas the transition state in the gas phase is more product-like, with H* closer to water. The product-like transition state in the gas phase indicates that the C-C bond forming reaction is endothermic and thus not thermodynamically favored in the absence of the zeolite framework.

5.3.3 Overall Free Energy Surfaces

The overall free energy surface for the methanol coupling reaction in chabazite is given in Figure 5-9, and in the gas phase in Figure 5-10.

Also, the heights of the relevant points on the free energy surfaces are given in Table 5.4.

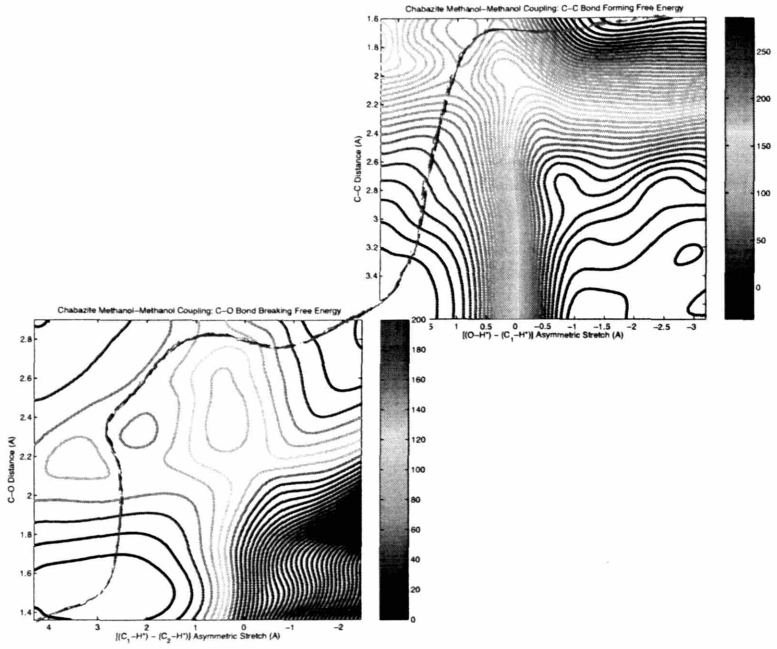

Figure 5-9: Overall free energy surface for methanol coupling reaction in chabazite

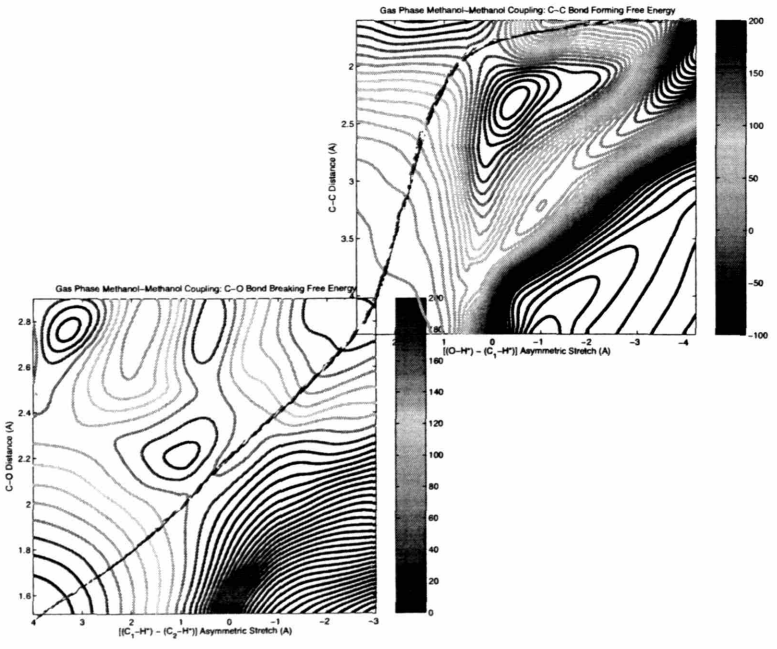

Figure 5-10: Overall free energy surface for methanol coupling reaction in the gas phase

5.4 Conclusions

The free energy barriers for the two-step methanol coupling reaction in both chabazite and in the gas phase have been computed via constrained molecular dynamics and the blue-moon ensemble approach. The reaction coordinates for the first step of the reaction are suspected to be the C-O distance and the [(C_1-H*) - (C_2-H*)] asymmetric stretch. The reaction coordinates for the second step of the reaction are suspected to be the C-C distance and the [(O-H*) - (C_1-H*)] asymmetric stretch. Further studies would need to be performed to verify these.

Chapter 6

Conclusions and Future Work

The overall goals of this thesis were to: 1. Develop a quantitative understanding of the acid sites in the zeolite chabazite, specifically to determine the effect of local structural defects on energetic properties at the acid sites, and to evaluate several measures to probe the acid strength of the Brønsted sites, 2. Develop an understanding of how zeolites catalyze solid state reactions, specifically to compute the mechanism for the methanol coupling reaction in the zeolite chabazite. State-of-the-art computational methods, including density functional theory, Car-Parrinello molecular dynamics, constrained molecular dynamics, and transition path sampling, were used to calculate energetic and spectroscopic properties and simulate reactive processes.

6.1 Characterization of Acid Sites

It was confirmed, using both ELF visualization and constrained geometry optimizations, that there are two minima for proton positions on the oxygens at the acid site of the zeolite chabazite. The four acidic oxygens at the aluminum T-site all have roughly the same deprotonation energy, which is not strictly correlated to the O-H bond length or stretch vibrational frequency. Furthermore, the adsorption energy of various bases at each acid site oxygen is roughly the same and correlates well only with the gas-phase proton affinity of the base. Therefore, the construction

of a universal scale for quantifying zeolite acidity is likely to be problematic. Also, the deprotonation energies and base adsorption energies are not significantly changed with the presence of additional aluminum substituents in the zeolite framework, nor with silanol framework defects near the acid site.

6.1.1 Correlation of Acid Strength to Catalytic Activity

All of the calculations in this thesis were performed on a chabazite model with an Al-substituted silicate framework. It has been found that the rates of high-temperature *n*-hexane cracking and room-temeperature propene oligomerization are much higher for H-[Al]ZSM-5 and H-[Ga]ZSM-5 than H-[Fe]ZSM-5. These results were obtained from microcalorimetry and temperature-programmed desorption (TPD) experiments, where the zeolite surface was initially saturated with ammonia or pyridine gas, and then the temperature was ramped up slowly while keeping the zeolite sample in a flowing inert gas stream [57].

The experimentally measured quantities correlate with catalytic activity, whereas the calculated base adsorption energies correlate with acid strength. An analogous set of calculations as those presented in Section 3.3 could be performed on Ga- and Fe-substituted chabazite. If the adsorption energy of ammonia on Al- and Ga-substituted chabazite is much higher, or much lower, than for Fe-substituted chabazite, then it can be concluded that base adsorption energy can be correlated to catalytic activity. The deprotonation energy of the Brønsted site on Al-, Ga-, and Fe-substituted chabazite should also be compared to determine if it is correlated to catalytic activity.

6.1.2 Generalization of Acid Site Properties to Other Zeolites

The results of this thesis would be even more useful, for understanding how zeolites catalyze reactions and for designing new catalysts, if they could be compared to the base adsorption energies on a different, more catalytically active zeolite such as faujasite or ZSM-5. Both faujasite and ZSM-5 resemble chabazite in terms of

chemical composition, crystal structure, and distribution. Also, both faujasite (7.4 Å) and ZSM-5 (5.5 Å) have larger pore size diameters than chabazite, so they can be used for petrochemical reactions involving larger molecules such as aromatics and longer-chain hydrocarbons. Unfortunately, faujasite contains 576 atoms, and ZSM-5 288 atoms, in its unit cell, so it will a huge computational challenge to successfully optimize the crystalline structure of either zeolite with one aluminum substituent. However, rapid advances in computing power over the past 5-10 years have made it feasible to perform *ab initio* calculations on large solid systems such as ZSM-5 [66] or million-atom nanostructures.

Therefore, an analogous set of calculations as those presented in Section 3.3 could be performed on the other zeolite, whether it be faujasite or ZSM-5 or another zeolite entirely, and the results used to derive generalizations about the nature of acid sites in zeolites. A comparison of the base adsorption energies on ZSM-5 and chabazite, for example, would be very useful in determining whether differences in base adsorption energies are correlated to differences in acidity and/or catalytic activity between zeolites. For instance, if the adsorption energy of methanol on ZSM-5 and chabazite is roughly the same, but ZSM-5 is known to be more catalytically active for the MTG reaction than chabazite [150], then it can be concluded that not only will it be impossible to develop a base-independent scale for solid acidity, but that the base adsorption energy is not a good measure of catalytic activity. As another example, if the adsorption energy of methanol on the four acid sites of faujasite varies by over 20 kJ/mol, then it is safe to say that the Brønsted sites in faujasite are heterogeneous in acid strength, whereas the sites in chabazite seem to be homogeneous in acid strength.

6.2 Methanol Coupling Reaction in Chabazite

Transition path sampling and constrained molecular dynamics methods have been used to study an acid-catalyzed reaction in the zeolite chabazite. In particular, a new mechanism was found for the C-C bond formation in the methanol coupling reaction that does not involve the formation of dimethyl ether or surface methoxy groups at the

acid site. This two-step mechanism at 400 °C proceeds through stable intermediates of water, methane, and protonated formaldehyde to form ethanol. The C-C bond forms directly and concurrently with a proton transfer from methane to water.

The free energy barriers for the methanol coupling reaction in both chabazite and in the gas phase were computed via constrained molecular dynamics and the blue-moon ensemble approach. The two-step mechanism is likely to be the correct reaction mechanism in chabazite, since it has a lower free energy barrier, 117.9 kJ/mol, than the barrier corresponding to the one-step mechanism, 223.5 kJ/mol. Both steps of the reaction have roughly the same activation energy, meaning that neither step is slow or rate-limiting compared to the other. However, the large barrier to the overall formation of the C-C bond means that it may still be the rate-limiting step of the MTG and MTO processes.

Although the overall mechanisms for methanol coupling in chabazite and in the gas phase are similar, the free energy barriers for the reaction in chabazite are generally much lower. Therefore, the zeolite framework is likely to be most important for molecular shape selectivity and short-range repulsions.

6.2.1 Investigation of Alternative Reaction Mechanisms

The mechanism described in Section 4.3.2 is valid at 400 °C. However, it has been well postulated that the methanol molecules may couple to form dimethyl ether in either a sequential or competing reaction. This process may also be temperature dependent. Therefore, it is important to develop a means of quickly finding and screening reaction pathways, even non-dynamic ones, that is less computationally intensive than constrained molecular dynamics.

The dimer [71] and biased transition state [112] methods have been developed to find an initial reaction path given only the reactants. If either of these methods were able to find appropriate reaction pathways, balancing speed with convergence, then they could be implemented into the CPMD code and used to determine the temperature dependence of the methanol coupling reaction pathway, perhaps at temperatures ranging from 300 ° C to 500 ° C.

Another idea, spurred by the recent work on hydrocarbon pool mechanisms [131, 62, 132, 115, 116, 70], is that surface methoxy groups may lower the free energy barrier to the methanol coupling reaction. Therefore, either the 1,3-dimethylcyclopentenyl cation adsorbed onto the acid site in place of a proton, or toluene trapped in the chabazite 6T cage, would result in a dangling methyl group in the main 8T ring. The reaction mechanism for methanol coupling in the presence of the dangling methyl group could then be computed by either the dimer or biased transition state method.

Either the nudged elastic band (NEB) [78] or action-derived molecular dynamics [107] methods could be used to determine a reaction pathway given the reactants and products. Again, if either method were implemented into the CPMD code, it could be used to verify the mechanism described in Section 4.3.2, with perhaps much less computational effort than constrained molecular dynamics. However, the need to specify the products *a priori* means that the NEB method is not as useful when screening for side reactions.

6.2.2 Identification and Verification of Reaction Coordinates

It still needs to be determined whether the chosen coordinates, namely the C_1-O distance and the [(C_1-H*) - (C_2-H*)] asymmetric stretch for the C-O bond breaking step, and the C_1-C_2 distance and the [(O-H*) - (C_1-H*)] asymmetric stretch for the C-C bond forming step, are sufficient for driving the methanol coupling reaction by calculating the committor distributions at the saddle regions shown in Figures 5-2, 5-4, 5-6, and 5-8.

Unfortunately, the driving coordinates for the reaction in chabazite may turn out to be different than those for the reaction in the gas phase. At the saddle points depicted in Figures 5-4 and 5-8, preliminary calculations show that the committor distributions, for both steps of the reaction in the gas phase, are generally flat or skewed, as shown in Figures 2-3(b) and 2-4(b), respectively. This means that there is diffusive behavior at the saddle regions, or that the correct transition state has not been captured in the gas phase. This is especially true for the C-C bond forming step, where the free energy surfaces for the reaction in chabazite (Figure 5-6 and in the gas

phase (Figure 5-8) are very different and hence the governing reaction coordinates are also likely to be very different.

Although the committor calculations are computationally expensive, they must first be performed on the chabazite system to verify the correctness of the reaction coordinates, which were determined by observing the bond breaking and bond forming processes in the converged mechanism found in Section 4.3.2. If the chosen coordinates are not correct even for the chabazite system, then a new set of coordinates must be proposed and the constrained molecular dynamics calculations performed again. Only after the driving coordinates for the reaction in chabazite have been verified, and the correct transition state(s) captured, should the corresponding committor calculations be performed for the gas phase system.

6.2.3 Comparison of Reaction Rates in Chabazite and in the Gas Phase

Though it appears free energy barriers to reaction are lower in chabazite than in the gas phase, it is still unknown whether this necessarily corresponds to increased reaction rates in the presence of a catalyst. Therefore, once the correctness of the reaction coordinates has been confirmed, it would be useful to compute the rates of reaction for both steps of the methanol coupling reaction, in chabazite and in the gas phase. The reaction rate constant is given by:

$$k_{A\rightarrow B} = \frac{1}{\tau_{mol}} exp\left(-\frac{\Delta F^{TS}}{k_B T}\right) \tag{6.1}$$

The autocorrelation function from transition path sampling can be plotted to determine τ_{mol}, which is the characteristic relaxation time associated with the barrier crossing of the transition state region. Using a set of order parameters $\chi = \{\chi_1, \chi_2, \}$, ranging from 0 to 1, that characterize the metastable free energy basins A and B, the autocorrelation function is defined as $\langle \chi_i(0)\, \chi_i(t) \rangle$. When plotted from $t = 0$ to $t = \mathcal{T}$, τ_{mol} is the time taken for the gradual transition of the autocorrelation function to move from 0 to 1, as shown in Figure 6-1.

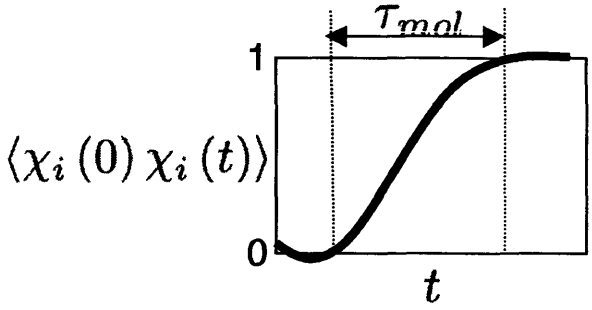

Figure 6-1: Schematic of autocorrelation function $\langle \chi_i(0)\, \chi_i(t) \rangle$ versus time for calculating the characteristic relaxation time τ_{mol} associated with barrier crossing of the transition state region

Bibliography

[1] J. B. Anderson. Statistical theories of chemical reactions. distributions in the transition region. *J. Chem. Phys.*, 58(10):4684–4692, 1973.

[2] D. H. Aue and M. T. Bowers. Stabilites of positive ions from equilibrium gas-phase basicity measurements. In M. T. Bowers, editor, *Gas Phase Ion Chemistry*, volume 2, chapter 9, pages 2–52. Academic Press, New York, 1979.

[3] S. M. Babitz, B. A. Williams, J. T. Miller, R. Q. Snurr, W. O. Haag, and H. H. Kung. Monomolecular cracking of n-hexane on Y, MOR, and ZSM-5 zeolites. *Appl. Catal. A: Gen.*, 179(1-2):71–86, 1999.

[4] L. A. M. M. Barbosa and R. A. van Santen. Influence of zeolite framework geometry structure on the stability of the $[ZnOZn]^{2+}$ cluster by periodical density functional theory. *J. Phys. Chem. B*, 107(19):4532–4536, 2003.

[5] P. T. Barger and S. T. Wilson. Converting natural gas to ethylene and propylene by the UOP/Hydro MTO process. In M. M. J. Treacy, B. K. Marcus, M. E. Bisher, and J. B. Higgins, editors, *Proceedings of the 12th International Zeolite Conference*, volume 1, pages 567–574, Warrendale, PA, 1999. Materials Research Society.

[6] P. A. Barrett, R. H. Jones, J. M. Thomas, G. Sankar, I. J. Shannon, and C. R. A. Catlow. Rational design of a solid acid catalyst for the conversion of methanol to light alkenes: Synthesis, structure and performance of DAF-4. *J. Chem. Soc. Chem. Comm.*, (17):2001–2002, 1996.

[7] E. R. Batista and H. Jónsson. Diffusion and island formation on the ice Ih basal plane surface. *Comp. Mater. Sci.*, 20(3-4):325–336, 2001.

[8] A. D. Becke. Density-functional exchange-energy approximation with correct asymptotic behavior. *Phys. Rev. A*, 38:3098–3100, 1988.

[9] A. D. Becke and K. E. Edgecombe. A simple measure of electron localization in atomic and molecular systems. *J. Chem. Phys.*, 92(9):5397–5403, 1990.

[10] C. H. Bennett. Molecular dynamics and transition state theory: The simulation of infrequent events. In R. E. Christoffersen, editor, *Algorithms for Chemical Computations*, volume 46 of *ACS Symposium Series*, pages 63–97, Washington D.C., 1977. American Chemical Society, American Chemical Society.

[11] A. I. Biaglow, A. T. Adamo, G. T. Kokotailo, and R. J. Gorte. An examination of the acid sites in SAPO-5. *J. Catal.*, 131:1991, 1991.

[12] A. I. Biaglow, R. J. Gorte, G. T. Kokotailo, and D. White. A probe of Brønsted site acidity in zeolites: ^{13}C chemical shift of acetone. *J. Catal.*, 148:779–786, 1994.

[13] S. R. Blaszkowski and R. A. van Santen. The mechanism of dimethyl ether formation from methanol catalyzed by zeolitic protons. *J. Am. Chem. Soc.*, 118(21):5152–5153, 1996.

[14] S. R. Blaszkowski and R. A. van Santen. Methanol adsorption and activation by zeolitic protons. In *Progress in Zeolite and Microporous Materials, Part A-C*, volume 105 of *Studies in Surface Science and Catalysis*, pages 1707–1714, Zürich, Switzerland, 1997. International Zeolite Association.

[15] S. R. Blaszkowski and R. A. van Santen. Theoretical study of C-C bond formation in the methanol-to-gasoline process. *J. Am. Chem. Soc.*, 119(21):5020–5027, 1997.

[16] S. R. Blaszkowski and R. A. van Santen. Theoretical study of the mechanism of surface methoxy and dimethyl ether formation from methanol catalyzed by zeolitic protons. *J. Phys. Chem. B*, 101(13):2292–2305, 1997.

[17] P. G. Bolhuis, D. Chandler, C. Dellago, and P. L. Geissler. Transition path sampling: Throwing ropes over rough mountain passes, in the dark. *Annu. Rev. Phys. Chem.*, 53:291–318, 2002.

[18] P. G. Bolhuis, C. Dellago, and D. Chandler. Sampling ensembles of deterministic transition pathways. *Faraday Discuss.*, 110:421–436, 1998.

[19] P. G. Bolhuis, C. Dellago, and D. Chandler. Reaction coordinates of biomolecular isomerization. *Proc. Natl. Acad. Sci. U. S. A.*, 97(11):5877–5882, 2000.

[20] M. Bonn, R. A. van Santen, J. A. Lercher, A. W. Kleyn, and H. J. Bakker. Picosecond infrared activation of methanol in acid zeolites. *Chem. Phys. Lett.*, 278(4-6):213–219, 1997.

[21] M. Brändle and J. Sauer. Acidity differences between inorganic solids induced by their framework structure. a combined quantum mechanics/molecular mechanics *ab initio* study on zeolites. *J. Am. Chem. Soc.*, 120(7):1556–1570, 1998.

[22] M. Brändle, J. Sauer, R. Dovesi, and N. M. Harrison. Comparison of a combined quantum mechanics/interatomic potential function approach with its periodic quantum-mechanical limit: Proton siting and ammonia adsorption in zeolite chabazite. *J. Chem. Phys.*, 109(23):10379–10389, 1998.

[23] B. R. Brooks, R. E. Bruccoleri, B. D. Olafson, D. J. States, S. Swaminathan, and M. Karplus. CHARMM: A program for macromolecular energy, minimization, and dynamics calculations. *J. Comput. Chem.*, 4:187–217, 1983.

[24] E. Brunner, H. Ernst, D. Freude, T. Fröhlich, M. Hunger, and H. Pfeifer. Magic-angle-spinning NMR studies of acid sites in zeolite H-ZSM-5. *J. Catal.*, 127(1):34–41, 1991.

[25] M. Calligaris, G. Nardin, L. Randaccio, and P. Comin Chiaramonti. Cation-site location in a natural chabazite. *Acta. Crystallogr. B*, 38(2):602–605, 1982.

[26] R. Car and M. Parrinello. Unified approach for molecular dynamics and density-functional theory. *Phys. Rev. Lett.*, 55(22):2471–2474, 1985.

[27] E. A. Carter, G. Ciccotti, J. T. Hynes, and R. Kapral. Constrained reaction coordinate dynamics for the simulation of rare events. *Chem. Phys. Lett.*, 156(5):472–477, 1989.

[28] D. M. Ceperley and B. J. Alder. Ground state of the electron gas by a stochastic method. *Phys. Rev. Lett.*, 45(7):566–569, 1980.

[29] D. Chandler. Statistical mechanics of isomerization dynamics in liquids and the transition state approximation. *J. Chem. Phys.*, 68(6):2959–2970, 1978.

[30] D. Chandler. Barrier crossings: Classical theory of rare but important events. In B. J. Berne, G. Ciccotti, and D. F. Coker, editors, *Classical and Quantum Dynamics in Condensed Phase Simulations*, pages 3–23. World Scientific, Singapore, 1998.

[31] D. Chandler. Finding transition pathways: Throwing ropes over rough mountain passes, in the dark. In B. J. Berne, G. Ciccotti, and D. F. Coker, editors, *Classical and Quantum Dynamics in Condensed Phase Simulations*, pages 51–66. World Scientific, Singapore, 1998.

[32] C. D. Chang, J. C. W. Kuo, W. H. Lang, S. M. Jacob, J. J. Wise, and A. J. Silvestri. Process studies on the conversion of methanol to gasoline. *Ind. Eng. Chem. Proc. Des. Dev.*, 17(3):255–260, 1978.

[33] C. D. Chang and A. J. Silvestri. The conversion of methanol and other O-compounds to hydrocarbons over zeolite catalysts. *J. Catal.*, 47:249–259, 1977.

[34] N. Y. Chen and W. J. Reagan. Evidence of autocatalysis in methanol to hydrocarbon reactions over zeolite catalysts. *J. Catal.*, 50:123–129, 1979.

[35] J.-W. Chu, B. R. Brooks, and B. L. Trout. A super-linear minimization scheme for the nudged elastic band method. *J. Chem. Phys.*, 119(24):12708–12717, 2003.

[36] J. W. Chu, B. R. Brooks, and B. L. Trout. QM/MM and free energy simulations of the oxidation of methionine residues in aqueous solutions, free methionine and methionine in G-CSF. *J. Am. Chem. Soc.*, submitted.

[37] G. Ciccotti and M. Ferrario. Rare events by constrained molecular dynamics. *J. Mol. Liq.*, 89:1–2, 2000.

[38] J. H. Clark and C. N. Rhodes. *Clean Synthesis Using Porous Inorganic Solid Catalysts and Supported Reagents.* RSC Clean Technology Monographs. Royal Society of Chemistry, University of York, UK, May 2000.

[39] J. K. A. Clarke, R. Darcy, B. F. Hegarty, E. O'Donoghue, V. Amir-Ebrahimi, and J. J. Rooney. Free-radicals in dimethyl ether on H-ZSM-5 zeolite – a novel dimension of heterogeneous catalysis. *J. Chem. Soc. Chem. Comm.*, (5):425–426, 1986.

[40] S. J. Cook, A. K. Chakraborty, A. T. Bell, and D. N. Theodorou. Structural and electronic features of a Brønsted acid site in H-ZSM-5. *J. Phys. Chem.*, 97(25):6679–6685, 1993.

[41] O. Couronne and Y. Ellinger. An *ab initio* and DFT study of $(N_2)_2$ dimers. *Chem. Phys. Lett.*, 306:71–77, 1999.

[42] I. M. Dahl, H. Mostad, D. Akporiaye, and R. Wendelbo. Structural and chemical influences on the MTO reaction: A comparison of chabazite and SAPO-34 as MTO catalysts. *Micropor. Mesopor. Mat.*, 29(1-2):185–190, 1999.

[43] S. Damoun, W. Langenaeker, and P. Geerlings. Acidity of zeolites and silanols: Study of the influence of size and softness of the global system on the electronegativity–softness competition in halogenated model systems. *J. Phys. Chem. A*, 101(37):6951–6954, 1997.

[44] E. Darve and A. Pohorille. Calculating free energies using average force. *J. Chem. Phys.*, 115(20):9169–9183, 2001.

[45] S. J. DeCanio, J. R. Sohn, P. O. Fritz, and J. H. Lunsford. Acid catalysis by dealuminated zeolite-Y. 1. methanol dehydration and cumene dealkylation. *J. Catal.*, 101(1):132–141, 1986.

[46] C. Dellago, P. G. Bolhuis, and D. Chandler. Efficient transition path sampling: Application to Lennard-Jones cluster rearrangements. *J. Chem. Phys.*, 108(22):9236–9245, 1998.

[47] C. Dellago, P. G. Bolhuis, and D. Chandler. On the calculation of reaction rate constants in the transition path ensemble. *J. Chem. Phys.*, 110(14):6617–6625, 1999.

[48] C. Dellago, P. G. Bolhuis, F. S. Csajka, and D. Chandler. Transition path sampling and the calculation of rate constants. *J. Chem. Phys.*, 108(5):1964–1977, 1998.

[49] W. K. den Otter and W. J. Briels. Free energy from molecular dynamics with multiple constraints. *Mol. Phys.*, 98(12):773–781, 2000.

[50] E. G. Derouane. Confinement effects in sorption and catalysis by zeolites. In D. Barthomeuf, E. G. Derouane, and W. Hölderich, editors, *Guidelines for Mastering the Properties of Molecular Sieves*, volume 221, pages 225–239. Plenum Press, New York, 1990.

[51] E. G. Derouane. Zeolites as solid solvents. *J. Mol. Catal. A: Chem.*, 134:29–45, 1998.

[52] E. G. Derouane and C. D. Chang. Confinement effects in the adsorption of simple bases by zeolites. *Micropor. Mesopor. Mat.*, 35-36:425–433, 2000.

[53] P. A. M. Dirac. Note on exchange phenomena in the Thomas atom. *Proceedings of the Cambridge Philosophical Society*, 26:376–385, 1930.

[54] U. Eichler, M. Brändle, and J. Sauer. Predicting absolute and site specific acidities for zeolite catalysts by a combined quantum mechanics/interatomic potential function approach. *J. Phys. Chem. B*, 101(48):10035–10050, 1997.

[55] G. B. Ellison, P. C. Engelking, and W. C. Lineberger. An experimental determination of the geometry and electron affinity of CH_3. *J. Am. Chem. Soc.*, 100(8):2556–2558, 1978.

[56] D. Fărcaşiu and A. Ghenciu. Determination of acidity functions and acid strengths by ^{13}C NMR. *Prog. Nucl. Mag. Res. Sp.*, 29:129–168, 1996.

[57] W. E. Farneth and R. J. Gorte. Methods for characterizing zeolite acidity. *Chem. Rev.*, 95(3):615–635, 1995.

[58] D. Freude, M. Hunger, H. Pfeifer, and W. Schwieger. ^1H MAS NMR studies on the acidity of zeolites. *Chem. Phys. Lett.*, 128(1):62–66, 1986.

[59] J. D. Gale, C. R. A. Catlow, and J. R. Carruthers. An *ab initio* study of methanol adsorption in zeolites. *Chem. Phys. Lett.*, 216(1-2):155–161, 1993.

[60] P. W. Goguen, T. Xu, D. H. Barich, T. W. Skloss, W. Song, Z. Wang, J. B. Nicholas, and J. F. Haw. Pulse-quench reactor studies reveal a carbon-pool mechanism in methanol-to-gasoline chemistry on zeolite HZSM-5. *J. Am. Chem. Soc.*, 120(11):2650–2651, 1998.

[61] R. J. Gorte. What do we know about the acidity of solid acids? *Catal. Lett.*, 62(1):1–13, 1999.

[62] N. Govind, J. Andzelm, K. Reindel, and G. Fitzgerald. Zeolite-catalyzed hydrocarbon formation from methanol: Density functional simulations. *Int. J. Mol. Sci.*, 3:423–434, 2002.

[63] W. O. Haag and N. Y. Chen. Catalyst design with zeolites. In L. L. Hegedus, editor, *Catalyst Design: Progress and Perspectives*, pages 163–212. John Wiley and Sons, New York, 1987.

[64] F. Haase and J. Sauer. ^{1}H-NMR chemical-shifts of ammonia, methanol, and water molecules interacting with Brønsted acid sites of zeolite catalysis – *ab initio* calculations. *J. Phys. Chem.*, 98(12):3083–3085, 1994.

[65] F. Haase and J. Sauer. Interaction of methanol with Brønsted acid sites of zeolite catalysts – an *ab initio* study. *J. Am. Chem. Soc.*, 117(13):3780–3789, 1995.

[66] F. Haase and J. Sauer. *ab initio* molecular dynamics simulation of methanol interacting with acidic zeolites of different framework structure. *Micropor. Mesopor. Mat.*, 35-36:379–385, 2000.

[67] F. Haase, J. Sauer, and J. Hutter. *ab initio* molecular dynamics simulation of methanol adsorbed in chabazite. *Chem. Phys. Lett.*, 266(3-4):397–402, 1997.

[68] L. P. Hammett and A. J. Deyrup. A series of simple basic indicators. 1. the acidity functions of mixtures of sulfuric and perchloric acids with water. *J. Am. Chem. Soc.*, 54(7):2721–2739, 1932.

[69] J. F. Haw. Zeolite acid strength and reaction mechanisms in catalysis. *Phys. Chem. Chem. Phys.*, 4:5431–5441, 2002.

[70] J. F. Haw, W. Song, D. M. Marcus, and J. B. Nicholas. The mechanism of methanol to hydrocarbon catalysis. *Acc. Chem. Res.*, 36(5):317–326, 2003.

[71] G. Henkelman and H. Jónsson. A dimer method for finding saddle points on high dimensional potential surfaces using only first derivatives. *J. Chem. Phys.*, 111(15):7010–7022, 1999.

[72] P. Hohenberg and W. Kohn. Inhomogeneous electron gas. *Phys. Rev. B*, 136(3B):B864–B871, 1964.

[73] W. G. Hoover. Canonical dynamics - equilibrium phase-space distributions. *Phys. Rev. A*, 31(3):1695–1697, 1985.

[74] G. J. Hutchings, G. W. Watson, and D. J. Willock. Methanol conversion to hydrocarbons over zeolite catalysts: Comments on the rection mechanism for the formation of the first carbon-carbon bond. *Micropor. Mesopor. Mat.*, 29(1-2):67–77, 1999.

[75] J. Hutter, A. Alavi, T. Deutsch, M. Bernasconi, St. Goedecker, D. Marx, M. Tuckerman, and M. Parrinello. CPMD version 3.3. Max-Planck-Institut für Festkörperforschung and IBM Zurich Research Laboratory, 1995-1999.

[76] Y. Jeanvoine, J. G. Àngyán, G. Kresse, and J. Hafner. Brønsted acid sites in HSAPO-34 and chabazite: An *ab initio* structured study. *J. Phys. Chem. B*, 102(29):5573–5580, 1998.

[77] J.-P. Joly and A. Perrard. Determination of the heat of adsorption of ammonia on zeolites from temperature-programmed desorption experiments. *Langmuir*, 17(5):1538–1542, 2001.

[78] H. Jónsson, G. Mills, and K. W. Jacobsen. Nudged elastic band method for finding minimum energy paths of transitions. In B. J. Berne, G. Ciccotti, and D. F. Coker, editors, *Classical and Quantum Dynamics in Condensed Phase Simulations*, pages 385–404. World Scientific, Singapore, 1998.

[79] V. B. Kazansky, A. I. Serykh, V. Semmer-Herledan, and J. Fraissard. Intensities of OH IR stretching bands as a measure of the intrinsic acidity of bridging hydroxyl groups in zeolites. *Phys. Chem. Chem. Phys.*, 5:966–969, 2003.

[80] F. J. Keil. Methanol-to-hydrocarbons: Process technology. *Micropor. Mesopor. Mat.*, 29(1-2):49–66, 1999.

[81] S. Kirkpatrick, Jr. C. D. Gelatt, and M. P. Vecchi. Optimization by simulated annealing. *Science*, 220(4598):671–680, 1983.

[82] J. M. Kobe, T. J. Gluszak, J. A. Dumesic, and T. W. Root. Deuterium NMR characterization of Brønsted acid sites and silanol species in zeolites. *J. Phys. Chem.*, 99(15):5485–5491, 1995.

[83] W. Kohn and L. J. Sham. Self-consistent equations including exchange and correlation effects. *Phys. Rev. A*, 140(4A):A1133–A1138, 1965.

[84] H. Koller, R. F. Lobo, S. L. Burkett, and M. E. Davis. $SiO^- \cdots HOSi$ hydrogen bonds in as-synthesized high-silica zeolites. *J. Phys. Chem.*, 99(33):12588–12596, 1995.

[85] C. Lee, W. Yang, and R. G. Parr. Development of the Colle-Salvetti correlation energy formula into a functional of the electron density. *Phys. Rev. B*, 37:785–789, 1988.

[86] C. S. Lee and M. M. Wu. Reaction of carbenoid species from diazomethane decomposition over zeolite ZSM-5. *J. Chem. Soc. Chem. Comm.*, 5:250–252, 1985.

[87] C. Lo, C. A. Giurumescu, R. Radhakrishnan, and B. L. Trout. Methanol coupling in the zeolite chabazite studied via Car-Parrinello molecular dynamics. *Mol. Phys.*, 102(3):281–288, 2004.

[88] W. Loewenstein. The distribution of aluminium in the tetrahedra of silicates and aluminates. *Am. Mineral.*, 39:92–95, 1954.

[89] G. J. Martyna, M. L. Klein, and M. Tuckerman. Nosé-Hoover chains: The canonical ensemble via continuous dynamics. *J. Chem. Phys.*, 97(4):2635–2643, 1992.

[90] D. Marx and J. Hutter. *ab initio* molecular dynamics: Theory and implementation. In *Modern Methods and Algorithms of Quantum Chemistry*, volume 1 of *NIC Series*, pages 301–449. John von Neumann Institute for Computing, 2000.

[91] E. L. Meijer, R. A. van Santen, and A. P. J. Jansen. Computation of the infrared spectrum of an acidic zeolite proton interacting with acetonitrile. *J. Phys. Chem.*, 100(22):9282–9291, 1996.

[92] U. Messow, K. Quitzsch, and H. Herden. Heats of immersion of ZSM-5 zeolite in n-alkanes, 1-alkenes and 1-alcohols at 30 °C. *Zeolites*, 4(3):255–258, 1984.

[93] J. Meusinger and A. Corma. Influence of zeolite composition and structure on hydrogen transfer reactions from hydrocarbons and from hydrogen. *J. Catal.*, 159:353–360, 1996.

[94] V. V. Mihaleva, R. A. van Santen, and A. P. J. Jansen. A DFT study of methanol adsorption in 8T rings of chabazite. *J. Phys. Chem. B*, 105(29):6874–6879, 2001.

[95] V. V. Mihaleva, R. A. van Santen, and A. P. J. Jansen. The heterogeneity of the hydroxyl groups in chabazite. *J. Chem. Phys.*, 119(24):13053–13060, 2003.

[96] G. Mills and H. Jónsson. Quantum and thermal effects in H_2 dissociative adsorption: Evaluation of free energy barriers in multidimensional quantum systems. *Phys. Rev. Lett.*, 72(7):1124–1127, 1994.

[97] G. Mirth, J. A. Lercher, M. W. Anderson, and J. Klinowski. Adsorption complexes of methanol on zeolite ZSM-5. *J. Chem. Soc., Faraday Trans.*, 86(17):3039–3044, 1990.

[98] B. I. Mosqueda-Jiménez, A. Jentys, K. Seshan, and J. A. Lercher. Structure-activity relations for Ni-containing zeolites during NO reduction. I. Influence of acid sites. *J. Catal.*, 218:348–353, 2003.

[99] M. Nelson, W. Humphrey, A. Gursoy, A. Dalke, L. Kalé, R. D. Skeel, and K. Schulten. NAMD – a parallel, object-oriented molecular dynamics program. *Int. J. Supercomput. Ap.*, 10:251–268, 1006.

[100] M. Neurock. Perspectives on the first principles elucidation and the design of active sites. *J. Catal.*, 216:73–88, 2003.

[101] J. B. Nicholas, J. F. Haw, L. W. Beck, T. R. Krawietz, and D. B. Ferguson. Density functional theoretical and NMR study of Hammett bases in acidic zeolites. *J. Am. Chem. Soc.*, 117(49):12350–12351, 1995.

[102] S. Nosé. A molecular-dynamics method for simulations in the canonical ensemble. *Mol. Phys.*, 52(2):255–268, 1984.

[103] G. A. Olah, H. Doggweiler, J. D. Feldberg, S. Frohlich, M. J. Grdina, R. Karpeles, T. Keumi, S. Inaba, W. M. Ip, K. Lammertsma, G. Salem, and D. C. Tabor. Onium ylide chemistry. 1. bifunctional acid-base-catalyzed conversion of heterosubstituted methanes into ethylene and derived hydrocarbons. the onium ylide mechanism of the $C_1 \rightarrow C_2$ conversion. *J. Am. Chem. Soc.*, 106(7):2143–2149, 1984.

[104] R. G. Parr and W. Yang. *Density Functional Theory of Atoms and Molecules.* Oxford University Press, New York, 1989.

[105] D. J. Parrillo and R. J. Gorte. Characterization of acidity in H-ZSM-5, H-ZSM-12, H-Mordenite, and H-Y using microcalorimetry. *J. Phys. Chem.*, 97(34):8786–8792, 1993.

[106] F. Pascale, P. Ugliengo, B. Civalleri, R. Orlando, P. D'Arco, and R. Dovesi. Hydrogarnet defect in chabazite and sodalite zeolites: A periodic hartree-fock and B3-LYP study. *J. Chem. Phys.*, 117(11):5337–5346, 2002.

[107] D. Passerone and M. Parrinello. Action-derived molecular dynamics in the study of rare events. *Phys. Rev. Lett.*, 87(10):108302–1–108302–4, 2001.

[108] M. C. Payne, M. Hytha, I. Štich, J. D. Gale, and K. Terakura. First principles calculation of the free energy barrier for the reaction of methanol in a zeolite catalyst. *Micropor. Mesopor. Mat.*, 48(1-3):375–381, 2001.

[109] D. A. Pearlman, D. A. Case, J. W. Caldwell, W. S. Ross, T. E. Cheatham III, S. DeBolt, D. Ferguson, G. Seibel, and P. Kollman. AMBER, a computer program for applying molecular mechanics, normal mode analysis, molecular dynamics and free energy calculations to elucidate the structures and energies of molecules. *Comput. Phys. Commun.*, 91(1-3):1–41, 1995.

[110] J. P. Perdew. Unified theory of exchange and correlation beyond the local density approximation. In P. Ziesche and H. Eschrig, editors, *Electronic Structure of Solids '91*, pages 11–20, Berlin, 1991. Akademie Verlag.

[111] J. P. Perdew and A. Zunger. Self-interaction correction to density-functional approximations for many-electron systems. *Phys. Rev. B*, 23(10):5048=5079, 1981.

[112] B. Peters, W. Liang, A. T. Bell, and A. Chakraborty. Biasing a transition state search to locate multiple reaction pathways. *J. Chem. Phys.*, 118(21):9533–9541, 2003.

[113] M. Rasolt and D. J. W. Geldart. Exchange and correlation energy in a nonuniform fermion fluid. *Phys. Rev. B*, 34(2):1325–1328, 1986.

[114] E. Sandre, M. C. Payne, and J. D. Gale. First principles location of the transition state for formation of dimethyl ether in a zeolite. *J. Chem. Soc. Chem. Comm.*, (22):2445–2446, 1998.

[115] A. Sassi, M. A. Wildman, H. J. Ahn, P. Prasad, J. B. Nicholas, and J. F. Haw. Methylbenzene chemistry on zeolite HBeta: Multiple insights into methanol-to-olefin catalysis. *J. Phys. Chem. B*, 106(9):2294–2303, 2002.

[116] A. Sassi, M. A. Wildman, and J. F. Haw. Reactions of butylbenzene isomers on zeolite HBeta: Methanol-to-olefins hydrocarbon pool chemistry and secondary reactions of olefins. *J. Phys. Chem. B*, 106(34):8768–8773, 2002.

[117] G. Sastre and D. W. Lewis. Study of short and long range effects on Brønsted acidity in AFI and CHA zeolites. In M. M. J. Treacy, B. K. Marcus, M. E. Bisher, and J. B. Higgins, editors, *Proceedings of the 12th International Zeolite Conference*, volume 1, pages 341–348, Warrendale, PA, 1999. Materials Research Society.

[118] J. Sauer, M. Sierka, and F. Haase. Acidic catalysis by zeolites: *ab initio* modeling of transition structures. In D. G. Truhlar and K. Morokuma, editors,

Transition State Modeling for Catalysis, volume 721 of *ACS Symposium Series*, pages 358–367, Washington D.C., 1999. American Chemical Society, American Chemical Society.

[119] R. Shah, J. D. Gale, and M. C. Payne. *In Situ* study of reactive intermediates of methanol in zeolites from first principles calculations. *J. Phys. Chem. B*, 101(24):4787–4797, 1997.

[120] R. Shah, M. C. Payne, and J. D. Gale. Methanol adsorption in zeolites – a first principles study. *J. Phys. Chem.*, 100(28):11688–11697, 1996.

[121] R. Shah, M. C. Payne, and J. D. Gale. Acid-base catalysis in zeolites from first principles. *Int. J. Quant. Chem.*, 61(3):393–398, 1997.

[122] R. Shah, M. C. Payne, M.-H. Lee, and J. D. Gale. Understanding the catalytic behavior of zeolites: A first-principles study of the adsorption of methanol. *Science*, 271(5254):1395–1397, 1996.

[123] S. B. Sharma, B. Meyeres, D. Chen, J. Miller, and J. A. Dumesic. Characterization of catalyst activity by microcalorimetry and temperature-programmed desorption. *Appl. Catal. A: Gen.*, 102(2):253–265, 1993.

[124] M. Sierka, U. Eichler, J. Datka, and J. Sauer. Heterogeneity of Brønsted acidic sites in faujasite type zeolites due to aluminum content and framework structure. *J. Phys. Chem. B*, 102(33):6397–6404, 1998.

[125] M. Sierka and J. Sauer. Proton mobility in chabazite, faujasite, and ZSM-5 zeolite catalysts. comparison based on *ab initio* calculations. *J. Phys. Chem. B*, 105(8):1603–1613, 2001.

[126] P. E. Sinclair and C. R. A. Catlow. Computational studies of the reaction of methanol at aluminosilicate Brønsted acid sites. *J. Chem. Soc., Faraday Trans.*, 92(12):2099–2105, 1996.

[127] P. E. Sinclair and C. R. A. Catlow. Density functional theory calculations of adsorption and reactivity of methanol at alumino-silicate Brønsted acid centres. *J. Chem. Soc., Faraday Trans.*, 93(2):333–345, 1997.

[128] L. J. Smith, A. Davidson, and A. K. Cheetham. A neutron diffraction and infrared spectroscopy study of the acid form of the aluminosilicate zeolite, chabazite (H-SSZ-13). *Catal. Lett.*, 49(3-4):143–146, 1997.

[129] R. D. Smith and J. H. Futtrell. Evidence for complex formation in the reactions of CH_3^+ and CD_3^+ with CH_3OH, CD_3OD, and C_2H_5OH. *Chem. Phys. Lett.*, 41(1):64, 1976.

[130] A. A. Sokol, C. R. A. Catlow, J. M. Garcés, and A. Kuperman. Local states in microporous silica and aluminum silicate materials. 1. modeling structure, formation, and transformation of common hydrogen containing defects. *J. Phys. Chem. B*, 106(24):6163–6177, 2002.

[131] W. Song, J. F. Haw, J. B. Nicholas, and C. S. Heneghan. Methylbenzenes are the organic reaction centers for methanol-to-olefin catalyis on HSAPO-34. *J. Am. Chem. Soc.*, 122(43):10726–10727, 2000.

[132] W. Song, D. M. Marcus, H. Fu, J. O. Ehresmann, and J. F. Haw. An oft-studied reaction that may never have been: Direct catalytic conversion of methanol or dimethyl ether to hydrocarbons on the solid acids HZSM-5 or HSAPO-34. *J. Am. Chem. Soc.*, 124(15):3844–3845, 2002.

[133] W. Song, J. B. Nicholas, and J. F. Haw. A persistent carbenium ion on the methanol-to-olefin catalyst HSAPO-34: Acetone shows the way. *J. Phys. Chem. B*, 105(19):4317–4323, 2001.

[134] W. Song, J. B. Nicholas, A. Sassi, and J. F. Haw. Synthesis of the heptamethylbenzenium cation in zeolite-β: *in Situ* NMR and theory. *Catal. Lett.*, 81(1-2):49–53, 2002.

[135] H. Soscún, O. Castellano, J. Hernández, and A. Hinchliffe. Acidity of the Brønsted acid sites in zeolites. *Int. J. Quant. Chem.*, 82(3):143–150, 2001.

[136] M. Sprik and G. Ciccotti. Free energy from constrained molecular dynamics. *J. Chem. Phys.*, 109(18):7737–7744, 1998.

[137] I. Štich, J. D. Gale, K. Terakura, and M. C. Payne. Dynamical observation of the catalytic activation of methanol in zeolites. *Chem. Phys. Lett.*, 283(5-6):402–408, 1998.

[138] M. Stöcker. Methanol-to-hydrocarbons: Catalytic materials and their behavior. *Micropor. Mesopor. Mat.*, 29(1-2):3–48, 1999.

[139] N. Tajima, T. Tsuneda, F. Toyama, and K. Hirao. A new mechanism for the first carbon-carbon bond formation in the MTG process: A theoretical study. *J. Am. Chem. Soc.*, 120(32):8222–8229, 1998.

[140] P. Treesukol, J. P. Lewis, J. Limtrakul, and T. N. Truong. A full quantum embedded cluster study of proton siting in chabazite. *Chem. Phys. Lett.*, 350(1-2):128–134, 2001.

[141] N. Troullier and J. L. Martins. Efficient pseudopotentials for plane-wave calculations. *Phys. Rev. B*, 43(11):1993–2006, 1991.

[142] B. L. Trout and M. Parrinello. Analysis of the disociation of H_2O in water using first-principles molecular dynamics. *J. Phys. Chem. B*, 103(34):7340–7345, 1999.

[143] S. Tsuzuki and H. P. Lüthi. Interaction energies of van der Waals and hydrogen bonded systems calculated using density functional theory: Assessing the PW91 model. *J. Chem. Phys.*, 114(9):3949–3957, 2001.

[144] J. P. van den Berg, J. P. Wolthuizen, and J. H. C. van Hooff. In L. V. C. Rees, editor, *Proceedings of the 5th International Conference on Zeolites*, pages 649–, London, 1980. Heyden.

[145] R. A. van Santen. Quantum-chemistry of zeolite acidity. *Catal. Today*, 38(3):377–390, 1997.

[146] G. Vitale, L. M. Bull, B. M. Powell, and A. K. Cheetham. A neutron-diffraction study of the acid form of zeolite-Y and its complex with benzene. *J. Chem. Soc. Chem. Comm.*, (22):2253–2254, 1995.

[147] J. M. Vollmer, E. V. Stefanovich, and T. N. Truong. Molecular modeling of interactions in zeolites: An *ab initio* embedded cluster study of NH_3 adsorption in chabazite. *J. Phys. Chem. B*, 103(44):9415–9422, 1999.

[148] S. H. Vosko, L. Wilk, and M. Nusair. Accurate spin-dependent electron liquid correlation energies for local spin-density calculations – a critical analysis. *Can. J. Phys.*, 58(8):1200–1211, 1980.

[149] T. Xu, D. H. Barich, P. W. Goguen, W. Song, Z. Wang, J. B. Nicholas, and J. F. Haw. Synthesis of a benzenium ion in a zeolite with use of a catalytic flow reactor. *J. Am. Chem. Soc.*, 120(16):4025–4026, 1998.

[150] L.-T. Yuen, S. I. Zones, T. V. Harris, E. J. Gallegos, and A. Auroux. Product selectivity in methanol to hydrocarbon conversion for isostructural compositions of AFI and CHA molecular sieves. *Micropor. Mat.*, 2:105–117, 1994.